Novel Microfabrication Techniques Towards Next-Generation In Vitro and In Vivo Medical Devices

Thesis by

Sau Yin Chin

Submitted in partial fulfillment of the

Requirements for the degree of

Doctor of Philosophy

in the Graduate School of Arts and Sciences

Columbia University

2015

Abstract

Novel Microfabrication Techniques Towards Next-Generation In Vitro and In Vivo Medical Devices

Sau Yin Chin

Microfabrication has given rise to numerous technologies and has resulted in new paradigms for how science and technology has advanced in recent years. Having originated from the microelectronics industry, microfabrication techniques have increasingly been leveraged in the development of various other fields. Such techniques have an increasing presence in the field of medical devices, especially with the advent of microfluidics. The capability that microfluidics lends to miniaturizing and making portable analytical tools was, and still is, extremely useful in the advancement of medical technologies.

In this dissertation, we explore novel microfabrication techniques towards the development of next-generation medical devices. We can broadly classify these devices as devices that function in *in vitro* and *in vivo* settings. *In vitro* devices typically function in a non-invasive manner such as when patient samples are processed externally for diagnostic purposes. *In vivo* medical devices, on the other hand, normally play a role in disease treatment upon implantation into a patient, such as with stents, pacemakers and drug delivery devices. Here we demonstrate how microfabrication techniques can be implemented in the improvement of devices involved in diagnosis and treatment; two important branches of medical sciences that go hand in hand. Firstly, microfabrication and microfluidic techniques were implemented in developing a CD4+ T helper cell counter. This integrated device, where capture and analysis are performed on the same platform, also employs a chemiluminescence-based method of detection. This a rather simple and elegant technique that is amenable for miniaturization in future as it does not require the use of external complex light source (such as for fluorescence imaging) nor the use of image/data analysis methods.

The second part of this dissertation describes novel microfabrication techniques for the development of a new class of implantable devices- hydrogel MEMS devices. This technique is comparable to additive manufacturing techniques such as 3D printing. Current 3D printing or fabrication techniques for biocompatible materials normally result in standalone structures. Using our technique, we are not only able to construct microcomponents entirely out of hydrogels but also have the capability to assemble and align various moving components to form a robust MEMS-like device. As these MEMS devices are constructed entirely out of biocompatible PEG-based hydrogels, they are ideal candidates for implantable devices. Once implanted, they can be wirelessly actuated using simple permanent magnets and the operation of the devices do not require onboard power-sources or electronics, which is common for current MEMS-based implantable devices. These devices can also be designed to deliver payloads and this delivery can be actively controlled. We also explore the use of hydrogel MEMS in the in vivo delivery of therapeutics, and assess its efficacy in delivering local, low-doses of a chemotherapeutic drug in a disease model. We envision that these devices, and the technology from which they are borne, will open up a new paradigm in the way implantable devices are developed.

Table of Contents

List of figures

List of tables

Acknowledgements

Someone once told me that completing a PhD is akin to going through childbirth; it's really difficult at times but somehow you will get through it and you will have your bundle of joy (in this case, a degree). Indeed, this thesis has been a long time coming and it was not an easy road. There were numerous complications for it to come to its full-term. In extremely rough times I would remember this analogy and tell myself that the pain was temporary. Numerous sacrifices were made for this offspring but all in all it has been an enlightening journey. Hopefully, I can be proud of the fruits of my labor as how all parents are proud of their children.

This journey was not traversed alone and I have many people whom which I will be eternally grateful to. Firstly, I would not be able to pursue my higher education without the generous support of my sponsors, the Agency for Science, Technology and Research (A*STAR), Singapore. I would like to thank them for having faith in me and giving me the resources to pursue both my undergraduate and graduate studies.

I would also like to thank my advisor, Professor Samuel Sia, for giving me the opportunity to work in his lab as well as all his advice, support and encouragement over the years. I would also like to express my appreciation for the occasional ideas that are a bit "out there" for without crazy ideas there won't be interesting projects and this thesis for one would not exist. I am eternally grateful to the members of Sia Lab, both past the present members. The first generation of graduate students really helped me with useful advice (and funny anecdotes) and made me feel like part of the lab. Specifically, I would like to thank Curtis Chin for his kind advice and passing on the baton for the CD4 project, Yukkee Cheung-Poh for always being very willing to help and her awesome advice even via Skype as a consultant on the hydrogel MEMS project, Brian Gillette for experimental tips, advice in animal work and enthusiasm in everything science, and Hesam Parsa for moral support, sage advice and occasional delicious Persian fare. I would also like to thank Tassaneewan Laksanasopin who both started and finished this journey together with me, we have been through a lot together through the ups-and-downs of this PhD program and her moral support, advice and ear (that I have severely bent at times) were invaluable. Also, the other junior PhD students who have had to deal with this grumpy old PhD student; Tiffany Guo for being ever so cheerful (until I broke her) and extremely willing to answer any random medical-related question I might have, Nalin Tejavibulya with whom I've enjoyed brainstorming ideas on gears, devices and commiserations on mystery smells, and Samiksha Nayak for all her help, being the social chair of the lab and always believing me when

I say Myra will visit. Ninna Rossen, for always being ever so cheerful and helping with last minute experiments. Also, not forgetting my students, notably Kathryn Lau, Lauren Hsu and Sarah Kim who have provided much needed help required to push these projects forward.

Other members of the BME department that I would like to thank are Keith Yeager for his vast knowledge, expertise and invaluable help in using (and sometimes building) various equipment, and members of the Kam Lab who so generously allow me to use their equipment and reagents whenever I need to (and Helen for the quote).

Then there are the very important people who have not been physically with me throughout this journey but have the most faith in me. My parents, who have made me the person I am today and supported all my decisions (and even when they don't agree they pretend to). Ma and Pa, I am very grateful for all you have done even if I don't always show it. I hope this offspring of yours has done you proud. My brothers, who I know will always be there and hope the best for me. Also, thanks for having kids and taking the pressure off of me while I finish up my PhD! Lastly, all my friends whom I've met along this journey in various countries and are just too many to list here. Thanks for being supportive even though I don't do a good job of explaining what it is exactly I'm working on and you have no idea what I'm talking about. Thanks for nodding and saying that it sounds cool!

My eternal gratitude,

Sau Yin Chin

New York, New York

May 2015

Chapter 1

Overview

1.1 Introduction

MEMS technologies have been around for the past few decades and since the development of the first generation lab-on-a-chip platform[1], which is also the first demonstration of microfluidics, there has been an exponentially growing interest in applying such technologies in the medical field. Various efforts have been put towards using MEMS and microfluidic technologies to improve the efficiency of diagnostic tools[2-4], developing new medical devices for disease treatment and management[5, 6] as well as increasing the accessibility and affordability of such devices for underserved populations[7-9].

Here we focus on developing technologies for a new generation of medical devices. We can broadly classify these devices as devices that function in *in vitro* and *in vivo* environments. *In vitro* devices typically function in a non-invasive manner where patient samples are processed externally, such as in diagnostic tests. *In vivo* medical devices, on the other hand, normally function as treatment devices upon implantation, such as stents, pacemakers and drug delivery devices. As both diagnosis and treatment are essential in patient care and go hand-in-hand, we aim to demonstrate how novel microfabrication techniques can be used to address clinical needs in these two important branches of medical care.

In terms of developing new diagnostics tools, implementation of microfluidic technologies often result in varying levels of success. For example, various microfluidic assays lack the integration of “capture” and “analysis” on a single chip; target analytes that are isolated and/or processed from a sample have to be enumerated or quantified on a separate platform. Even when the analyses of the captured target analytes are achieved on the same platform, they often require the use of standard lab equipment such as fluorescence microscopes or computers for

quantification purposes[10-13]. This culminates in a host of microfluidic technologies that only perform part of an assay, may still require the use of other standard analytical tools with core technologies that are unnamable for miniaturization and thus are impractical to be used in point-of-care settings where these assays are often most needed. In this thesis, the first specific aim is to develop a fully integrated diagnostic device that performs both the capture and detection of T-lymphocytes. A microfluidic device was developed to specifically capture CD4+ T-lymphocytes from whole blood samples and using chemiluminescence-based detection, we were able to detect and enumerate the cells captured on the same platform. This technique also only requires the use of simple equipment and as it does not involve the use of external complex light sources (such as for fluorescence microscopy), the method of detection is amenable for miniaturization for future use at the point-of-care.

In terms of developing implantable medical devices, MEMS technology has made significant breakthroughs in developing such devices for the treatment of disease and management of health. These devices range from stents[14] and pacemakers to drug delivery devices[15] and, to a certain extent, wearable electronics[16]. However, most of these devices are still based on silicon-technologies and often have a host of biocompatibility issues. This makes them non-ideal for use as implantable devices unless they are coated with biocompatible or non-biofouling materials[17, 18], which could still potentially fail or wear off with extended use in the body. In this thesis, a new generation of fully biocompatible MEMS devices constructed entirely out of hydrogels is proposed. In Chapters 2 to 5, we explore the material characteristics of the hydrogels used for constructing implantable MEMS devices, the various design considerations that are unique to the case of using hydrogels as building blocks towards the goal of a sophisticated, implantable device that can be actively controlled post-implantation, as well as the implementation of these devices in an in vivo environment. Finally, we also demonstrate the use of such devices in the treatment of a disease model.

1.2 Organization

This dissertation will be organized in the following manner:

Chapter 2: A microfluidic CD4 T-cell counting device using chemiluminescence-based detection. The development of a microfluidic device for the enumeration of CD4+ T-lymphocytes from whole blood samples is described. Using a combination of microfabrication and microfluidic techniques, capture and detection of CD4+ T-lymphocytes, a clinical target for monitor HIV/AIDS, is integrated on a single chip. This device was also built on technology that is amenable for miniaturization and hence can be used in resource-poor settings. This work has since been published- Wang, Zuankai†, **Sau Yin Chin**†, Curtis D. Chin, John Sarik, Maritza Harper, Jessica Justman, and Samuel K. Sia. "Microfluidic CD4+ T-cell counting device using chemiluminescence-based detection." *Analytical chemistry* 82, no. 1 (2009): 36-40. († Authors contributed equally to this work)

Chapter 3: Characterization and tuning of mechanical and diffusive properties of PEGDA hydrogels towards a viable building block for MEMS devices. We explore various compositions of PEGDA-based hydrogels to determine suitable candidates to be uised as building blocks for a MEMS device. To this end, we extensively characterized the mechanical and diffusive properties of an array of PEGDA-based hydrogels.

Chapter 4: The design, fabrication and testing MEMS devices that are actuated magnetically and constructed entirely out of PEGDA hydrogel. Using a novel fabrication technique, we designed, constructed and tested the robustness of hydrogel-based MEMS devices. We also devised methods for creating PEGDA-based components that respond to magnetic actuation. Additionally, we take advantage of the “soft” properties of hydrogels which are traditionally considered a disadvantage from a microfabrication standpoint. By leveraging

the wide range of properties of PEGDA hydrogels, we can potentially increase the functionality of the fabricated components.

Chapter 5: The development and testing PEGDA-based MEMS devices in *in vitro* and *in vivo* environments towards implantable drug delivery devices. We examine the capability of these fabricated PEGDA-based MEMS devices in delivering payloads. The delivery of drugs and other payloads by these devices is controlled wirelessly and externally using magnets. We also show the capability of selectively delivering one of multiple types of payloads.

Chapter 6: An implantable PEGDA-based MEMS device for local, low-dose chemotherapy treatment of osteosarcoma. In the culmination of the extensive work done on developing an implantable hydrogel-based MEMS device, we further demonstrate the use of this device as a means for delivering chemotherapy drugs locally at the site of a tumor in a mouse osteosarcoma model. This method of delivery is potentially more efficacious than traditional IV-administered chemotherapy as well as minimizes the severely detrimental side effects of chemotherapy.

Chapter 2

Microfluidic CD4 T-cell counter for HIV/AIDS monitoring in resource poor settings.

2.1 Introduction

HIV/AIDS remains a major pandemic in both developed[19] and developing countries[20]. Patients diagnosed as HIV positive are required to have their CD4+ T-cell count (CD4 count) enumerated from whole blood samples as these cells are the primary targets for the virus. A patient's CD4 count, together with viral load information, is an indication of the progression of the disease. This is crucial information especially during the initial decisions regarding ART administration and clinical management[21]. However, there remains an unmet need for a point-of-care (POC) CD4 cell counter[7, 22-24]. This is especially crucial in areas where the disease is most widespread; resource-poor settings in developing countries.

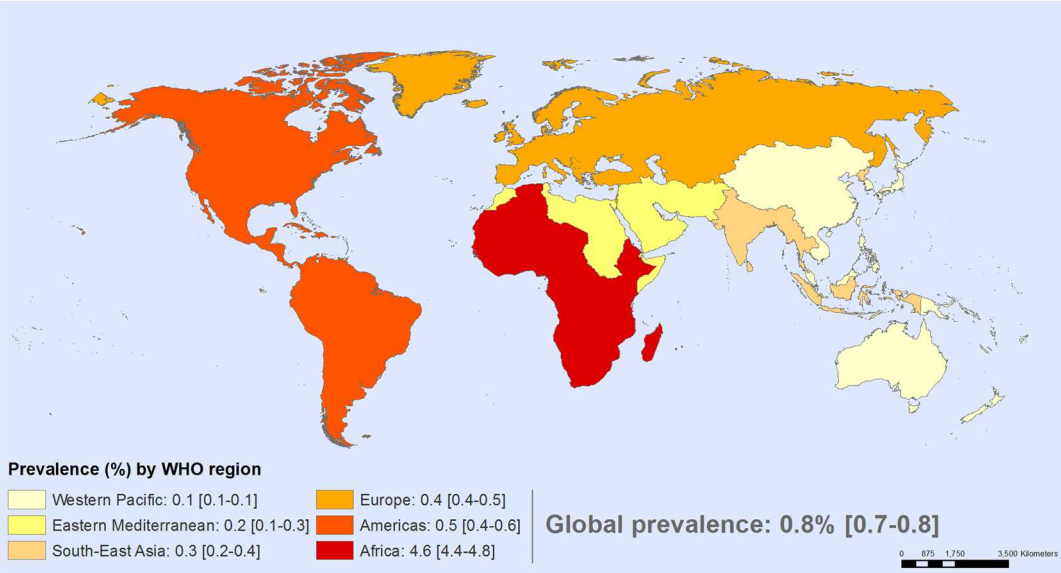

Prevalence of HIV/AIDS by WHO region.

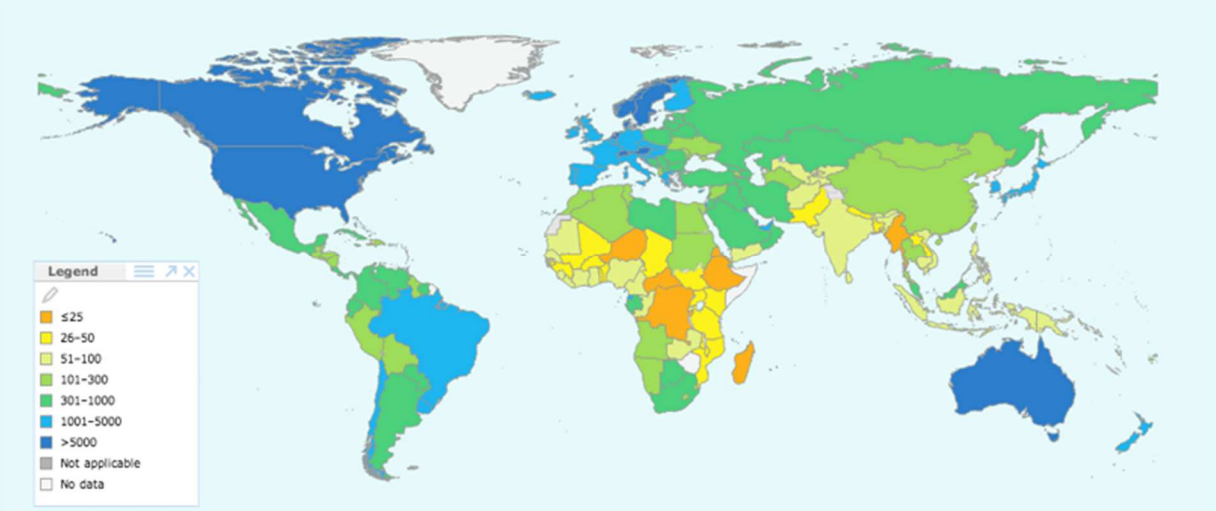

Per capita total expenditure on health care at average exchange rate ($US)

Figure 2.1: Maps showing the prevalence of HIV/AIDS as well as the per capita expenditure on health care for different countries. It can be seen that countries with a high prevalence of HIV/AIDS also have less resources to spare on health care, such as Sub-Saharan Africa[25, 26]. *(Source: World Health Organization)*

According to CDC disease-staging[27], HIV positive patients with CD4 counts that are less than 200cells/μL are considered as having AIDS. At this point, antiretroviral treatments should be initiated[28] though more recent research has shown that such treatment would be more effective at higher CD4 counts; WHO 2013 Consolidated ART guidelines recommend an ART initiation threshold of CD4 counts of 500cells/μL[29]. The CD4 count is also an important factor in making clinical decisions regarding screening and prophylaxis treatment for major HIV-related opportunistic infections[21, 30]. For patients who are already undergoing antiretroviral treatments, it is still important to monitor their CD4 counts in order to direct any necessary changes to the treatment regimen especially in the absence of viral load testing. Regular monitoring of CD4 counts also play a role in disease management as antiretroviral treatments become more available to AIDS patients and as cases of drug resistance become more prevalent[31, 32].

The current gold standard for obtaining CD4 counts is via flow cytometry. Flow cytometry is a highly precise and high throughput method for obtaining cell counts but it is not practical for use in resource-poor settings. Flow cytometers require central laboratory facilities as well as trained personnel for its operation. Also, a rather large volume of blood (in the order of mLs) is required for flow cytometry, and this requires a venous draw to be performed. Thus, the availability of a low-cost, potentially portable CD4 counter that uses just a pinprick volume of blood (<50μL) would result in a tremendous improvement for the timely diagnosis and monitoring of AIDS patients.

Indeed, there have been various efforts to develop a point-of-care CD4 counter. Microfluidic approaches include a PDMS-glass microfluidic chip consisting of an open chamber that is functionalized with anti-CD4 antibodies[11]. Upon capture of CD4+ cells, the CD4 count is enumerated by manual counting under a microscope (Figure 2.2A). This technique is also a label-free method and only utilizes the specific capture of all cells expressing CD4. Therefore, it is subject to errors such as an artificially high CD4 count due to monocyte contamination (monocytes also express CD4). This technology was later improved using a double-stage cascade device containing monocyte-depletion zones that utilizes anti-CD14 antibodies to first deplete the sample of monocytes before CD4+ capture[10]. Although the authors showed that they were able to improve their results, the final CD4 count was still obtained manually under microscopy.

There have also been efforts to capture cells on a porous-membrane system; the membrane is etched to have 3μm pores that allows the passage of red blood cells but retains larger cells such as lymphocytes (Figure 2.2B and Figure 2.2C). In this manner, the sample can be purified prior to enumeration. Prior to cell capture, the blood samples are immunolabelled with anti-CD3 and anti-CD4 antibodies conjugated with fluorescent tags[13] or quantum dots[12] of different emission wavelengths. Thus, by using digital image analysis methods, the cells of interest can

be specifically identified and counted. For these strategies, miniaturization of the peripheral instrumentation and detection system to produce signals that can be collected rapidly and automatically reported (and without the need for complex or bulky optical or electrical systems) continues to present a challenge for their use in truly remote settings.

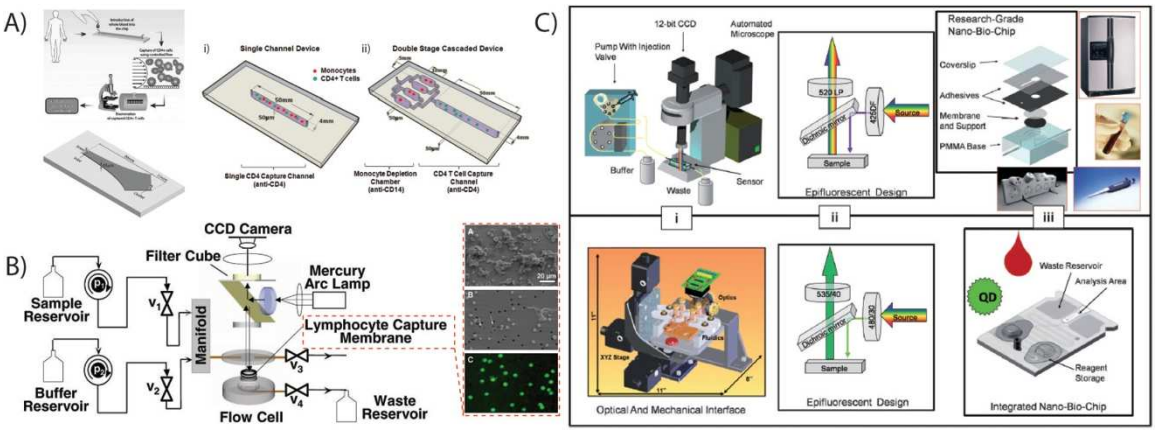

Figure 2.2: Current efforts in developing a point-of-care CD4 counter. (A) A PDMS-glass based microfluidic chip with an open chamber for the capture of CD4 cells. CD4 cells are enumerated manually via cell-counting under a microscope. An improved second generation device with monocyte depletion chambers was also developed to improve the accuracy of CD4 counts obtained. (B), (C) Schematic of systems utilizing porous membranes for capture and imaging of CD3+CD4+ cells. These systems require the use of fluorescence imaging , thus involving complex light sources and cameras.

More recently, Zyomyx, Inc has developed a point-of-care CD4 test based on cell capture and stacking method that does not require any external equipment or reporter agent. This device has recently been awarded the CE mark and is undergoing clinical trials[33]. They have shown a high correlation between their cell stacking height and CD4 counts obtained via flow cytometery (Figure 2.3). However, on closer inspection of their data it is noticed that there is a large scatter in the data points at lower, more clinically relevant CD4 counts, making this technology not as attractive for monitoring patients who are known to have low CD4 counts. Perhaps the most prevalent point-of-care CD4 counter on the market now is the Alere Pima

CD4 test. It is a cartridge-based fingerstick test that uses either pinprick or venous blood samples and returns a CD4 count in 20 minutes based on static image analysis (Figure 2.3B). However, this system is still a rather bulky set-up weighing 2.5kgs and is powered by an AC source or a rechargeable battery that takes up to 10 hours to be fully charged.

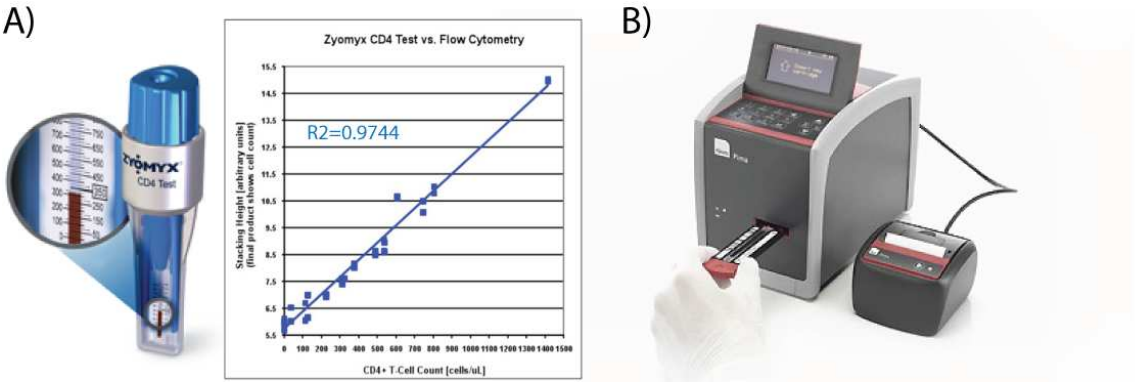

Figure 2.3: Current commercial point-of-care CD4 counters. (A) The Zymoyx CD4 counter is based on a cell capture and stacking method that does not require an external analyzer. (B) The Alere Pima CD4 test is consists of a cartridge that uses fingerstick samples, an analyzer and a printer. It analyzes CD4 counts based on static image analysis.

Our proposed strategy is a microfluidic chip that is surface functionalized to present anti-CD4 antibodies on its surface so as to specifically capture CD4+ cells from a blood sample that is run through the chip. Following the capture and separation of these cells from the rest of the blood sample, the cells will then be detected using chemiluminescence; the blood sample is first pre-incubated with anti-CD3 antibodies and a secondary antibody that is conjugated with horseradish peroxidase. Thus, when a chemiluminescent substrate is introduced to the microfluidic chip after the CD4 T-cells (that are both CD4+ and CD3+) are captured, a chemiluminescent signal will be generated. This signal will be detected by a photodetector and converted to a quantifiable current signal.

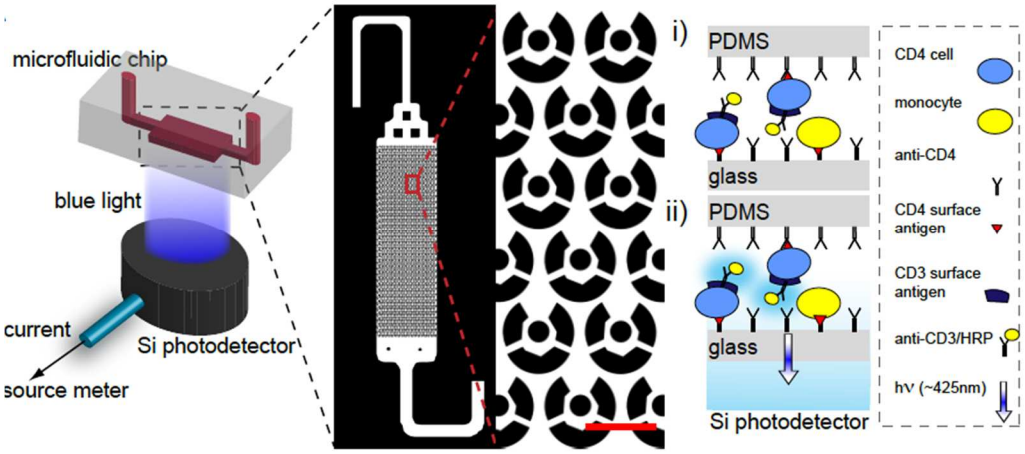

Figure 2.4: Schematic diagram of our microfluidic chip, capture and detection strategies. The left panel shows a schematic of diagram of the entire set-up while the middle panel shows the design of microfluidic traps (scale bar is 100 μm) The right panel shows a schematic diagram of the cell-capture strategy. For cell capture, whole blood is introduced into the chip, followed by rinsing of unbound cells (including red blood cells) (top). As both monocytes and T lymphocytes are CD4+, these two cell types remain within the chip, however only the T lymphocytes have CD3 surface antigens and are hence labeled with CD3-IgG-HRP. Therefore, when luminol and hydrogen peroxide is introduced, the generation of light would only result from the presence of CD4 cells (bottom). This blue light is detected by a silicon photodetector and is then converted to a photocurrent.

Design of microfluidic chip and capture of CD4 cells

Since we are only using a small volume of sample (10-20μL of whole blood) to, we have to maximize the capture of the very small fraction of CD4 T-cells. Building on previous passive methods for cell capture [11], we designed a microfluidic chip with microfabricated pillars unto which the capture antibodies can be immobilized. This not only increases the area of the chip that can be coated with antibodies, but it also increases the surface area on which the cells can interact with the chip. We also designed the pillars to produce a range of shear stresses in order to ensure that the target cells experience the optimal values of shear stress for binding to surfaces [10] on some regions of the chambers, yet allowing the free passage of the bulk of the red blood cells in the sample and cells other than that of our interest.

2.2 Methods

The three main components in achieving the aims in the chapters are 1) the designing of a microfluidic chip that has large surface areas for cell capture as well as a range of shear stresses to aid in the capture of cells, 2) the surface functionalization of the microfluidic chip with CD4+ antibodies and 3) the use of chemiluminescence for the detection of cells as well as the analysis of the light signal towards quantitative measurements.

2.2.1 Materials

Polydimethylsiloxane (PDMS) is purchased from Dow Corning (Midland, MI). High intensity UV lamp (Model B-100A) was purchased from UVP, Inc. (Upland, CA). SU-8was purchased from Microchem Corporation (Newton, MA) while 3-mercaptopropyl trimethoxysilane, luminol and hydrogen peroxide were purchasd from Sigma (St. Louis, MO). GMBS (N-y-maleimidobutyrryloxysuccinimide), NeutrAvidin and bovine serum albumin (BSA) were purchased from Fisher Scientific (Pittsburgh, PA). Biotinylated anti-CD4 antibodies were purchased from Beckman Coulter (Jersey City, NJ). Mouse anti-human CD3 antibodies, goat anti-mouse IgG conjugated with AlexaFluor488 (IgG-AF488) and goat anti-mouse IgG conjugated with horseradish peroxidase (IgG-HRP) were purchased from Invitrogen (now known as Life Technologies, Carlsbad, CA). Red blood cell lysis buffer was purchased from eBioscience (San Diego, CA). . A silicon photodiode (UV-818, Newport, Stratford, CT) and a Model 2602A Dual-channel System SourceMeter (Keithley, Cleveland, OH) were also used.

2.2.2 Mask design. The transparency mask for the microfluidic design was designed in AutoCAD and printed by CAD/Art services, Inc (Bandon, OR). The microfluidic chip was designed to measure 30 mm $\times$ 5 mm, as shown in Figure 3 and contains hundreds of micro-trap arrays inside the flow chamber (measuring 10 mm $\times$ 3.2 mm) to significantly increase the surface area for antibody immobilization. The “trap” was designed with a pillar surrounded by C-

cups with a gap of about 17.5 μm. A smaller gap and dense trap arrays arrangement increases the cell-capture ability of our chip. The distance between each trap was 25 μm, with a shift of 88 μm every three rows to facilitate cell contact with trap surface.

2.2.3 Chip fabrication. The chip was fabricated using standard soft lithographic techniques[34]. Briefly, and SU-8 master was first fabricated using traditional lithography methods; a layer of 45 μm thick SU-8 3050 was spun onto a 3-inch silicon wafer, baked, and exposed under UV light to define a negative feature of the microfluidic chip in the resist based on the mask designed as described in 2.2.2. The chip was then molded in polydimethylsiloxane (PDMS) from the SU-8 master. PDMS pre-polymer was cast on the SU-8 master and baked for 2 hour at oven of 70^{o}C. We peeled off the PDMS mold, and punched holes for fluidic connections. Next, the PDMS chip was bonded to glass after plasma treatment for 1 minute.

2.2.4 Surface modification of microfluidic chip. The fabricated devices were modified for maximum CD4 antibody immobilization using a similar method reported before[10, 11]. Briefly, after the hydroxyl groups on PDMS surface were generated following plasma treatment, the fabricated devices were immediately permanently bonded to glass and treated with a 4% (v/v) solution of 3-mercaptopropyl trimethoxysilane in ethanol for 30 min at room temperature so that both the PDMS and glass will be functionalized. After surface silanization, the chip was incubated with 0.01 mM GMBS (N-y-maleimidobutyryloxysuccinimide) in ethanol for 15 minutes at room temperature. NeutrAvidin was then immobilized to GMBS by incubating the chip surfaces with 10μg mL^{-1} NeutrAvidin solution in PBS overnight at 4^{o}C. Afterwards, a 10 μg/ mL biotinylated anti-CD4 solution in PBS and 1% (w/v) BSA was introduced to chip and incubated at room temperature for 15 minutes. Rinsing steps were conducted after each step to remove unreacted molecules.

2.2.5 Cell capture and Chemiluminescence-based detection

To assess the effectiveness of capturing CD4+ T-cells, we passed a small volume (3 μL) of human whole blood through the chip and used fluorescence microscopy to count the number of cells captured in the chamber. Throughout this study, we used anti-CD3 antibody for detection in order to avoid signal from captured monocytes (which express CD4 but not CD3 on the cell surface). For initial studies, cell capture was first confirmed and quantified using a fluorescent-labeled antibody while chemiluminescent detection was achieved later on by utilizing antibodies conjugated with horseradish peroxidase.

2.2.6 Blood immunolabelling. Blood samples donated from healthy patients were obtained from the Columbia University Medical School, under an approved IRB protocol. Varying CD3+/CD4+ cell counts within the range of values typically encountered in both healthy and immunocompromised individuals were simulated by diluting blood in a PBS solution with 1%(w/v) BSA using a method similar to that reported by work in the similar field (previous studies where samples were diluted from normal patients[12, 35]. For staining, we first incubated the whole blood with mouse, anti-human CD3 antibodies in PBS containing 1% BSA followed by goat, anti-mouse IgG conjugated with an Alexa Fluor 488 (IgG-AF488). For CL based detection, goat anti-mouse IgG conjugated with horseradish peroxidase (IgG-HRP) was used instead of IgG-AF488. The concentrations of the primary and secondary antibodies and the reaction/incubation times were optimized. While CD4 antigens are expressed by monocytes as well, fluorophore or HRP will not be linked to monocytes, since monocytes are not a subset of T cells (CD3+). As a result, monocytes are excluded in this counting process, though some monocytes might be captured in the microfluidic chip (as shown in Figure 2.5).

2.2.7 Cell capture and detection. To identify the optimal flow condition and characterize our device performance, we first conducted fluorescence-based detection. After rinsing away unbound molecules in the microfluidic chip, we introduced the stained blood into the chip and the blood was left to incubate in the chip for 15 minutes. A red blood cell lysis buffer was then flowed through the chamber at 2 μL/min for 10 minutes to lyse red blood cells that might clog up the microfluidic chamber. Subsequently, PBS containing 1% BSA (w/v) was flowed through the chip at 2μL/min for 15 minutes to rinse off unbound cells and quench the lysis buffer. In order to accurately count the CD4 cells (particle auto-fluorescence can lead to artificially high CD4 counts), we counted the cells under high-resolution microscopy and compared phase-contrast images to the fluorescence images to confirm that the fluorescent bodies counted were indeed cells. Control experiments, without any CD4 antibody immobilized on the surface on the chamber, were conducted to assess the non-specific binding. The net count in the chamber was determined by subtracting non-specific binding from the whole count. The capture efficiency of the device was estimated from the ratio of captured CD3+CD4+ cells in chamber (divided by the volume in the capture zone in which the cells were trapped and counted) to the count obtained via flow cytometry. Flow cytometry data was collected on a Cytomics FC 500 (Beckman Coulter, Fullerton, CA) using a protocol provided by the manufacturer.

For chemiluminescence-based detection, we placed a silicon photodetector (UV-818, Newport) directly under the capture chamber of the PDMS microchip (following incubation of blood, lysing and rinsing steps) to minimize the optical path length and maximize signal collection. Prior to chemiluminescent measurements, the dark current was measured by measuring photocurrent signals before any solution was introduced into the chip. A mixture of hydrogen peroxide and luminol (Sigma, St. Louis) was then injected into the microfluidic chip at a flow rate of 5 μL/min. In the presence of horseradish peroxidase, which is on the surface of the captured CD4 cells, the oxidation of luminol is catalyzed and the excess energy associated

with this reaction is liberated as photons, visible as a blue light. We collected the emitted blue light using a silicon photodiode (UV-818, Newport) with a 1000ms gate time, and measured the converted photocurrent using 2602 SourceMeter (Keithley, Cleveland, Ohio). Since only captured CD3+CD4+ cells are labeled with IgG-HRP, the measured current is proportional to the CD4 cell counts.

2.3 Results and discussion

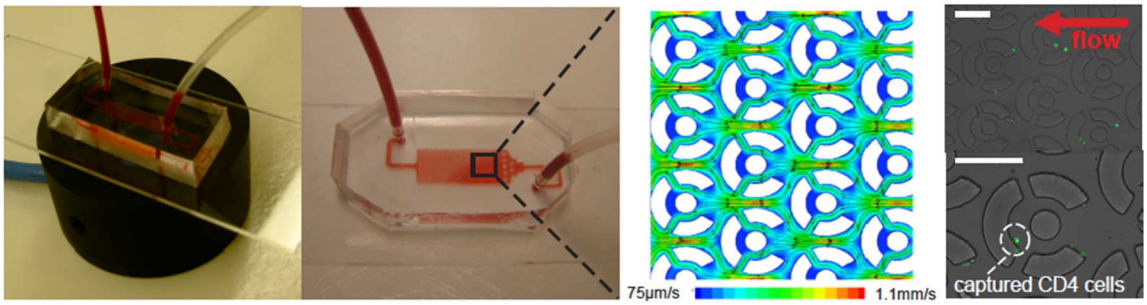

Figure 2.5: Images of microfluidic device, computational flow modeling and microtrap structures with captured cells. Pictures of a microfluidic chip on the photodetector (left), microfluidic chip with human whole blood inside (middle left), computational modeling of fluid flow inside the cell-capture chamber (middle right), and fluorescence micrographs of T-cells captured in the traps (right). The right panel shows the microtraps at 20x magnification (top) and 40x magnification (bottom). The green dots correspond to captured CD4 cells labeled with anti-CD3-IgG conjugated to Alexa Fluor 488. The fluorescence images of the stained cells sometimes appear speckled and hence may not reflect the true size of the CD4 cell. Size of cells measured under phase contrast was around 9-11 μm. The red arrow indicates the direction of flow when the blood sample and buffers were introduced into the chip. The scale bars are 100 μm.

Other works have reported that the optimal shear stress for the capture of CD4 cells fall within the range of 1-3 dyn/cm^2[11]. Computational modeling of fluid flow in our design shows that different regions of the microfluidic chamber exhibit shear stress within a range of 0.4-4 dyn/cm^2.

As shown in Figure 2.5, the CD4 cells tend to be captured at the regions of lower shear stresses and there are no cells remaining in the regions of higher shear stresses (both specifically and

non-specifically captured). The capture efficiency, or percentage of CD4 T-cells available for capture that were ultimately immobilized in the chip, was about 80%. Moreover, we observed that over 70% of captured T-cells reside in the low-flow rate areas near the traps. Hence, we concluded that the microfabricated pillars captured available T-cells with high efficiency, as intended by the microfluidic design.

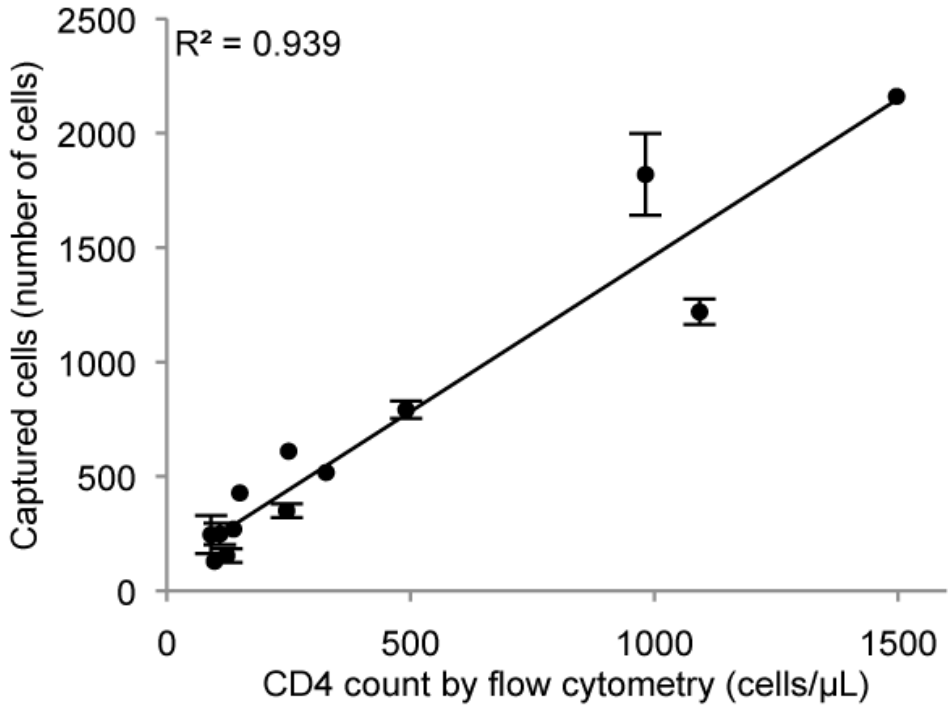

Figure 2.6: Plot of number of cells captured on microfluidic chip vs. CD4 count by flow cytometry. Quantification of captured T-cells from 3 μL of human whole blood using a microfluidic chip (as performed by manual counting of fluorescently labeled T-cells), as a function of CD4 counts obtained by flow cytometry. We ran samples with 13 different CD4 counts (ranging from 91 to 1497 cells/μL) with up to three replicates per data point. The standard deviations are shown.

Having verified the ability of the device to capture CD4+ T-cells, we tested the ability of the device to perform cell counting using chemiluminescence-based detection. We used a flow rate for chemiluminescent substrate (luminol and H_2O_2 mixture) of 5 μL/min (high flow rates led to shearing of captured cells, while low flow rates resulted in low signal). A silicon photodiode was

used to monitor the magnitude of the light from the chemiluminescence reaction as a function of time (Figure 2.5). Before the luminol/H_2O_2 mixture reached the capture chamber (□180 s), the measured current corresponded to the photodiode dark current. After □300 s, the measured current corresponded to the photocurrent generated by the light from the chemiluminescent reaction (for this set-up, a highly negative current corresponded to the generation of light). We analyzed a time-averaged signal of the photocurrent over 200 s toward the end of an 8 min period. Due to fluctuations in current, we found that the time-averaging of signal was critical. For example, CVs for raw current were very large, up to 82%, compared to 1-30% for time-averaged readings, depending on the amount of IgG-HRP used. We obtained excellent correlation between the measured photocurrent and CD4 counts (Figure 2.7), with a correlation coefficient of 0.99. The analysis of a total chemiluminescence signal emanating from many captured cells, rather than the optical signal from individual cells, could also compensate for any variations due to cell-to-cell variations in the expression of the CD3 marker

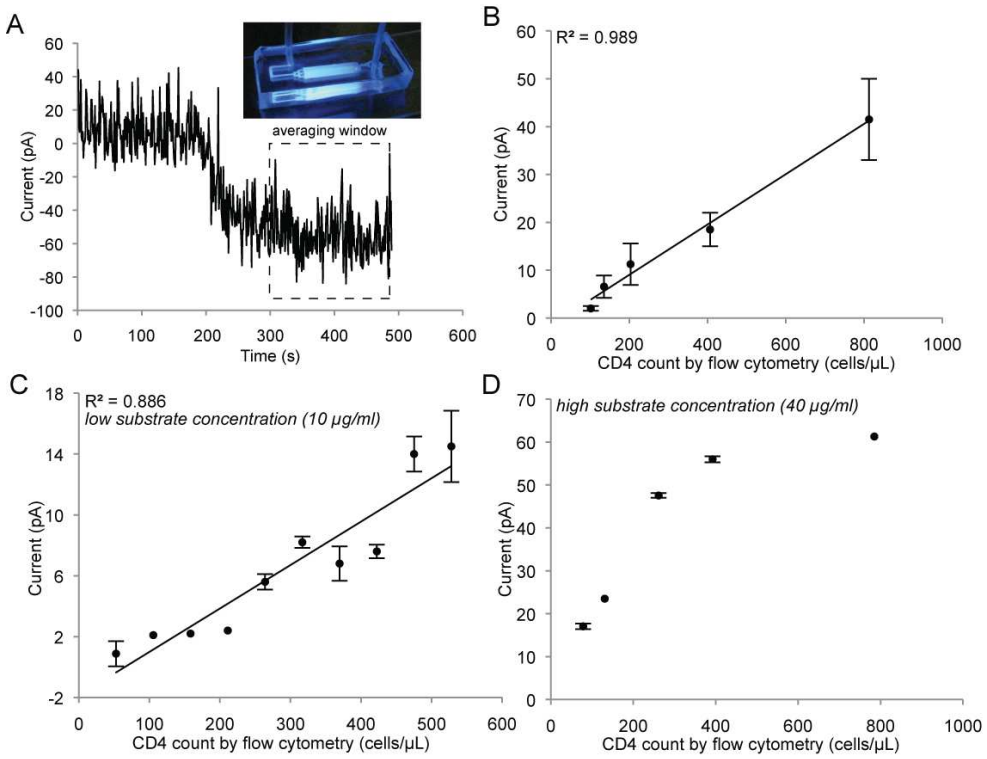

Figure 2.7: Detection of captured T-cells by chemiluminescence. (A) Plot of transient photocurrent observed during chemiluminescence-based detection. Following introduction of luminol and H_2O_2, photocurrent signals were collected for □8 min. The photocurrent from 0 to 200s was dark current and background noise, as little light was generated (while the substrate was reaching the capture chamber and the reaction was taking time to generate light). The photocurrent became negative upon detection of light. A time average of the last 200 s over the 8 min period was measured. (B) Plot of time-averaged photocurrent against CD4 counts obtained via flow cytometry. The concentration of IgG-HRP used during the blood staining process was varied from 20*μ*g/mL. There were two replicates per data point, and the standard deviations are shown. (C) Plot of time-averaged photocurrent against CD4 counts obtained via flow cytometry for two different concentrations of IgG-HRP. The concentration of IgG-HRP used during the blood staining process was varied from 20 to 10*μ*g/mL and 40 *μ*g/mL. Up to two replicates were performed for each data point, with the standard deviations shown.

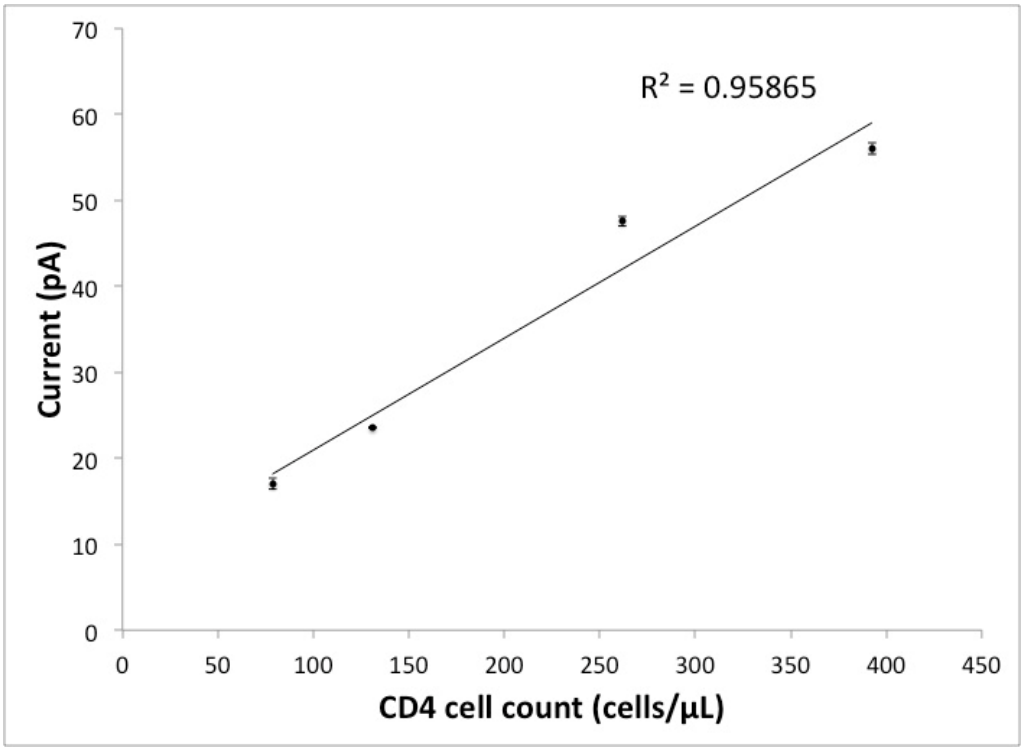

Figure 2.8: Plot of time-averaged photocurrents against CD4 counts obtained via flow cytometry using higher IgG-HRP concentrations. The graph shows a high correlation between the values at lower CD4 counts.

We also explored the possibility of shifting the linear range of detection by using different

concentrations IgG-HRP during blood immunolabeling. We observed that the overall correlation coefficient, for samples with cell counts ranging from 0 to 1500 cells/μL, decreased when we changed the concentration of IgG-HRP (during labeling of the T-cells) from 20 to either 10 μg/mL (due to reduction in the signal-to-noiseof the photocurrent) or 40 μg/mL (due to saturation in the amount of light as the oxidation reaction became increasingly substrate-limited) (Figure 6). Nevertheless, since the photocurrent can reach up to several hundreds of picoamps, our system can enumerate CD4 cells even at low CD4 counts by increasing the concentration of IgG-HRP, when low ranges of CD4 counts are of special interest (e.g., in following AIDS progression in diagnosed patients). In fact, if we were to plot the photocurrent values for samples with lower CD4 counts, we find that the coefficient of correlation increases to 0.95865 (Figure 2.8). Thus, this condition could be useful for precisely obtaining CD4 counts from patients who have a known HIV/AIDS status when low CD4 counts are expected. Next, we tested the accuracy of our calibration curves for predicting the positive or negative statuses of the patient. With the use of the two graphs where good correlation was observed across all cell counts (i.e., at 20 and 10 μg/mL of IgG-HRP) and 11 and 4.8 pA as the thresholds for diagnosis of AIDS (corresponding to the clinically significant 200 cells/μL threshold), our device displayed a sensitivity of 90.9% with a 95% confidence interval of 10.8% and a specificity of 100%. (Shifting our photocurrent thresholds would trade sensitivity for specificity, depending on the clinical need.) Hence, we believe this device exhibits the desired analytical features of a semi-quantitative POC diagnostic test that centers on the clinical thresholds around 200 cells/μL.

2.4 Conclusion.

We successfully demonstrated a proof-of-concept for performing chemiluminescence-based detection of CD4+ T-cells following specific capture on a microfluidic platform. This method shows great sensitivity and specificity, which can be further improved by using a higher concentration of HRP-linked antibodies. This technology is also highly amenable for

miniaturization as it does not external light-sources or sophisticated image/data analysis methods. Future work would include incorporating fluid-management into the microfluidic device to enable on-chip labeling of CD4+ cells with IgG-HRP. Possible complications from this are having low signal-to-noise ratios due to the very sensitive nature of chemiluminescence techniques to background noises, eg: residual IgG-HRP in the incubation chambers. Therefore, a multi-chamber design coupled with fluidic handling techniques (microfluidic valves) should be incorporated in future iterations of this device to enable on-chip labeling of whole blood before capture and detection is carried out downstream.

This work was completed and published as "Microfluidic CD4+ T-cell counting device using chemiluminescence-based detection. **Anal Chem, 2010. 82(1): p. 36-40"** ***[36].***

Chapter 3

PEGDA as a viable biomaterial for MEMS devices

3.1 Introduction

Hydrogels have been extensively used for biomedical engineering applications mainly due to their biocompatibility and material characteristics which are similar to biological tissues[37-39]. Due to the permeability of the polymer networks of hydrogels, they are often used for the encapsulation of drugs and cells. The have become ideal scaffolding and encapsulation material for tissue engineering [40-42]. Hydrogels have also garnered great interest in the drug delivery community with numerous efforts on using hydrogels as a vector for the controlled-release of therapeutics[43-45]. It is possible to tune the material properties of hydrogels, which in turn results in controllable release profiles for drug-loaded hydrogels[46-48].

One class of hydrogels that are of interest is PEG-based gels, specifically polyethylene glycol diacrylate (PEGDA). PEG is an FDA approved material[49] for use in humans as they are highly biocompatible and display very little to no immunogenicity. PEGDA hydrogels are photopolymerizable[50, 51], and have easily tunable mechanical[52] and diffusive properties[53]. Various implantable PEGDA structures have been developed[54, 55] as well as devices that are coated with PEG-based hydrogels to improve their biocompatibility and prevent biofouling [56-58].

Therefore, due to its versatility and superior biocompatibility, we postulate that PEGDA would be an ideal building material for implantable MEMS devices. This would introduce a new paradigm of implantable biomedical devices that do not contain silicon, metals and are entirely biocompatible as well as potentially biodegradable. Biocompatible materials have been

developed to replace older implantable technologies (biodegradable suture, orthopedic implants, stents)[59-61] and we believe the same can be done for medical devices. However as hydrogels are typically used as “soft” materials, we first have to characterize and tune the properties of PEGDA to ensure that they are viable candidates for building robust MEMS devices.

3.2 Mechanical stiffness of PEGDA

Mechanical stiffness is an important criterion for selecting a PEGDA composition suitable for the fabrication of robust moving components within a MEMS-like device as. In general, a minimum level of stiffness is required to ensure robust movements/actuation within a MEMS device. Materials that are too “soft” or brittle would not be practical as they would not be able to withstand wear and tear with continued use. Also, the exterior surface of the device has to have be able to protect its interior components from its surrounding environments and any mechanical perturbations that may occur during normal movement after implantation. The incorporation of PEGDA gels with lower mechanical stiffness that tend to be more flexible would also lend more capabilities; much like flexible elastomers used as valves or snap-fits. A mismatch in stiffness between interfacing surfaces could also aid precise movement of components (see Chapter 4.1.2, Locking mechanism).

Here, we show that we are able to achieve a wide range of stiffnesses by varying the length of the PEG chain as well as the concentration (w/v%) of PEG used (Table 1). The Young’s moduli achieved are in line with what would be expected from these compositions as tested on macroscale gels.

3.2.1 Methods

PEGDA hydrogels of various molecular weights and percentages (weight/volume) were mechanically tested and their respective Young's Moduli were calculated.

Materials. Polye(ethylene glycoly)-diacrylate (PEGDA, MW: 20kDa and 10kDA) was purchased from Laysan Bio, Inc (Arab, AL). PEGDA (MW: 400Da, and 4kDA) and ProMag™ Superparamagnetic Microspheres (dia: 3μm) were purchased from Polysciences (Warrington, PA). Darocur 1173 and Irgacure 2959 photoinitiators were purchased from Ciba Specialty Chemicals (Basel, Switzerland). 3-(trimethoxysilyl) propyl methacrylate (TMSM), 1-vinyl-2-pyrrolidone (NVP), Rhodamine B, Fluorescein, TRITC-dextran (3kDa, 20kDa, 155kDa) and FITC-dextran (3kDa, 20kDa and 155kDa) were purchased from Sigma (Milwaukee, WI). Polydimethylsiloxane (PDMS) is purchased from Dow Corning (Midland, MI). High intensity UV lamp (OMNICURE 2000 system, Model S2000) was purchased from The Lumen Dynamics Group Inc. (Ontario, Canada). All reagents were used without further purification.

Unpolymerized PEGDA mixtures (prepolymer) were prepared at different compositions. These compositions, various combinations of molecular weight of PEGDA chain, percentage of PEGDA (% weight/volume), photoinitiators and accelerators, are summarized in Table 3.1.

Molecular weight of PEGDA chain (Da)	Percentage (weight/volume) of PEGDA in prepolymer	Other additives
400	20%, 50%, 60%, 70%, 80%, 90%, >99%	1% (v/v) Darocur 1173
4k	5%, 10%, 20%	1% (v/v) Irgacure 2959 + 0.2% (v/v) NVP
10k	5%, 10%, 20%	1% (v/v) Irgacure 2959 + 0.2% (v/v) NVP
20k	5%, 10%, 20%	1% (v/v) Irgacure 2959 + 0.2% (v/v) NVP
400 + 4k	5% and 10% respectively	1% (v/v) Irgacure 2959 + 0.2% (v/v) NVP

Table 3.1: Different compositions of PEGDA hydrogels tested.

Briefly, all prepolymer compositions also included 0.2% (v/v) NVP (Sigma-Aldrich) and 1% (w/v) I2959 (Irgacure). This is with the exception of gels composed of 400Da PEGDA, where 1% Darocur 1173 was used instead. This is due to the different solubilities of the two photoinitiators used. It was found that Irgacure 2959 was not as miscible in 400Da PEGDA polymers compared to Darocur 1173. This resulted in 400Da PEGDA gels polymerized with Irgacure 2959 becoming very brittle. This could be due to the non-uniform polymerization of the gel due to the poor miscibility of the photoinitiator

Each prepolymer composition was polymerized using a collimated UV light source (Omnicure S2000, EXFO) and a transparency mask was used to define the shape of each gel (more detailed description of this photolithography method is described in Chapter 3). Disks ($n \geq 3$) of 10mm in diameter and 1mm thick were fabricated for each gel composition. After swelling in PBS (>24 hours), unconfined compression tests were then performed on these hydrogels to determine their mechanical stiffness using an Instron 8841 mechanical testing machine. Each disk was placed on the stage of the Instron and the platens was lowered such that it just made contact with the hydrogel and a small load is detected by the load cell (<0.1N). A strain of 20% was applied to each gel disk at a rate of 0.02mm/s (10% of total displacement per second). The integrated software was used to track the displacement of the platens and the readings of the load cell. A stress strain curve was then obtained from these values and the Youngs Modulus for each gel was obtained. The compression tests were performed on some select gel compositions over a period of 2 weeks in order to assess their mechanical strengths over time. The gels were left in PBS in between testing.

3.2.2 Results and discussions

For each gel composition, stress and strain values were calculated based on the dimensions of the gels as well as the load and displacement data as recorded by the Instron. Stress strain

curves were then plotted for each gel. Figure 3.1 is an example of a stress-strain curve obtained for a 5% (w/v) 400Da PEGDA gel after mechanical testing.

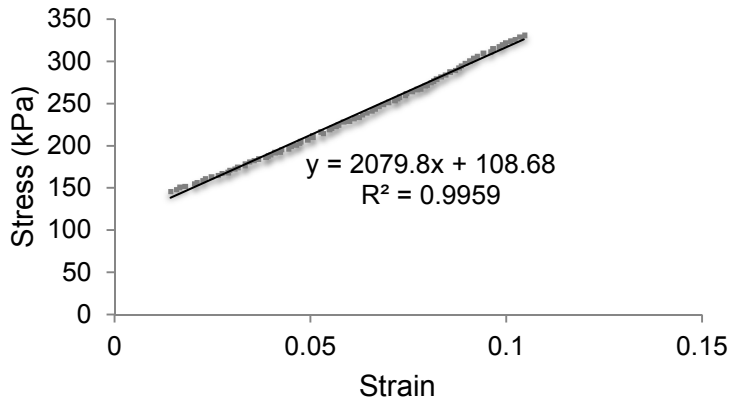

Figure 3.1: Stress-strain curve. This plot is obtained by calculated stress and strain values from displacement and load values applied by the platens during mechanical testing. A linear fit is applied to the curve and the slope of the curve is obtained.

The Youngs Modulus for each gel composition was obtained from the slope of the stress-strain curve using the following equation:

$$Young's\ Modulus = \frac{(Equilibrium\ load - Preload)/Surface\ area\ of\ disk}{\%\ Strain\ applied}$$

The Young's Moduli for the various compositions are summarized in Figures 3.2 and 3.3. Figure 3.2 shows the Young's Moduli of 400Da PEGDA gels with increasing percentages while Figure 3.3 shows the effect of increasing chain lengths of PEGDA on the Young's moduli of the gels. As can be seen from both figures, increasing the percentage of PEGDA in the prepolymer solution increases the Young's modulus of the resulting gel. On the other hand, Figure 3.3 shows that increasing the molecular weight of the PEGDA used (ie: increasing chain lengths) would decrease the Youngs modulus of the gel.

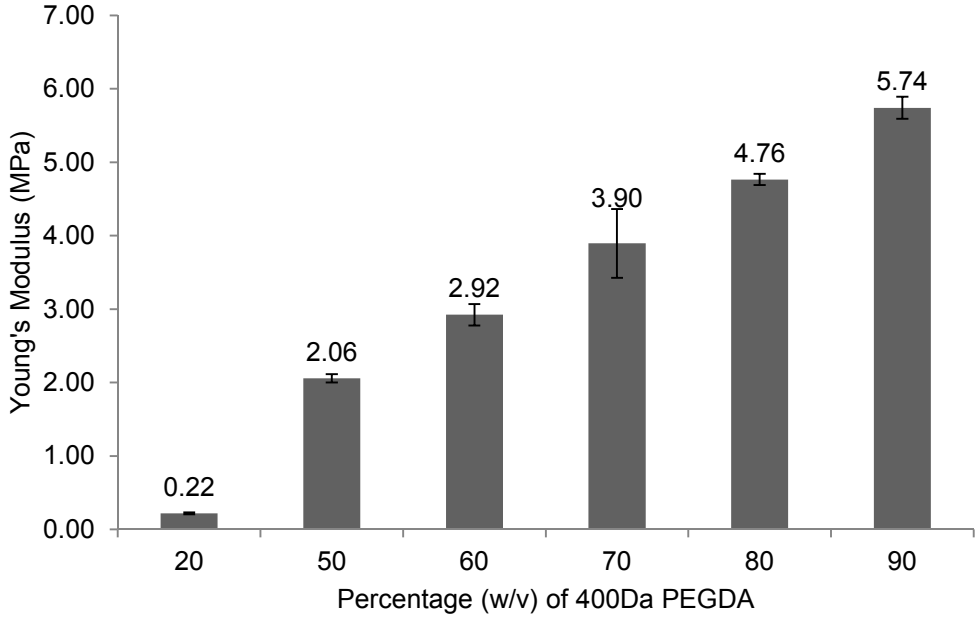

Figure 3.2: Young's Modulus of 400Da PEGDA with increasing percentages of PEGDA in prepolymer.For each gel type, n=4

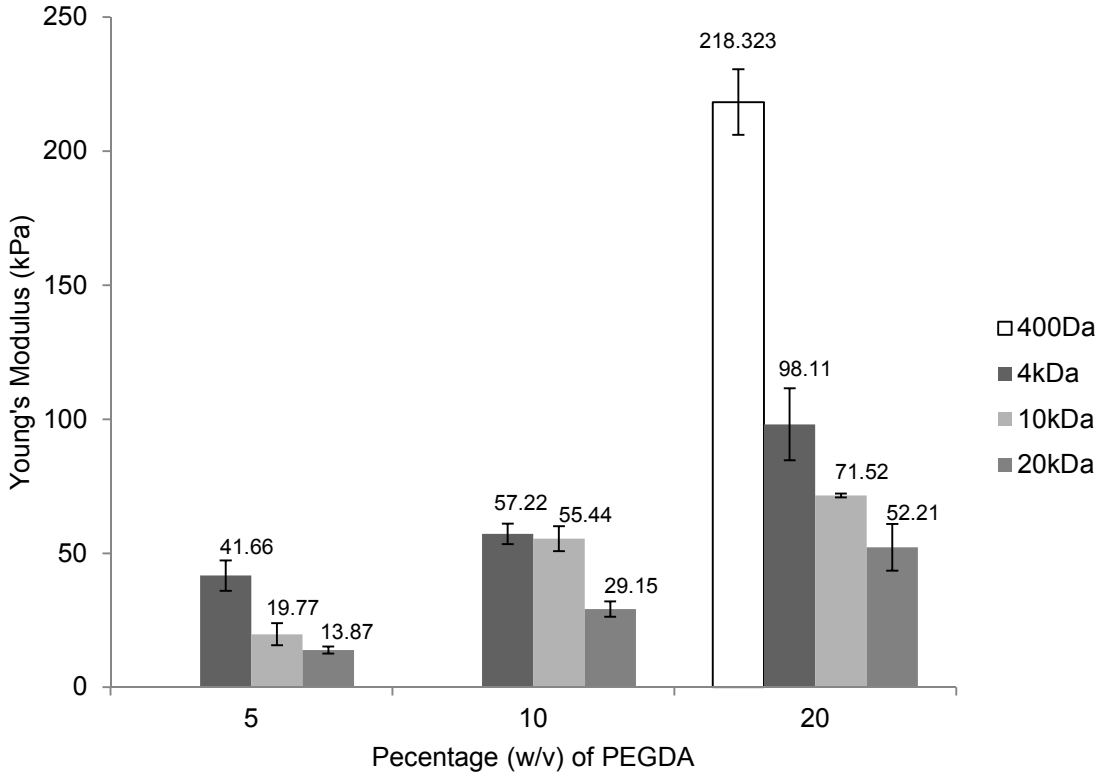

Figure 3.3: Young's Modulus of PEGDA gels with various molecular weights and percentage PEGDA. n=3 for each gel type except for 400Da PEGDA at 20%, where n=4.*Note: 400Da PEGDA at 5% and 10%*

(w/v) PEGDA were not tested. Gels became opaque at these percentages and hence could not be completely cross-linked by UV.

Next, we tested a select set of PEGDA gels (gel compositions given in Table 3.2) that had a large range of Young's moduli over a period of 2 weeks. As shown by Figure 3.4, we can see that the mechanical integrity of the gels were not compromised over time.

Gel name	Gel composition	Additive
PEG400	>99% 400Da PEGDA	1% (v/v) Darocur 1173
PEG4k	10% 4kDa PEGDA + 5% 400Da PEGDA	1% (v/v) Irgacur 2959+ 0.2% (v/v) NVP
PEG10k	5% 10kDa PEGDA	1% (v/v) Irgacur 2959+ 0.2% (v/v) NVP
PEG20k	5% 20kDa PEGDA	1% (v/v) Irgacur 2959+ 0.2% (v/v) NVP

Table 3.2: Composition of PEGDA hydrogels used for assessing Young's modulus over time.

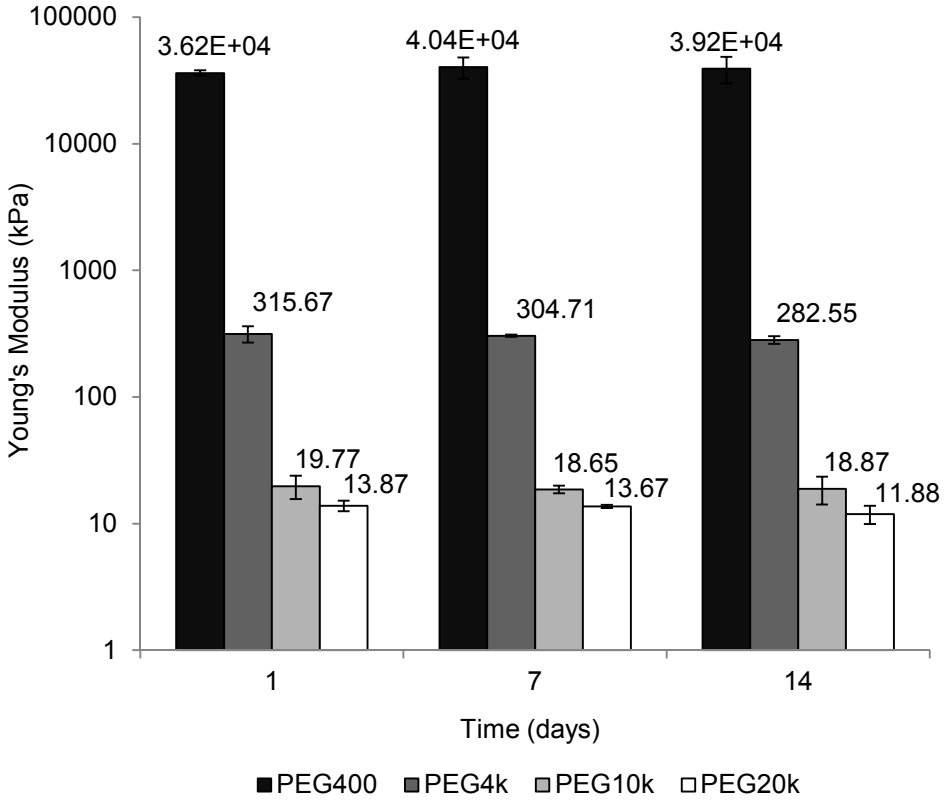

Figure 3.4: Young's modulus of PEGDA gels over time. These compositions were selected to cover a wide range of stiffnesses. n=3 for each gel type. *Note: logarithmic y-axis used.*

As can be seen from these values, we are able to achieve a large range of stiffnesses by changing the composition of the hydrogels; the stiffnesses range from the order of 10kPa (comparable to soft tissues) to 10MPa (comparable to rubber). In general, the mechanical strength of the hydrogel increases with decreasing chain length of PEGDA. This is because, for the same weight percentage of PEGDA, as the chain length decreases there is a higher extent of crosslinking for every repeat on the PEG chain. Also, the mechanical strength increases with increasing weight percent of PEGDA used as a denser network is formed after polymerization[62]. Thus, in this manner one can easily tune the Young's modulus of gels by changing factors that would affect the cross-linking density of the gel. Also, it is noted we can fine-tune these stiffnesses further by using combinations of PEGDA with different chain lengths. In the case of PEG4k, which is a combination of 4kDa PEGDA (10% w/v) and 400Da PEGDa (5% w/v), we are able to increase the resulting Young's modulus by about 6 times compared to that of gels composed of 10% (w/v) 4kDa PEGDA alone. This wide range of Young's moduli is useful as different materials of different stiffnesses can be utilized to serve different functions within a MEMS device (See Chapter 4, Locking mechanism).

3.3 Diffusive properties of PEGDA

PEGDA has a porous network structure that allows for diffusion of small molecules. The porosity of PEGDA can be tuned depending on the percentage of PEGDA used as well as the length of the PEG chain as these two factors affect the cross linking density in the resulting hydrogel. Being able to tune the rate at which substance diffuse across the network is important especially if the hydrogel-based MEMS device were to be used for drug delivery applications (see Chapter 4). In this instance, we could change the release kinetics of the drug from the device by changing the permeability of the hydrogel or have the hydrogel be totally impermeable to the drug so as to be able to contain its payload. Here's we characterize the diffusive properties of PEGDA via two methods.

The first method employed is fluorescence recovery after photobleaching (FRAP) as measured as a function of time and space by means of confocal laser scanning microscopy[63]. Using this method, we are able to represent one-dimensional diffusion from a plane source by irreversibly bleaching a line through a fluorescent sample and then measuring fluorescence recover curves that are orthogonal to this bleached line.

A second method employed is to encapsulate fluorescent-conjugated dextrans in hydrogels and measure the release of these dextrans over time from the hydrogel constructs. This method assesses both the diffusive property of the gels as well as the effectiveness of our fabrication technique in fully encapsulating liquid materials.

3.3.1 Method

3.3.1.1 Fluorescence Recovery After Photobleaching.

FRAP experiments were performed to obtain the diffusion coefficient of the gels. FITC-conjugated dextran with a molecular weight of 3kDa was purchased from Invitrogen while FITC-conjugated dextrans with molecular weights of 20kDA and 155kDa were purchased from Sigma Aldrich. In order to ensure the adhesion of PEGDA hydrogels to the glass slides, to prevent movement during imaging, the glass slides were first treated with TMSM. The slides were immersed in 10% (v/v) TMSM in 100% ethanol for an hour followed by rinsing with DI water. This functionalizes the surface of the glass with methacrylate groups and will promote the adhesion of PEGDA hydrogels on the surface. Figure 3.5 describes the gel preparations and incubations prior to FRAP experiments. The gels of interest are then polymerized on TMSM treated glass slides using 5mmx5mm photomasks. The polymerized gel is then immersed in solutions of FITC-conjugated dextran.

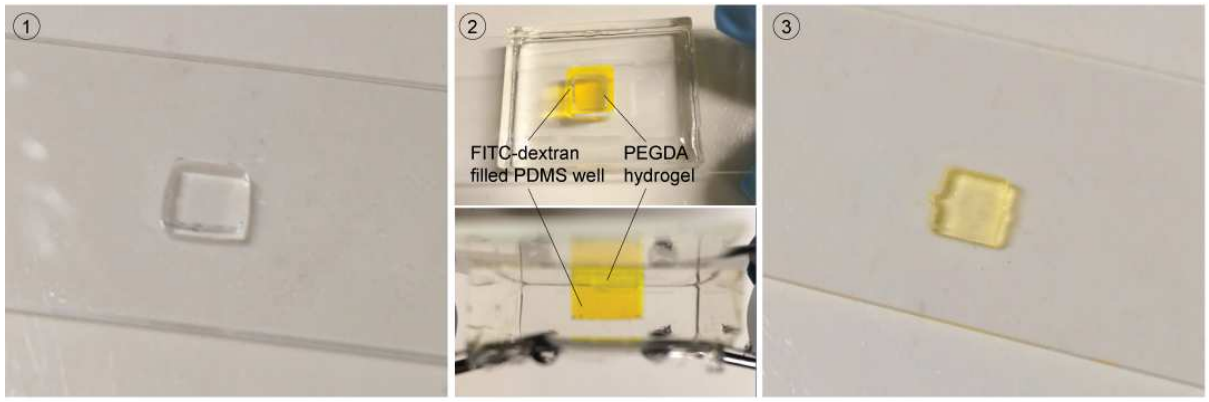

Figure 3.5: Preparation of PEGDA hydrogels for FRAP experiments. 1) PEGDA hydrogels are polymerized to form a 5x5x0.5 mm slabs that are adhered to TMSM-treated glass. 2) PDMS wells (8x8x5mm) were filled with FITC-dextran solutions of various molecular weights (3kDa, 20kDa, 155kDa). The glass slides with PEGDA gels adhered on their surfaces were then placed over these wells with the gel in contact with the FITC-dextran solutions. The glass slide and PDMS wells were then clamped together with binder clips and the gels were allowed to incubate in the FITC-dextran solutions overnight. 3) After incubation, the PEGDA gels were rinsed with PBS to remove any excess FITC-dextran solutions and FRAP experiments were conducted on them.

After overnight incubations, the gels were rinsed of excess FITC-dextran with PBS and FRAP was performed on the gels using a Leica TCS SP5 Confocal and Multiphoton Microscope. A 488nm Argon laser was used to form a bleached region on the gel (95% power) as well as to image (6% power) the gel. A high power laser was used to irreversibly bleach the region to ensure that recovery of fluorescence in the region was due purely to diffusion of unbleached fluorophores into the bleached region. A lower power was used for imaging to ensure no further bleaching took place. Time-lapse images of the hydrogel as the bleached zone recovers its fluorescence were then captured. A 1-D diffusion model was used to approximate the associated diffusion coefficient[63, 64].

1-D diffusion model. For the case where diffusing species are initially localized to a plane within an infinite medium, diffusion takes place in the dimension orthogonal to the plane. For

one-dimensional cases, when diffusion occurs only in the x-direction, the diffusion equation, or Fick's second law, is give as:

$$\frac{\partial C}{\partial t} = D\frac{\partial^2 C}{\partial x^2}$$

where C is the concentration of the diffusing species, D is the diffusion coefficient, t is the time of diffusion and x is the distance from the plane. When the diffusing substance is localized in a plane within an infinite medium at time t=0, the solution to Fick's second law is:

$$C(x,t) = \frac{M}{2\sqrt{\pi D t}}\exp\left(\frac{-x^2}{4Dt}\right)$$

M is the total amount of diffusing species per unit area. 1-dimensional diffusion can be modeled by bleaching a line through a sample, and fitting the intensity profile orthogonal to the bleach line to the following equation:

$$I(x,t) = I_0 - \frac{M}{2\sqrt{\pi D t}}exp\left(\frac{-x^2}{4Dt}\right) = I_0 - A(t)exp\left(\frac{-x^2}{w^2}\right);\ w^2 = 4Dt$$

where I is the fluorescence intensity, M is the fluorescence intensity per unit area (corresponding to the amount of bleached fluorophore), D is the diffusion coefficient, x is the pixel position relative to the bleach line, w is the full width at half maximum of the Gaussian function and t is the time after bleach. Raw images obtained after FRAP experiments were processed using imageJ. Using a MATLAB code, processing the images yielded plots of w^2 versus t. Diffusion coefficient values were obtained from the slope of these plots.

3.3.1.2 *In vitro* dextran release from hydrogel encapsulated systems.

In order to characterize the permeability of the gels used, experiments were performed to measure the diffusion of fluorescently labeled dextran molecules out of and through the gels on

a larger scale. Briefly, fluorescent-conjugated dextrans in solution were encapsulated within hydrogel constructs. These constructs are fabricated with voids into which solutions can be injected. The constructs are then sealed without any inadvertent polymerization of the injected material. In this way, we do not risk changing or affecting the composition of the injected material/drug. This is in contrast with other hydrogel encapsulation techniques which require that the drug be incorporated into the prepolymers and then polymerized in situ with the bulk of the material[65-67]. These techniques would not only potentially affect the material that is being encapsulated but would also affect the amount of material that can be released should they become trapped in non-interconnective pores of the polymer network.

In the study of the release of material from these hydrogel constructs, we will also be able to compare the calculated diffusion coefficients with that obtained from the FRAP experiments. We postulate that any discrepancies found would due to the fabrication technique as a whole. For example, improper sealing of voids within structures during fabrication could cause breaches or leaks in the hydrogel.

Fabrication of dextran-filled hydrogel "boxes". Hydrogel constructs were fabricated using various PEGDA compositions following the steps detailed in Figure 3.6. This construct measures 10mmx10mmx1.1mm and is formed with an internal void measuring 6mmx6mmx0.7mm. The top and bottom layers are 200μm thick while the sidewalls are 2mm thick all around. A fine gauge needle is used to remove any uncrosslinked polymer as well as to inject TRITC conjugated dextrans of various molecular weights before a final sealing step. These constructs were then incubated in PBS at 37^{o}C under gentle agitation for up to 30days. Samples were taken daily from the solution surrounding the constructs and the amount of TRITC-dextran that diffused out of the construct were quantified by fluorescence readings using a BioTEK microplate reader (Excitation wavelength: 557nm, Emission wavelength: 576nm)

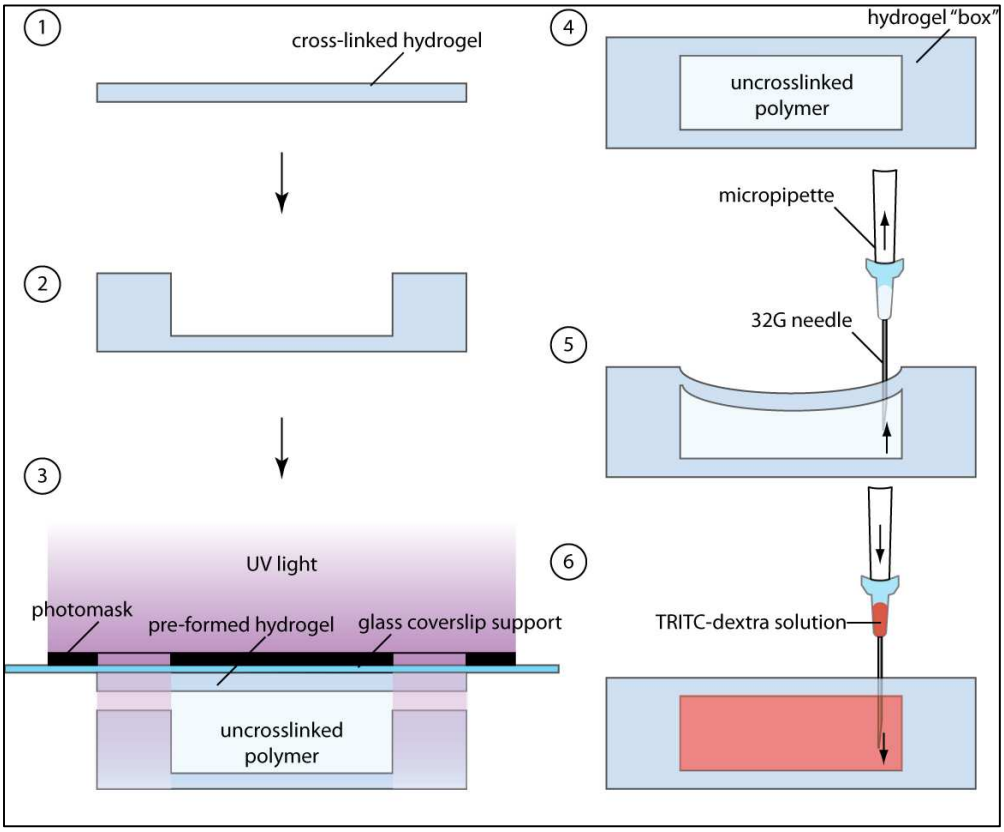

Figure 3.6: Fabrication steps for dextran-filled hydrogel constructs for *in vitro* release experiments. (1) A bottom layer of 200μm thick hydrogel was first formed (10mmx10mm). (2) A frame of height 700μm was then formed with a 2mm thickness all around (outer dimensions:10mmx10mm, inner dimensions: 6mmx6mm). (3) A pre-formed slab of hydrogel of 200μm thickness (1mmx1mm) is then layered on top of this structure using a glass coverslip as a support. More prepolymer was added and the construct was sealed. (4) A hydrogel "box" measuring 10mm x 10mm x 1.1mm is formed with a void (6mm x 6mm x 0.7mm) that is filled with the uncrosslinked prepolymer. (5) Using a 32G needle attached to a micropipette, the uncrosslinked polymer is removed. (6) In the same manner, TRITC conjugated dextran of various molecular weights was then injected into the void. A final sealing layer is applied by layering a thin pre-formed layer of hydrogel on top of the injected construct followed by UV polymerization (not shown in figure).

3.3.2 Results and Discussions

3.3.2.1 Fluorescence Recovery after Photobleaching

Figure 3.7 shows an example of a subset of raw images obtained from FRAP experiments Following image processing (ImageJ, NIH) and analysis using a MATLAB code, plots of w^2 versus time were obtained.

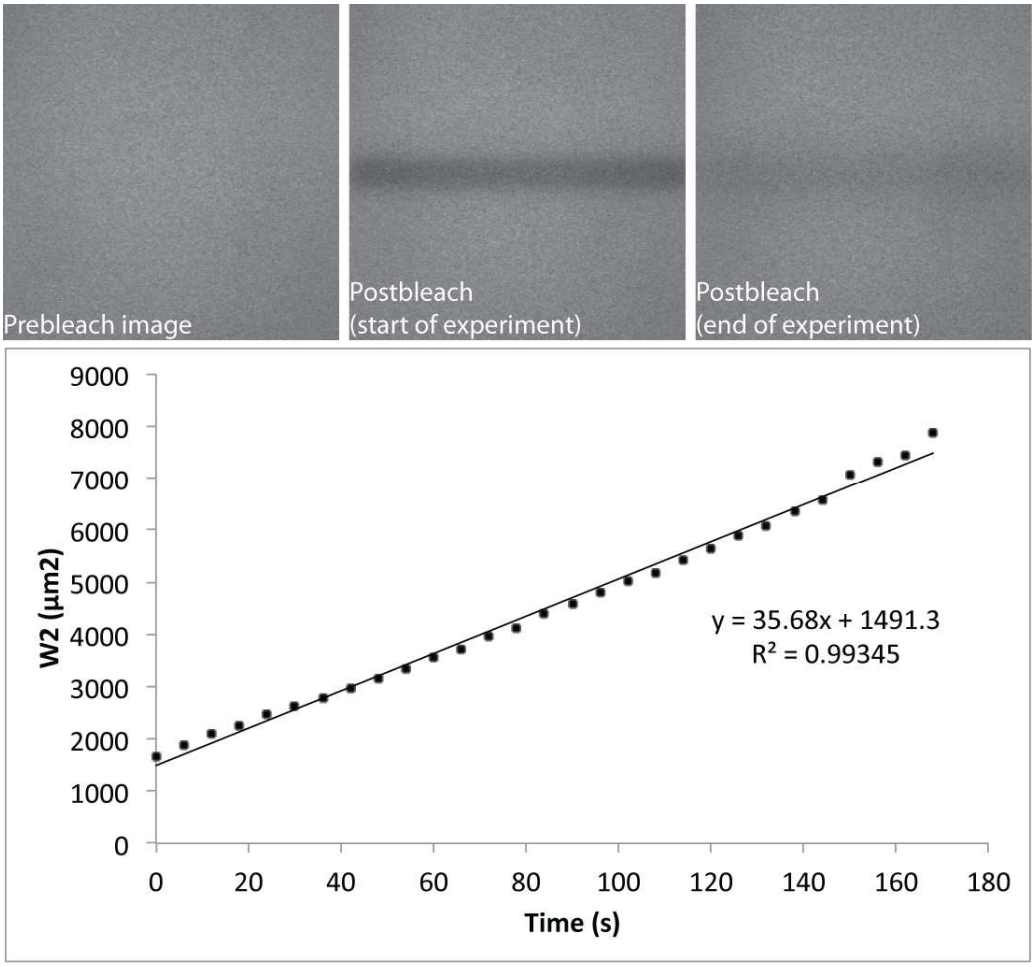

Figure 3.7: Example raw images obtained during FRAP experiments and subsequent plots to obtain associated diffusion coefficients. The top panel shows 3 images from the set of raw images obtained during FRAP experiments on 10k5 hydrogels incubated with 150kDa FITC-dextran. The prebleach image shows the fluorescent image of the gel prior to photobleaching using the Argon laser. The middle image shows the first fluorescent image of the gel at the same location immediately after the gel was photobleached in the region of interest. The image on the right is the

last fluorescent image in the series of time-lapse images and the photobleached zone can be seen to recover its fluorescence. The plot below is generated after the images have been processed and analyzed using a MATLAB code and is a measure of how quickly the fluorescent signal is recovered in the bleached zone. The diffusion coefficient of the gel can be obtained from the slop of this graph.

The diffusion coefficient, *D*, for each combination of gel type and diffusing species (TRITC-dextran) was obtained from the slope of their individual w^2 plots. The results of these FRAP experiments are summarized in Table 3

Name of hydrogel	Diffusion coefficient (D, cm^2/s)		
	3kDa dextran	20kDa dextran	155kDa dextran
PEG400	Below LOD ($<10^{-9}$)	Below LOD ($<10^{-9}$)	Below LOD ($<10^{-9}$)
PEG4k	$4.7 \pm 0.8 \times 10^{-7}$	$1.0 \pm 0.1 \times 10^{-7}$	Below LOD ($<10^{-9}$)
PEG10k	$1.2 \pm 0.2 \times 10^{-6}$	$5.9 \pm 0.9 \times 10^{-7}$	$8.7 \pm 1.1 \times 10^{-8}$
PEG20k	Above LOD ($>10^{-5}$)	$5.3 \pm 0.9 \times 10^{-7}$	$2.5 \pm 0.5 \times 10^{-7}$

Table 3.3: Diffusion coefficients, D, of PEGDA hydrogels as obtained from FRAP experiments. LOD: Limit of detection. n=3 for each gel type.

As can be seen from Table 3.3, the values of D decrease as the molecular weight of the diffusing species (dextran) increases and as the MW of the PEGDA chain decreases. This is because as the extent of crosslinking increases the porous network becomes denser and the porosity of the hydrogel decreases, hence inhibiting the diffusion of dextran. In fact, for the PEG400 gels, FRAP experiments could not be performed because after incubation with FITC-dextran solutions the hydrogel did not uptake any FITC-dextran and little to no fluorescence was observed when the gel was imaged. Increasing the incubation time to 3 days yielded the same result. We also tried incubating the PEG400 gels with unconjugated FITC solutions (MW= 389Da) and the gels still did not uptake enough fluorescence for FRAP experiments. For our purposes, these gels are considered to be impermeable to molecular weights of 389Da or higher.

3.3.2.2 *In vitro* dextran release from hydrogel encapsulated systems.

We then measured the cumulative amount of TRITC-dextran that diffused out of the construct in the in vitro diffusion experiments. These values were then expressed as the percentage of the total injected dextran in the construct that diffused out. Table 4 summarizes the results of those set of experiments.

Name of hydrogel	Release of dextran (%mass released)		
	3kDa dextran	20kDa dextran	155kDa dextran
PEG4k	63.4 ± 5.4 (t=31 days, n=8)	28.3 ± 5.2 (t=33 days, n=8)	6.0 ± 0.9 (t=49 days, n=7)
PEG10k	71.3 ± 6.8 (t=34 days, n=7)	36.8 ± 9.5 (t=15 days, n=6)	18.1 ± 2.6 (t=20 days, n=2)
PEG20k	78.4 ± 16.5 (t=34 days, n=4)	79.2 ± 9.6 (t=21 days, n=8)	50.6 ± 1.7 (t=31 days, n=3)

Table 3.4: Percentage of the total mass of dextran encapsulated in the constructs that were released over time.

We manage to achieve a minimal baseline diffusion of 6.0 ± 0.9% for the combination of PEG4k hydrogel and 155kDa dextran. The trend that we observe from the in vitro diffusion experiments is similar to that of the FRAP experiments; percent mass released and D decreases with decreasing MW of the PEG chain. The amount of dextran that diffuses out of the hydrogel construct is a result of the permeability of the hydrogel as well as any imperfections in the construct due to the fabrication process. Thus, the baseline diffusion of dextran out of the most impermeable gel that we have is reflective of the limit of our fabrication process. PEG400 gels were not tested in these experiments. It was observed that these constructs would deform after incubation in PBS due to osmotic pressure. Most of our gel compositions were able to withstand some level of deformation due to their elastic nature. However, PEG400 gels are not elastic and would not be able to withstand this deformation. As a result, they would crack and/or delaminate due to osmotic pressure.

In order to compare these the data collected from our FRAP experiments and the percentage mass of dextran released from constructs over time, we then calculated the effective diffusion

coefficients for each PEGDA construct tested. To achieve this, we used early-time and late-time approximation equations for solving Fick's second law of diffusion[68, 69]

Once again, Fick's second law may be written as:

$$\frac{\partial C}{\partial t} = D\frac{\partial^2 C}{\partial x^2}$$

where:

$t = 0\ , -\frac{l}{2} < x < \frac{l}{2}\ , C = C_1$

$t > 0\ , x = \pm\frac{l}{2}\ , C = C_0$

l is the thickness of the construct, $C_1$is the initial concentration of diffusing species, C_0 is the concentration at the surface at the surface of the construct (maintained at a constant). The solution of Fick's law in the form of a trigonometric series under these conditions:

$$\frac{M_t}{M_\infty} = 1 - \sum_{n=0}^{\infty} \frac{8}{(2n+1)^2\pi^2} exp\left[-\frac{D(2n+1)^2\pi^2}{l^2}t\right]$$

M_t is defined as the mass of material released over time and M_∞ is the mass of material released as time approaches infinity. Expressing this equation in the form of an error function series gives us:

$$\frac{M_t}{M_\infty} = 4[Dt/l^2]^{1/2}\left[\frac{1}{\pi^{\frac{1}{2}}} + 2\sum_{n=1}^{\infty}(-1)^n ierfc\frac{nl}{2\sqrt{Dt}}\right]$$

$ierfc\ x$ represents the integrated complementary error function for x. For "short times" this equation can be approximated by:

$$\frac{M_t}{M_\infty} = 4\left[\frac{D_{eff}t}{\pi l^2}\right]^{1/2}$$

This early-time approximation is valid for the first 60% of the total released material ($\frac{M_t}{M_\infty} \leq 0.60$). D_{eff} is the effective diffusion coefficient for our constructs. For late-time approximations, the following equation can be used:

$$\frac{M_t}{M_\infty} = 1 - \frac{8}{\pi^2} exp\left(-\frac{\pi^2 D_{eff}t}{l^2}\right)$$

$$\log\left(1 - \frac{M_t}{M_\infty}\right) = -\frac{\pi^2 D_{eff}t}{l^2}\log\left(\frac{\pi^2}{8}\right)$$

Therefore by plotting $\frac{M_t}{M_\infty}$ vs $t^{1/2}$ for early-time approximations and $\log\left(1 - \frac{M_t}{M_\infty}\right)$ vs t for late-time approximations, we were able to obtain the effective diffusion coefficients for these constructs D_{eff}. Figures 3.8 and 3.9 shows examples of plots used to obtain the effective diffusion coefficients.

A)

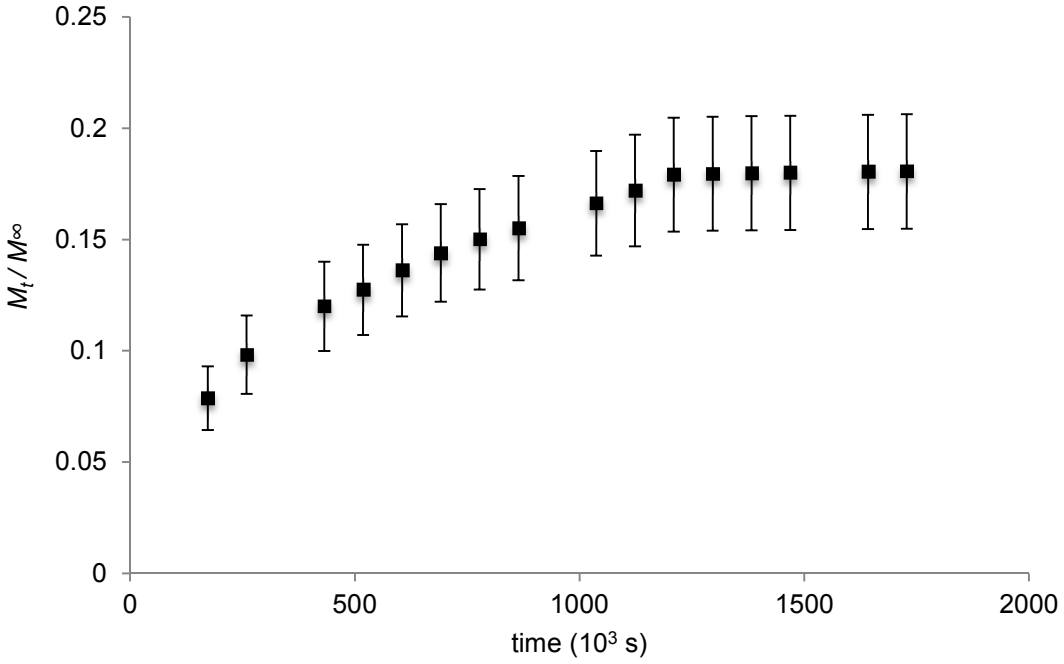

B)

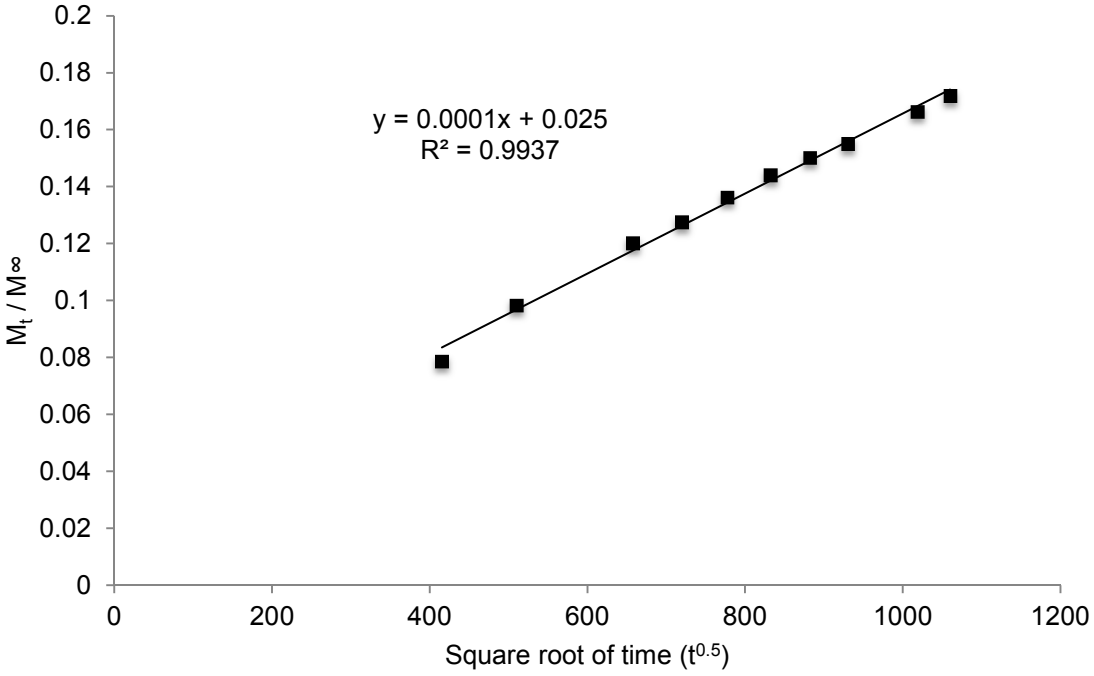

Figure 3.8: Graphs for early-time approximation of effective diffusion coefficient, D_{eff}. A) Plot of M_t/M_∞ vs. time for 155kDa TRITC-dextran encapsulated in PEG10k hydrogel constructs. B) Corresponding plot for M_t/M_∞ vs. the square root of time. The slope of this graph was used to calculate D_{eff} =9.6 x 10^{-8}cm^{2}s^{-1}

A)

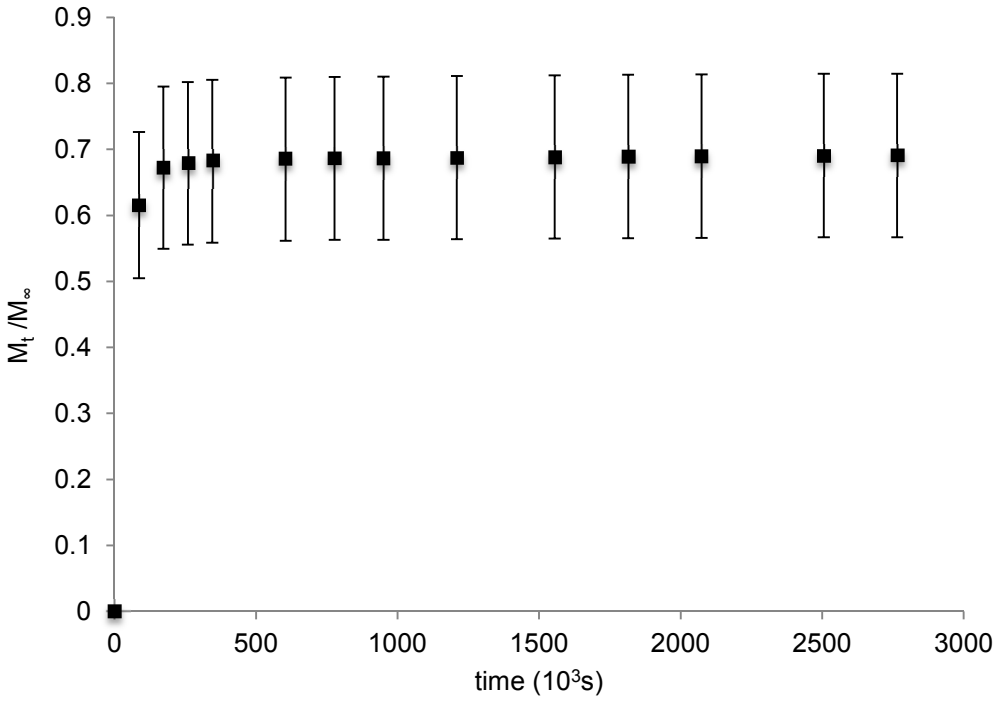

B)

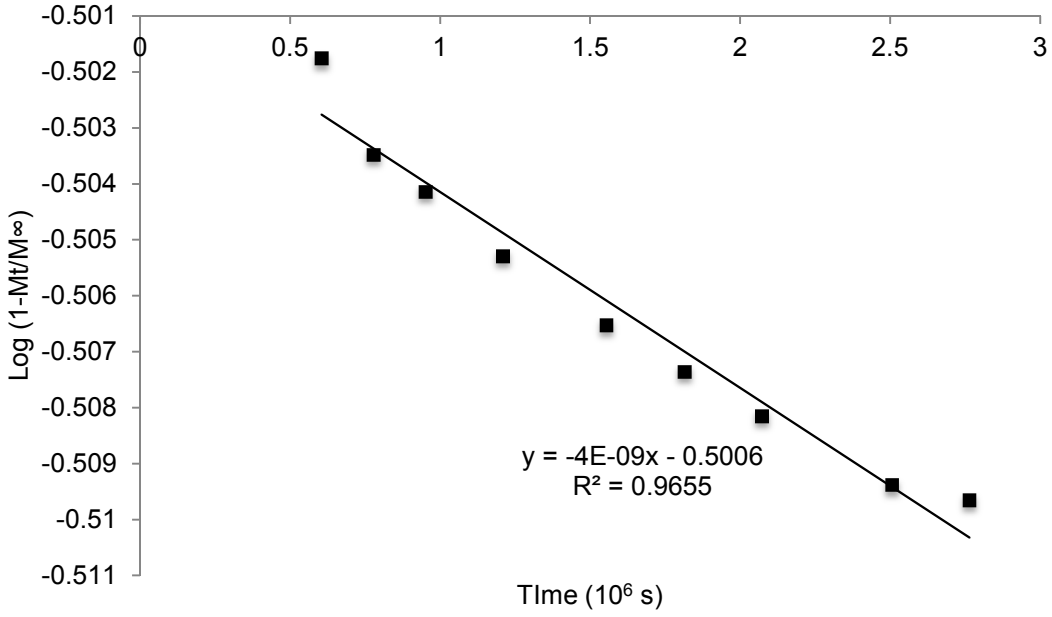

Figure 3.9: Graphs for late-time approximation of effective diffusion coefficient, D_{eff}. A) Plot of M_t/M_∞ vs. time for 3kDa TRITC-dextran encapsulated in PEG4k hydrogel constructs. B) Corresponding plot for log $(1-M_t/M_\infty)$ vs. time. The slope of the graph was used to calculate $D_{eff}= 8.6 \times 10^{-7} cm^2 s^{-1}$

Comparing the data from the FRAP experiments and that of the in vitro release experiments, we found that for each combination of gel type and dextran, we obtained diffusion coefficients that were of the same order of magnitude, confirming the validity of our methods (Table 3.5). For each combination, D_{eff} values were generally slightly higher than that of the diffusion coefficients obtained from FRAP. This small discrepancy was probably due to slight fabrication defects of the hydrogel constructs. However, given that these discrepancies are very small we can conclude that our fabrication technique has little to no effect on the diffusive properties of these gels when they are incorporated into MEMS devices.

Name of gel	Diffusion coefficients (cm^2s^{-1})					
	3kDa dextran		10kDa dextran		20kDa dextran	
	D_{FRAP}	D_{eff}	D_{FRAP}	D_{eff}	D_{FRAP}	D_{eff}
PEG4k	$4.7\pm0.8\times10^{-7}$	8.6×10^{-7}	$1\pm0.1\times10^{-7}$	3.8×10^{-7}	$<10^{-9}$	3.8×10^{-9}
PEG10k	$1.2\pm0.2\times10^{-6}$	3.8×10^{-6}	$5.7\pm0.9\times10^{-7}$	3.8×10^{-7}	$8.7\pm1.1\times10^{-8}$	9.6×10^{-8}
PEG20k	$>10^{-5}$	4.4×10^{-5}	$5.3\pm0.9\times10^{-7}$	1.1×10^{-6}	$2.5\pm0.5\times10^{-7}$	8.7×10^{-7}

Table 3.5: Diffusion coefficients obtained from both FRAP experiments (D_{FRAP}) and in vitro release of dextran from fabricated hydrogel constructs (D_{eff}).

3.3 Conclusion

We are able to tune the mechanical properties and permeability of the hydrogels by varying the molecular weight of the PEGDA chain. It is also observed that stiffer gels tend to be less permeable and this is the combined effect of denser and highly crosslinked networks. As we are able to obtain superior mechanical properties, PEGDA can be expected to be a viable building material for implantable MEMS devices. The ability of it to be impermeable to certain molecules also makes it an ideal material for constructing drug delivery devices, with the added advantage of more permeable PEGDA hydrogels as a means of controlling release kinetics.

Chapter 4

Hydrogel MEMS-Device design, fabrication and testing

Various groups have demonstrated that it is possible to create defined microstructures out of hydrogels such as PEGDA[70-72] with varying degrees of success. Most of these techniques, however, yield microstructures that are single components anchored to a hydrogel or non-hydrogel substrate [73]. Other additive manufacturing methods, including use of hydrogels as well as other non-biocompatible materials, yielded final structures that do not include moving parts[74-76]. In our lab, we have also previously demonstrated fabrication of hydrogel shapes and structures using photolithography methods aided by microfluidics[77]. Though versatile and capable of precisely producing microstructures at high resolutions (~20μm) this strategy was still not suitable for constructing a MEMS-like device.

One of the common problems faced by such techniques of microfabrication of hydrogels is that they did not have flexible control of the thicknesses of the structures constructed; the thicknesses of the components were typically defined by the height of the mold in which the hydrogel was cured [78-80] or by the thickness of spacers that separate two substrates in between which the gels are polymerized. Here, we have a devised a simple method of fabrication with flexible control of the z-axis while maintaining high resolutions in the x-y plane. Additionally, we also show that we can isolate, align and assemble preformed hydrogel structures to form moving components within larger structures, essentially forming a MEMS-like device.

4.1 Device fabrication and design

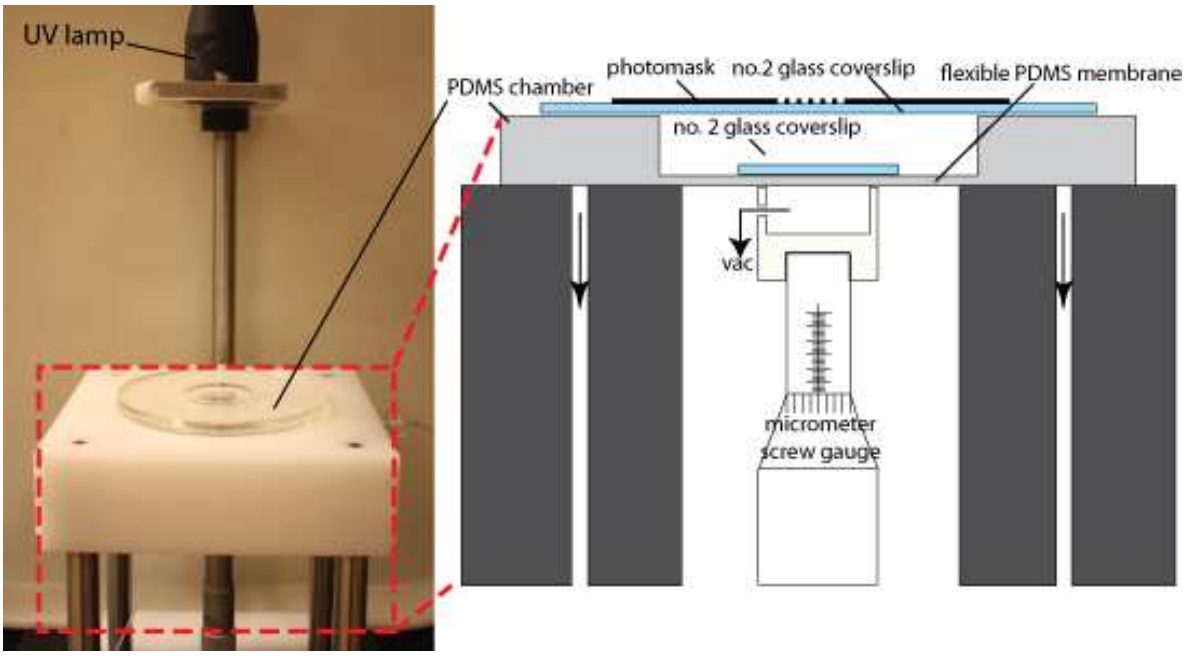

Figure 4.1. Picture of fabrication set-up and corresponding schematic diagram of individual features and components.

We have devised a fabrication technique and set-up that allows for precise z-axis control (Figure 4.1). This set-up consists of a stage with etched and drilled tracks leading to a vacuum line, an integrated micrometer screw gauge, PDMS chamber in which the hydrogels are polymerized, as well as an aligned collimated UV light source. The PDMS chamber has a flexible membrane that is coupled to the micrometer screw gauge via negative pressure generated by the vacuum. This flexible membrane also has a thin piece of glass plasma-bonded to it on which the PEGDA prepolymer can be deposited and cured. This plasma-bonded glass is also silanized to prevent the adhesion of hydrogels on its surface after repeated use. The micrometer screw gauge can easily control the thickness of the layer of cured PEGDA by controlling the height of the flexible membrane and hence its distance relative to the top of the PDMS chamber. During fabrication, the PDMS chamber is covered with a glass coverslip, onto which a photomask can be placed. In this manner, layer-by-layer fabrication of hydrogel

structures is possible. This set-up, along with the use of different types of glass coatings for the glass coverslip, also allows for the easy manipulation of fabricated components and their alignment with respect to each other in the finished product.

4.1.1 Device fabrication

4.1.1.1 Surface treatment of glass coverslip. Different types of surface-treated glass coverslips for the top of the PDMS chamber were used during our fabrication process. Depending on the type of structure being constructed, the hydrogel can be made either to adhere to the glass coverslip following photopolymerization (to immobilize the structure so as to ease manipulation and alignment of the structure during downstream assembly) or to be repelled from the glass coverslip, leaving it on the side of the flexible PDMS membrane. To promote hydrogel adhesion, 35 x 50mm glass coverslips were immersed in 10w/v% TMSM (in 70% ethanol) for an hour. The cover glasses were rinsed three times in 100% ethanol and baked at 120°C for at least 10mins. To prevent hydrogel adhesion, a thin layer of PDMS (<100μm) was spun and cured onto glass coverslips as non-adherent surfaces to the hydrogel (due to the oxygen inhibition layer present on the PDMS surface). The thin glass that is bonded on the flexible PDMS membrane is also treated with trichloro(1H,1H,2H,2H-perfluorooctyl)silane via vapor deposition to prevent the strong adhesion of PEGDA to its surface following long-term use.

4.1.1.2 Mask design for photolithography of PEGDA. Photomasks were used to define the shapes of the polymerized PEGDA hydrogel structures. Each layer of the device and its components were designed on separate photomasks. These photomasks were designed on Adobe Illustrator and printed by CAD/Art Services (Bandon, OR).

4.1.1.3 Layer-by-layer assembly. The schematic of a typical fabrication procedure are shown in Figure 4.2. Prior to fabrication, a cleaned PDMS chamber was placed on top of the

fabrication stage where it was secured onto the stage via vacuum. A 35 x 50mm #2 glass coverslip was placed on top of the PDMS chamber to form a closed chamber. The micrometer was brought upwards until the glass piece (10 x 10 mm) that is attached to the flexible membrane (hereafter known as the bottom substrate) was in complete contact with the top glass coverslip. The corresponding z-position of the micrometer screw gauge was then used as a reference zero point. This step was done whenever a new PDMS chamber was used to account for any thickness variations. At this point, the bottom substrate was lowered and the hydrogel prepolymer was deposited onto it. Then, the bottom substrate was lowered until it reached the desired height. A mask was placed directly on top of the top cover glass and the hydrogel was exposed using a collimated UV light source (Omnicure S2000, EXFO) for 10-20s (Figure 4.2, step 1). The top cover glass was then removed and any uncured prepolymer was removed by vacuum suction. A new hydrogel prepolymer (of either the same or different composition from the first) could then be deposited for the subsequent cycle. The bottom substrate was adjusted to a new z-position. A new mask was aligned with respect to the hydrogel microstructures formed in the previous cycle and another photopolymerization step was performed (Figure 4.2, step 2). After the supporting structures were formed (which remained attached to the bottom substrate), the top cover glass was removed to allow the transfer of free-standing, prefabricated components (e.g. microgear, different layers of hydrogel) onto the supporting structures (Figure 4.2, step 4). Once the free-standing component was successfully transferred onto the supporting structures, the PDMS chamber was topped by a new cover glass on which a piece of preformed hydrogel was adhered to (Figure 4.2, step 5). An external magnet could be used to guide any free-standing, iron-doped components to the desired position. Finally, a new mask was used to photopolymerize selected regions on the hydrogel device to seal the top hydrogel piece to the underlying supporting features (Figure 4.2, step 5).

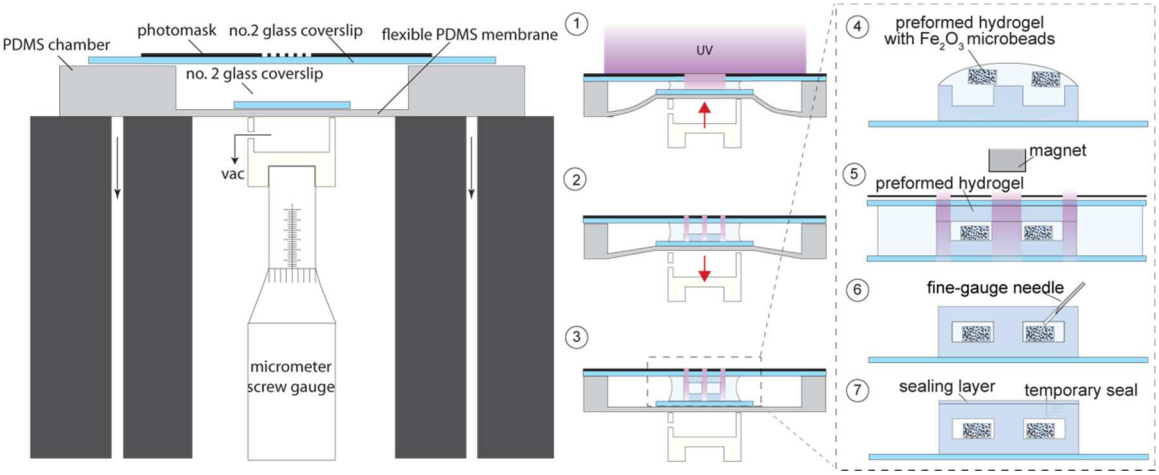

Figure 4.2: Fabrication set-up and schematic of fabrication technique. The middle panel describes the use of the micrometer screw gauge to allow for precise z-control and hence enables us to use a layer-by-layer fabrication technique. The right most panel describes how individual components can also be manipulated and aligned against supporting structures. Following a final polymerization step to seal the entire construct, forming a complete device, uncrosslinked prepolymer solutions present in voids of the device can either be allowed to diffuse out or draw out using fine-gauge needles. A final sealing layer has to be applied should a fine-gauge needle be used to remove uncrosslinked materials.

4.1.1.4 Iron-doped components.

Our devices are incorporated with components that can be actuated magnetically. These components are doped with superparamagnetic particles and can be done in one of two ways:

Bulk doping. ProMag™ Superparamagnetic Microspheres suspensions were first centrifuged to isolate the microspheres from the solution in which they are suspended. The microspheres are then mixed with prepolymer and vigorously vortexed to ensure a uniform suspension. This doped prepolymer was then polymerized using the technique described above to create structures containing superparamagnetic particles which respond to magnetic actuation

Depot doping. Superparamagnetic iron oxide nanopowder (Sigma-Aldrich, St. Louis, MO) was first weighed out. The moving component was then fabricated such that a well/reservoir is

formed as part of the structure of the component. The dry powder is then suspended in a small amount (~20μL) of prepolymer to form a paste and then pipeted into the well. A small permanent magnet is used to aid the placement of the nanopowder within the well. As the nanopowder is attracted to the base of the well, excess prepolymer is removed using a micropipette. The structure is then exposed to UV to temporarily fix the nanopowder in place to prevent their dispersion when the magnet is removed. After the magnet is removed, more prepolymer is then placed on top of the well and the height of the bottom substrate is adjusted. The nanoparticles are then sealed in and the moving component is formed at the desired height.

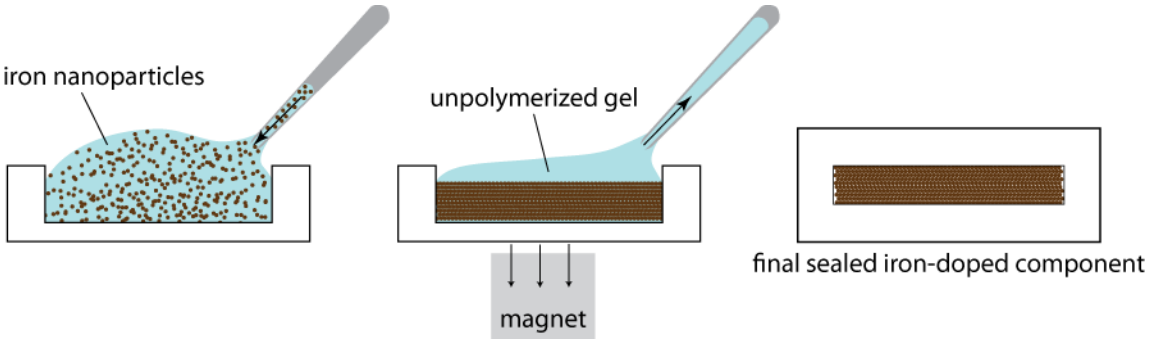

Figure 4.3: Depot doping method for the microfabrication of iron-nanoparticle doped components. A suspension of nanopowder in prepolymer is deposited into a pre-formed well. Using a magnet, the nanoparticles are aligned in the well and the component is subsequenty sealed with more prepolymer, setting the nanoparticles in place.

4.1.2 Device design.

As an initial demonstration of hydrogel-based MEMS device, we proposed to design devices for implantable drug delivery applications. Common features of the design include:

i) A moving component consisting of iron-doped hydrogel that is fabricated using either the bulk- or depot-doping methods.

ii) Reservoirs for drugs/payload which separate each individual “dose” from each other.

iii) Diffusion window/aperture out of which the drug to exits the device.

iv) A locking mechanism to prevent accidental movement and hence release of drugs. Typically, structures fabricated out of “softer” hydrogels (less stiff with lower Young’s modulus) were used as supports that hold the components in place when magnetic actuation is absent. PEG20k and PEG10k gels are used for this purpose.

Variations of each of the following designs ideas were fabricated and tested.

4.1.2.1 Linear chambers.

In this design, the iron-doped hydrogel was first fabricated using the bulk doping method and PEG4k gels. Hydrogels were also doped with fluorescent- labeled dextran (payload or “model drug”) by mixing solutions of FITC- or TRITC-dextran (155kDa) with PEG20k prepolymer (most permeable) and photopolymerized to yield PEGDA hydrogel pieces that are doped with fluorescent-labeled dextran. The amount of dextran in each doped hydrogel piece is at the order of that used in drug-dosing regimens. The pre-fabricated iron-doped and dextran-doped hydrogel pieces were then set aside while the surrounding supporting structures were fabricated. The top layer of the device consists of a hydrogel layer (PEG4k) that is impermeable to the dextran with a permeable window (PEG20k) out of which the dextran can diffuse. The middle layer (PEG10k) of the device consists of reservoirs to contain the dextran-doped pieces and a channel that is complementary in shape to the iron-doped plug. The complementary shape of the channel allows for the iron-doped plug to be “locked” in place when it is not actuated. The material of the channel that would immediately surround the iron-doped hydrogel plug is selected to have a significantly lower mechanical stiffness compared to that of the iron plug. This stiffness mismatch is important as it allows for the movement of the iron-doped plug when it is exposed to a magnetic field; as the iron-doped plug is actuated to move, it is able to deform the hydrogel surrounding it and slide along the channel. As the iron-doped plug moves to the right (Figure 4.4), it exposes a pathway out of which the dextran can diffuse. The

combination of the complementary shape of the channel and the stiffness mismatch is crucial to ensure a single “dose” is delivered per actuation and prevent the accidental release of multiple doses.

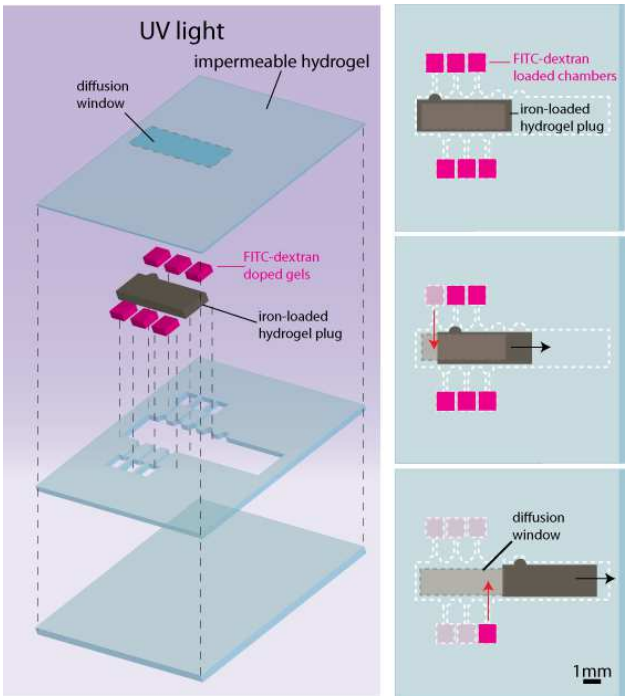

Figure 4.4. Drug delivery device with multiple drug-containing chambers or reservoirs arranged in a linear fashion. The various layers and components of the device (left) prior to the sealing of the device is shown. The linear movement of the iron-doped hydrogel plug controls the diffusion of the TRITC-dextran. In the “closed” position (right, top), the diffusion window is blocked off by the iron-doped plug. When the iron-doped plug (bulk doping method) is actuated to move to the right, a pathway for diffusion is exposed to the first chamber (right, middle). The bottom most diagram shows the position of the iron-doped plug when the last “dose” of dextran is released.

4.1.2.2 Rotating devices.

In this design, the moving component is incorporated with reservoirs to contain the drugs which is loaded into the device in solution. As shown in Figure 4.5, the top layer (i) of the device has an aperture out of which the drug diffuses. The moving component (ii) resembles a single rotating gear with a depot containing iron nanopowder (depot doping method). The gear has a star-shaped bore that has a complementary fit to the star-shaped axle on the bottom later of the device (iii). The star-shaped axle is made of a hydrogel that is less stiff than the rotating gear. This stiffness mismatch and the shape of the axle aids the precise movement actuation of the device; the rotating gear can be actuated to move by a single position, exposing the drug to the aperture one reservoir at a time. As shown in Figure 4.5 (right panel), when the device is in the

closed (non-dosing) position, the iron depot is aligned to the aperture in the top layer. As it is actuated to move clock-wise, the first reservoir is then aligned with the aperture and the first dose is released. The star-shaped axle prevents further movement and in this manner, doses can be released from the device a single-dose at a time. The star-shaped axle is typically fabricated using PEG20k gels while the rest of the device is constructed out of PEG400 gels.

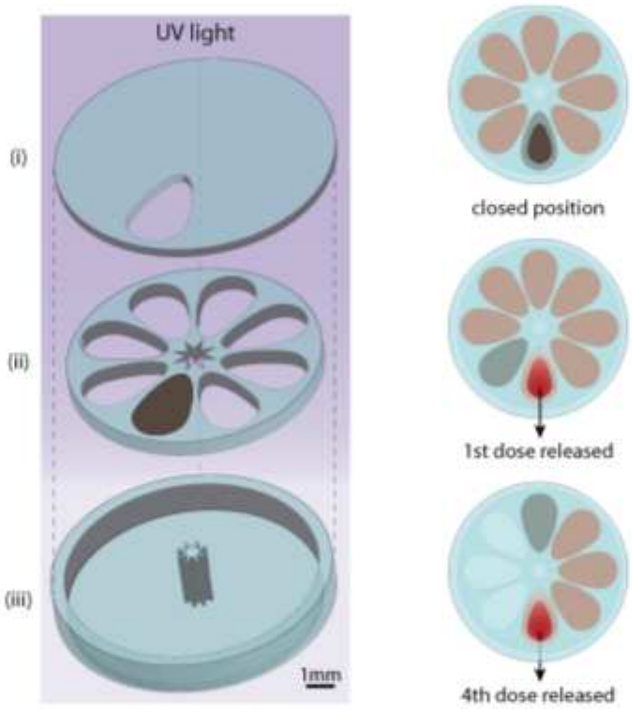

Figure 4.5. Rotating hydrogel MEMS device for drug delivery. This device contains a rotating disc (ii) in which the drugs are loaded. One of the chambers in the rotating disk is depot-doped with iron nanoparticles. The diffusion window is an aperture on the top layer of hydrogel out of which the drug can diffuse (i). The base layer (iii) contains a star-shaped axel made of softer PEGDA materials and is complementary in shape to the central bore in the rotating disc. The panel on the right shows different stages of dose-release upon actuation.

4.1.2.3 Two-gear device.

In this design (Figure 4.6), the method in which the drugs are release is similar to that of the rotating device (see above). The larger gear contains reservoirs for drugs and when each reservoir is aligned to the aperture, the drug then diffuses out of the device. The larger gear also has a star-shaped bore and corresponding axle.

However, the iron depot is now located on a smaller, driving gear. This design incorporates an intermittent mechanism in which a device is regularly advanced and then held in place for a brief duration of time. The two gears are designed such that they are engaged to each other and the

larger gear only rotates by 45° with each full rotation of the driving gear and otherwise stays in place when not engaged.

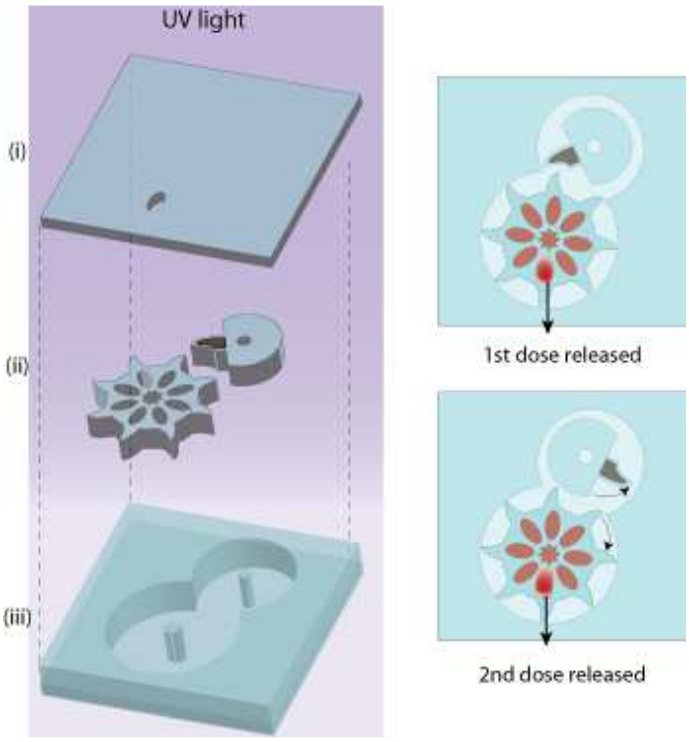

Figure 4.6: Two-gear hydrogel MEMS device for drug delivery. This design consists of 2 gears (ii); a larger gear containing reservoirs for drugs and a second smaller driving gear that contains an iron depot. When the driving gear is actuated to move by one full rotation, it engages the larger gear and causes it to move by one position (45°); exposing a single reservoir to the aperture on the top layer. Each full rotation of the driving gear corresponds to the release of a single dose.

4.1.2.4 Geneva drive device.

An interesting variation of the two-gear device is a design based on the Geneva drive (Figure 4.7). Also based on an intermittent mechanism, the two gears are overlapping one another with a pin located on the driving gear (Figure 4.7). This design would not only be more robust (no slippage during engagement of the driven gear and hence advancement of the driven gear is ensured), but also decreases the surface area of the device.

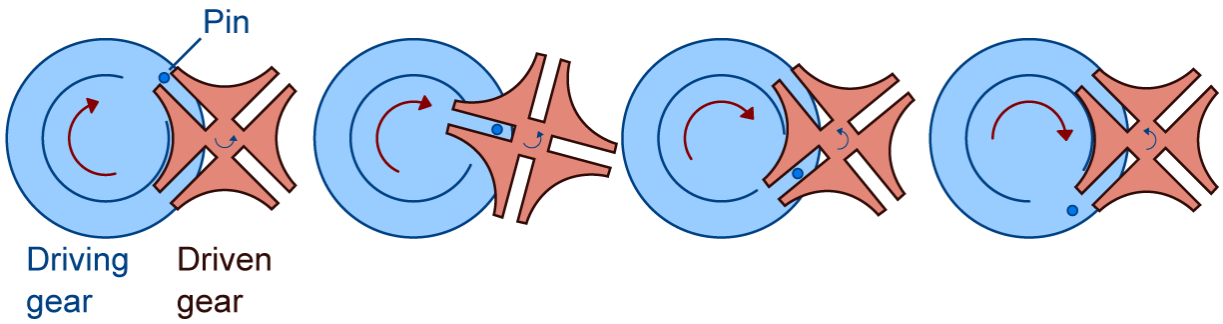

Figure 4.7: Operation of Geneva drive. A driving gear with a pin engages with the slot on a driven gear and advances the driven gear by "one step" of 90º for each full rotation of the driving gear. This diagram is adapted from [81].

As can be seen in Figure 4.7, the degree of advancement of the driven gear depends on the number of slots it has for engagement with the pin. In general, if the driven gear has *n* slots, it advances by 360º/*n* for each full rotation of the driving gear. Figure 4.8 shows a schematic of a typical Geneva drive that was fabricated using our technique. The posts, which hold the driven gear in place when the device is not being actuated, are typically fabricated out of softer hydrogels such as PEG10k while the rest of the components of the device, are constructed out of PEG400 gels.

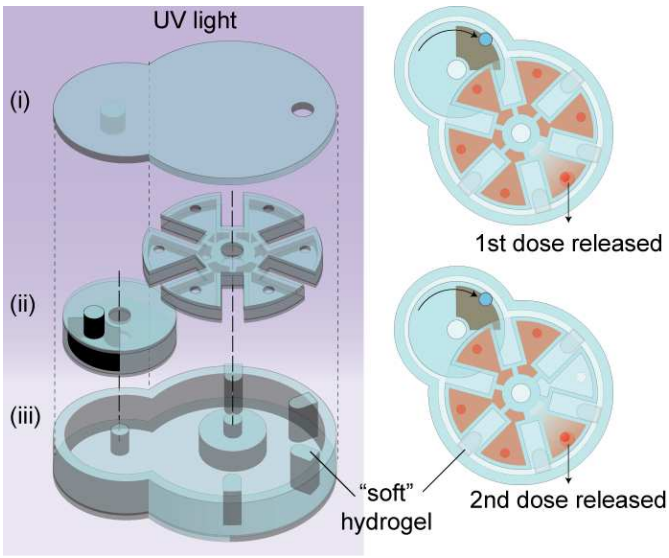

Figure 4.8: Geneva drive hydrogel MEMS device for drug delivery. This schematic shows a variation of the two-gear design. It consists of two stacked gears (ii). The driving gear has a pin that engages a driven gear that contains reservoirs that can be filled with drugs/payloads. The top layer (i) has an aperture out of which the drugs can diffuse to the surrounding environment. The base (iii) of the device contains axles, supporting structures as well as posts that are made of PEG10k gels that are designed to hold the driven gear in place when not engaged.

4.1.2.5 Magnetic actuation.

All devices are actuated with strong permanent magnets (N52 neodymium magnets, K&J Magnetics, Inc). The magnets are typically held under the device, directly below the moving component, at a distance of 0.5-1cm. For precise rotational actuation, an actuator consisting of a slow-spinning motor and gears with a neodymium magnet attached to one of the gears was used (Figure 4.9). The voltage supplied to the motor was changed in order to vary the rotational speed of the magnet.

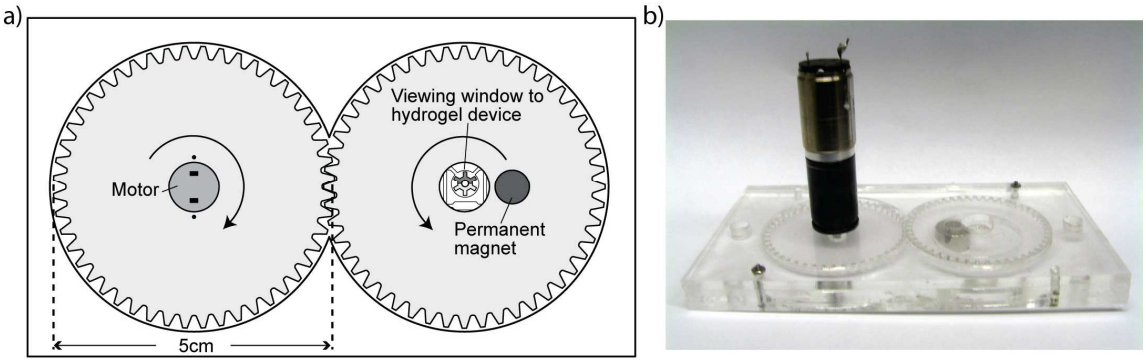

Figure 4.9: Schematic and image of actuator used for rotational actuation of devices. A slow spinning motor is attached to one of the gears. Movement induced by the motor will cause the two engaged gears to rotate. This movement generates the uniform rotational movement of a permanent magnet located on the driven gear. Changing the voltage supplied to the motor in turns control the rotation of the magnet; a higher voltage results in higher revolutions per minute of the magnet.

4.1.3 Results and discussions.

We were able to precisely fabricate microstructures using our fabrication strategy; a resolution of 100μm in the xy-plane and 25μm in the z-axis can be achieved. This strategy also allowed us to easily fabricate complex structures with one or more moving components. Figure 4.10 shows examples of simple devices that can be built using this strategy; spinning gears that respond to magnetic actuation. Other features such as fluorescent references can also be added to aid in imaging the device after it has been implanted (Chapter 5). The following sections discuss the

various designs that were fabricated and tested towards developing an implantable drug delivery device.

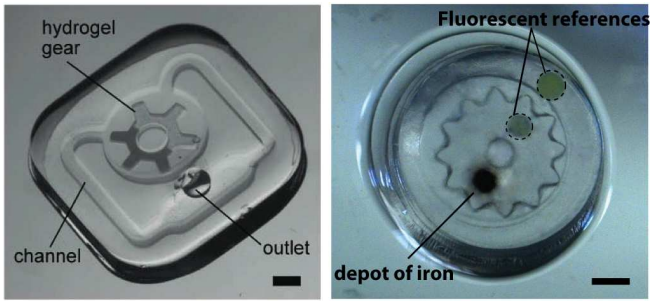

Figure 4.10. Simple hydrogel MEMS devices. The image on the left shows a hydrogel gear with half of the gear doped using the bulk doping method. The gear on the left was made using the depot doping method and includes fluorescent beads embedded in the gear and the capsule of the gear. Scale bars are 1mm.

4.1.3.1 Design of drug delivery device.

There were several lessons learned as we proceeded with the fabrication of a hydrogel MEMS device that could be used as an implantable drug delivery device:

1) *Introduction of iron particles into hydrogel components.* In order to produce robust movements and actuation, moving components that were doped using the depot doping method performed better as they responded more strongly to magnetic actuation. This is because there is a limit to which the microparticles can be incorporated in the moving component using the bulk doping method; the microparticles tended to absorb the UV light during photopolymerization as they were opaque. If too many particles were suspended in the prepolymer they would prevent hydrogel polymerization. Whereas when the depot doping method was used, the amount of nanopowder that can be densely packed into the moving component was only limited by the size of the depot.

2) *Loading of payload into hydrogel MEMS device.* Drugs/payloads have to be injected/loaded in their liquid form into the hydrogel MEMS device. Photopolymerization of dextran dissolved in prepolymer caused the dextran to be immobilized within the hydrogel network. This prevents it from diffusing out of the dextran-doped hydrogel pieces, resulting in the hydrogel retaining a

large amount of the dextran that was introduced. This is probably because there is poor interconnectivity in the porous structure of the hydrogel. Also, some molecules may have poor solubility in the prepolymer solution and this might affect the concentration of drug that is loaded into the device.

3) *Linear vs. rotational movement of device components.* In the interest of minimizing the size of the device, designs that were actuated using rotational movements were favored over designs that required actuation of linear movements (Figure 4.11, 4.12, Video 4.1). This is because for devices in which the moving component moves linearly, we have to take into account the space into which the component can move when it releases the drug (dead space). This often increases the surface area of the device by as much as twice that of the surface area required for the drug-filled reservoirs. For rotating designs, the moving component traverses a cyclic path and typically moves together with the reservoirs. Hence, less dead space is introduced with such designs.

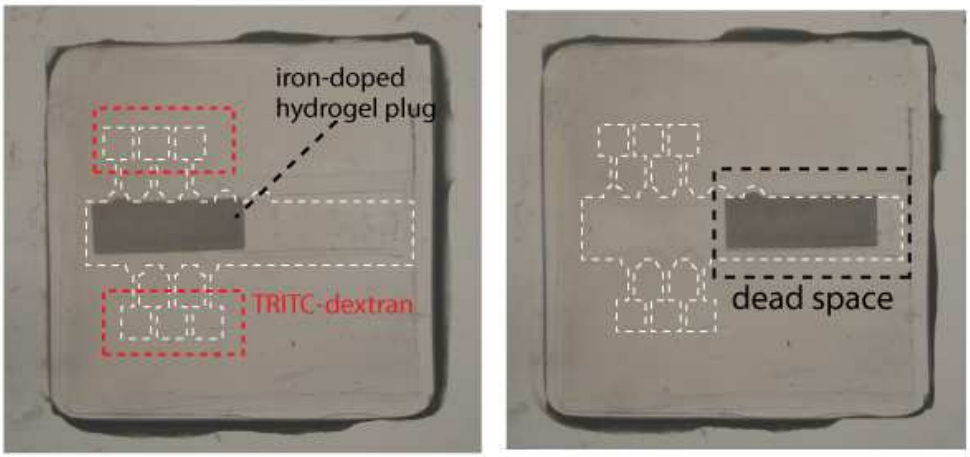

Figure 4.11: Fabricated linear chamber design. The device consists of 6 drug-filled chambers and an iron-doped hydrogel plug. As the iron-doped plug moves to the right to release the doses contained in the device, it recedes into the dead-space located at the end of the channel. White dashlines elucidate the shape of the reservoirs and channels.

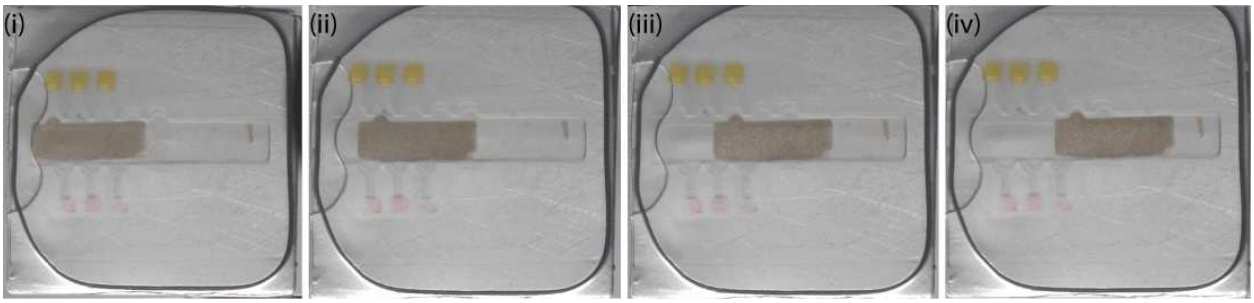

Figure 4.12: Time-lapse images of a linear hydrogel MEMS device with fluorescent-labeled dextran as payloads. Were able to fabricate and actuate a 6-chamber device containing TRITC-dextran (3 doses) and FITC-dextran (3 doses). The images show the position of the iron-doped plug when the device is "off" (i), actuated to release one dose (ii), three doses (iii) and five doses. Although we were able to actuate this device, it was found that the iron-doped plug responded weakly to the magnetic actuation and would sometimes fail (in this case, a 6th dose was not delivered). Also, dextran solutions immobilized in PEGDA gels did not diffuse to the main channel. Linear devices such as these also tended to have larger surface areas due to the dead space required for the movement of the iron-doped plug.

4) *Precision of actuation.* In designing and fabricating devices that were actuated by rotational movement of a permanent magnet, it was found that the two-gear designs could be actuated more easily and accurately. This is because it was difficult to achieve precise, small angular movements in the single rotating gear design as compared to a full rotation in the 2-gear design. Also, for in vivo applications, it would be difficult to locate and keep track iron depot in between actuations for the single gear device; imaging techniques would have to be used to aid actuation. However, for the 2-gear design, the location of the iron depot will be the same at the start and end of actuation as it moves one full rotation. In this way we are able to "reset" the position of the iron depot with every actuation and there is a larger room for error should the device move slightly within the animal. The operation of this device is shown in Figure 4.13 and Video 4.2

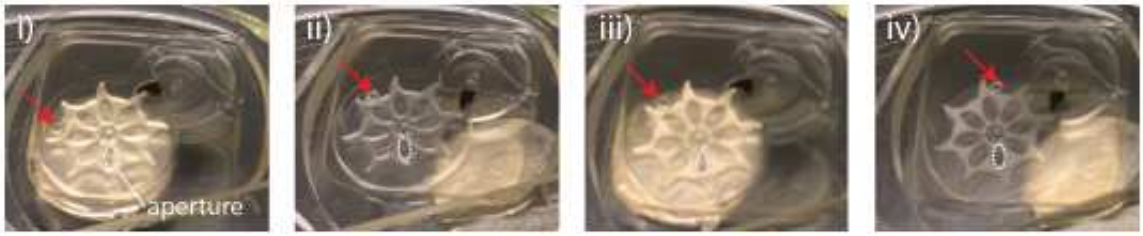

Figure 4.13: Actuation of two-gear hydrogel MEMS device. These images show the positions of the two gears relative to each other as well as the aperture on the top layer of the hydrogel device during rotational actuation. The dashed ellipse indicates the position of the aperture and a red arrow indicates the position of an air bubble trapped between two spokes as a position reference of the driven gear. The first image of the series shows the driving gear in its starting position and there is no movement in the driven gear (i). When the driving gear is actuated, the driven gear moves by 1 position (45^{O}) and the next drug reservoir is now positioned under the aperture (ii). The driving gear is fully rotated and ends back in the starting position (iii). The driving gear can then be actuated again and the driven gear moves another 45^{o} (iv).

Another successful design that was developed and tested was the Geneva drive device. It is similar to the 2-gear device described in Figure 4.13 but the two gears overlap each other and it was found that the pin-slot method of engagement between the two gears was more robust; for the device shown in Figure 4.13, the two gears would sometimes fail to engage due to slipping between the two gears. Figure 4.14 shows the dimensions of the device and its individual components while Figure 4.15 shows the fabrication steps and final assembly of the Geneva drive device.

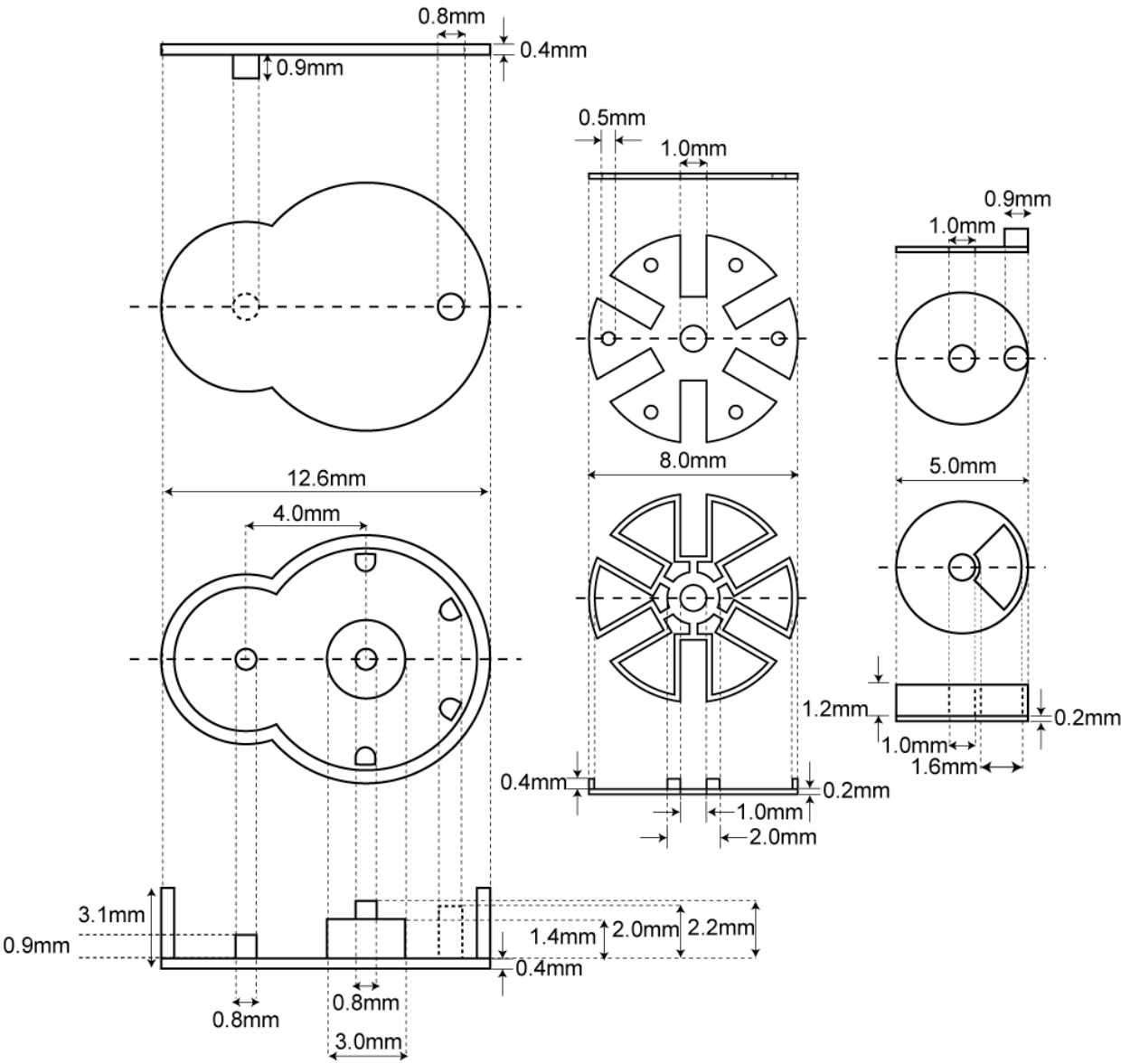

Figure 4.14: Schematic of Geneva drive device showing the dimensions of the various components in the device. The bulk of this device was constructed in PEG400. The left panel shows the top and cross-section view of the supporting structures, including 2.0mm tall PEG10k posts. The middle panel shows the top and cross-section view of the driven gear. The top of each drug reservoir is designed to have a 0.5mm aperture that aligns with a 0.8mm aperture on the top layer of device during device operation. The driving gear (right panel) has a pin that measures 0.9mm in diameter. This pin engages with 1mm wide slots on the driven gear during device operation.

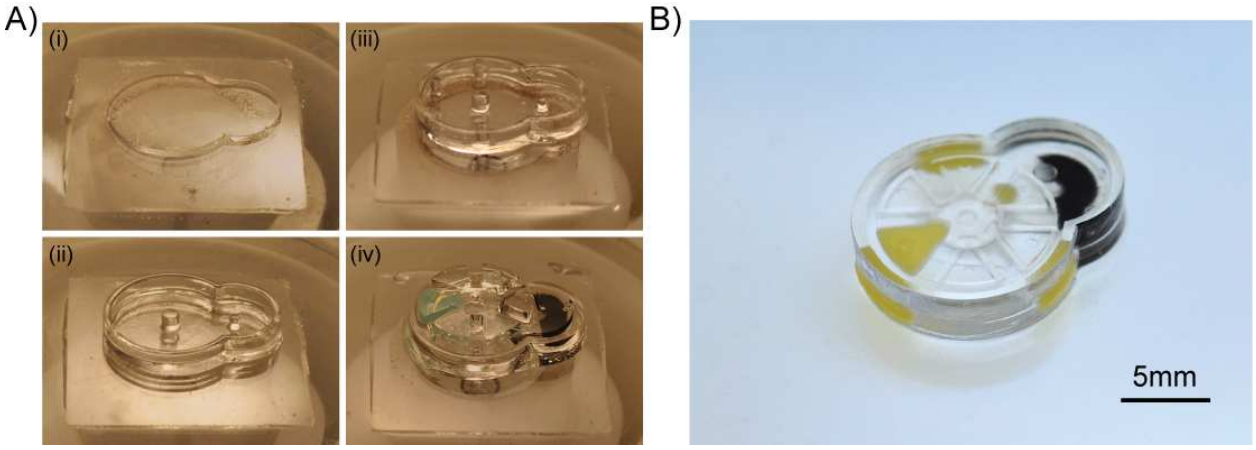

Figure 4.15: Fabrication and complete assembly of a Geneva drive hydrogel MEMS device. A) Images of layer-by-layer assembly of the Geneva drive device. A base layer was first polymerized (i) followed by the axles for both gears and supporting structures (each layer is of a different height) (ii). All the layers in (i) and (ii) were constructed out of PEG400 gels. After removal of prepolymer, a different prepolymer (PEG10k) was then introduced and posts which were designed to hold the driven gear in place in the absence of actuation were formed (iii). These posts were located on the outer edge of the driven gear and fit into 4 of the slots. After all the supporting structures were constructed, the moving components (gears) were then added to the structure. A small magnet was used to align the gears. After alignment, the stage is set to the final height of the device and the entire construct is sealed with a top layer of pre-formed hydrogel. B) Image of the complete hydrogel MEMS Geneva drive device.

These devices were then actuated *in vitro* to ensure that they can function as designed. Using actuator shown in Figure 4.9, with the magnet placed at ~1cm away from the device, we were able to robustly actuate the device (Figure 4.16 and Video 4.3).

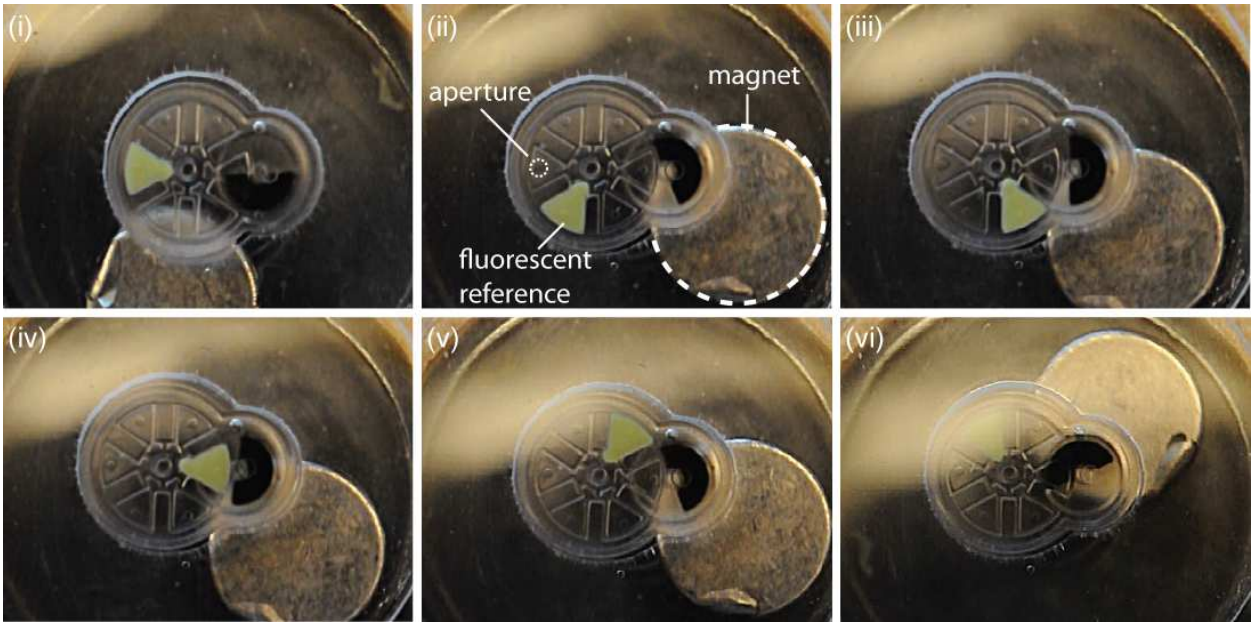

Figure 4.16: Still-frames of a video showing the operation of the Geneva drive device. One of the chambers in the driven gear is filled with fluorescent beads to aid in imaging after *in vivo* implantation. This chamber is placed under the aperture before actuation in an "off" position (i). After a full rotation (clockwise) of the driving gear, the driven gear rotates (anti-clockwise) and the next reservoir is then positioned under the aperture (ii). This is repeated until the driven gear has made a full rotation.

4.1.3.2 Locking mechanism.

A movie was taken of the star-shape bore and axle in the device during actuation. The still frames from the movie (Figure 4.17 and Video 4.4) show the star-shaped bore at the center of the driven gear and the star-shaped axle that is positioned in the bore. The edge of the bore of the gear appears darker, while the edge of the axle is elucidated by dashed lines (i). When the device is not actuated (ii), the star-shaped axle is able to maintain its shape and hold the gear in place. Upon actuation, the star-shaped axle can be seen to deform as the edges of the gear move against it (iii). This deformation/yielding allows for the movement of the driven gear when enough magnetic force is applied. When the gear has moved to its next position and magnetic actuation is stopped, the star-shaped axle reverts back to its original shape.

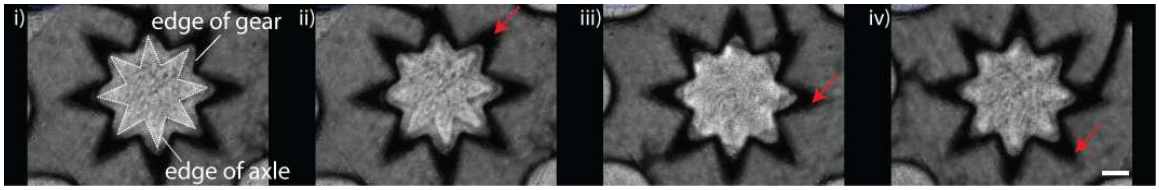

Figure 4.17: Still frames of a movie (Video 4.4) showing the deformation of the star-shaped axle during gear actuation and movement. The star-axle deforms when the stiffer gear moves against it but reverts back to its original shape when there is no actuation.

In the specific case of the Geneva drive device, we have PEG10k posts which hold the driven gear in place during the absence of magnetic actuation. During actuation, these posts will have to deform and bend to allow for the movement of the driven gear. We can estimate the force needed to bend the posts via simple beam-bending equations

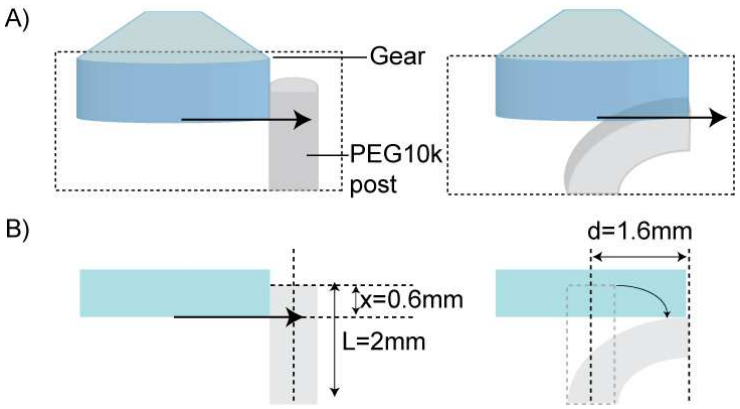

Figure 4.18: Diagram of theoretical post-bending during magnetic actuation. A) When the driven gear rotates, it exerts force at a point along the length of the of the PEG10k post. This causes the post to bend to allow for the passage of the gear. B) Cross-sectional view of post and gear unit with the relevant dimensions.

If we assume that there is no deformation in the gear during actuation (gears are typically composed of PEG400 gels that are 3 orders of magnitude stiffer than PEG10k gels) and that there is a pure bending effect on the PEG10k gels, we can use the equations for point-loading of a fixed cantilever beam:

$$d = \frac{Fx^2}{6EI}(3L - x)$$

where d is the maximum deflection of the beam, F is the force applied on the beam, x is the distance from the free end of the beam where the force is applied, L is the length of the beam, E is the Young's modulus for the beam and I is the area moment of inertia for the beam. Therefore, we can use this equation to calculate the force needed for the gear to deflect the beam. If we assume that this deflection corresponds to when half (or more) of the width of the "spoke" of the driven gear (reservoir chamber) has crossed the vertical mid-axis of the PEG10k post, we can then calculate the minimum amount of force needed to bend the PEG10k post to allow for safe passage of the driven gear.

$$F = \frac{d6EI}{x^2(3L - x)}$$

where $\mathrm{I} = 1.005\mathrm{x}10^{-14}m^4$ for PEG10k posts with a semicircle cross-sectional area with a radius of 0.4mm, E= 19.8kPa for PEG10k gels, d= 1.6mm (maximum width of each reservoir in the driven gear is 3.2mm), $x = 0.6mm$. Thus, this minimum force was calculated to be 0.00098N per post, or 0.0039N for a total of 4 posts in the Geneva drive design.

(Note: estimated maximum weight of driven gear is $3.1\mathrm{x}10^{-6}$kg and would not be enough to deform the posts on its own).

If we assume a frictionless device (lossless transfer of power between the driving and driven gears), we can assume that the magnetic force applied on the driving gear has to be at least 0.0039N in order for actuation to be successful. COMSOL magnetic field simulations were performed to confirm this.

A)

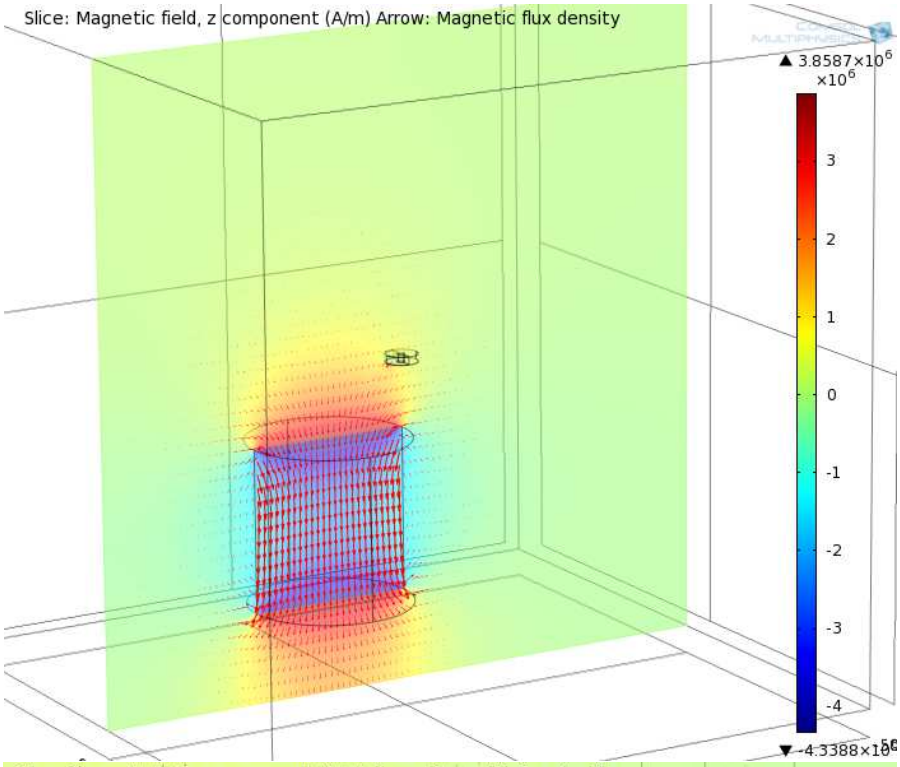

B)

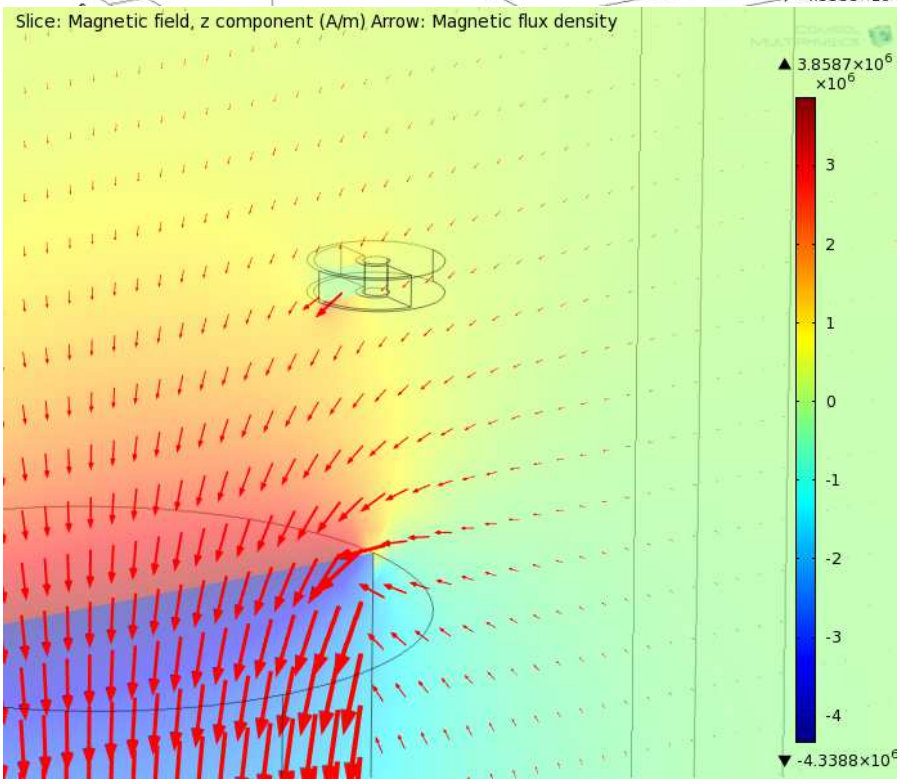

Figure 4:19: COMSOL magnetic field simulation of the magnetic force acting on the driving gear. A) The geometries and material properties of neodymium magnets (N52), and driving gear with iron oxide depot were use to set-up the simulation. B) Close-up view of arrow volume showing the magnetic force vectors acting on the driving gear.

Using known values of relative magnetic permeability of iron-oxide nanoparticles and the magnetization curves of neodymium magnets (as provided by manufacturer, K&J magnetics), we can simulate the magnetic field in the system and calculate the magnetic force acting on the driven gear. The corresponding magnetic force in the direction of rotation is 1.8864N. This is much more that what is required to deform the posts. Devices with half the amount of iron nanoparticles were also modeled and fabricated for testing in vivo. A corresponding magnetic force of 0.73N was calculated using COMSOL for these devices. This value is 3 orders of magnitude higher than that is needed to deform the posts. However, these devices were not as robust when they were tested in vitro. This indicates that the losses in power transmission between the two gears as well as friction within the device resulted in a much lower force being exerted on the PEG10k posts by the driven gear during actuation. These losses are difficult to quantify and change depending on the design. Therefore, in order to produce devices that can be robustly actuated, the combination of iron doping of the driving gear and the type of posts for holding the driven gear in place have to be determined empirically.

4.2 Conclusion

In this chapter, we have shown that we are able to make sophisticated MEMS-like devices that are constructed entirely of PEGDA hydrogels. These devices were designed, fabricated and tested with drug delivery applications in mind. We also made use of the range of different permeabilities and stiffnesses of the hydrogels to our advantage. We also developed strategies that were unique in the fabrication of PEGDA-based components with features in the micron-scale that can respond to magnetic actuation. The assembly of these components resulted in whole devices that can be actuated robustly and wirelessly via a permanent magnet.

Before moving on with implementing these devices for delivery of payloads, we also determined several design features or considerations that were important in addressing certain criteria depending on intended application for the hydrogel MEMS device.

Device criteria	Design considerations
Small foot print or surface area due to *in vivo* spatial limitations	• Moving component should produce rotation movements when actuated • Reservoirs for payloads move in synchrony with moving component, not in a fixed location within the devices, minimizing dead space in device.
Strong response to actuation (eg: deeper implantations)	• Depot-doping methods with nanopowder in order to have higher levels of iron oxide nanoparticles within the moving component
Precise actuation (eg: in vivo imaging techniques not available)	• Device designs that are similar to Geneva drive design • Designs with assymetrical designs
Long-functioning device	• Simple single-gear devices without engaging gears that would not be disrupted by cell infiltration • Decrease friction between moving layers (supports and gears)
Fast, efficient release of payload	• Reservoirs that allow for introduction of payloads in solution-form

Table 4.1: Device criteria and corresponding design considerations to address these criteria.

As summarized in Table 4.1, certain design considerations or decisions can be made when designing devices to meet criteria that one might have for an implantable device depending on its intended application. For applications where a device with minimal size or foot print is required due to spatial limitations at the intended site of implantation, device designs that employ rotational actuation and movements should be favored. The reservoirs in which payloads are contained should also be designed to move in synchrony with the moving component (as described for the rotating gear designs). Having a combination of linear movements as well as reservoirs that are fixed in location within the device introduces deadspace into the device. Should a strong response to magnetic actuation be required, for example for applications where the device has to be implanted deep into the body, depot-doping

methods for introducing iron oxide nanoparticles into the moving component should be favored as these methods allow for a higher concentration of nanoparticles to be introduced. Also, in cases where in vivo imaging of the device is not possible, and precise actuation of the device is still required, designs that are similar to the Geneva drive design should be favored. Also, an asymmetrical device (external shape) would be helpful in helping the doctor or patient pinpoint where actuation should be performed. For example, the Geneva gear has a distinct, assymetrical shape due to the difference in sizes of the two gears. This shape is evident externally even after subcutaneous implantation and the doctor or patient would be able to correctly actuate the device at side where the driven gear is located. For devices that are expected function *in vivo* for longer periods of time, simpler designs such as a single rotating gear should be favored. Over time, cell infiltration into the device (discussed in the following chapter) could result in failure of gears to engage with one another. Steps to decrease friction between the moving layers should also be taken, such as minimizing the surface area of contact between the gears and their supports. Lastly, for fast and efficient release of payloads, designs that allow for the introduction of payloads in their solution form should be employed. This is because payloads that are polymerized in situ with the hydrogel take a much longer time to diffuse out of the bulk of the gel. All these design considerations are important when designing the optimal device for *in vivo* applications.

Chapter 5

Implantable hydrogel-based MEMS device

Current implantable medical devices range from stents, catheters, pacemakers, cochlear implants and drug delivery devices. These devices have been shown to improve the quality of life of patients as upon implantation, the devices serve their purpose often without requiring the intervention of the patient. More specifically, implantable drug delivery devices such as intrauterine devices [82] and insulin pumps[83] have been favored as they improve patient compliance, are able to deliver their payload in a more timely manner[84] and can potentially alleviate the discomfort of patients if delivering drugs that are normally administered via injections or intravenously.

There have been numerous efforts to create implantable MEMS-based drug delivery devices (this is in contrast with implantable slow-release devices from which the drug slowly diffuses into the bloodstream and post-implantation intervention is not possible short or removal of device)[15, 85-87]. However most of these devices are still based on silicon technology, require the use of non-biocompatible and non-biodegradable materials and a power source. As such, these devices would also have to be removed from the body after they have served their function thus requiring a second surgery to excise the device.

Therefore, we propose to demonstrate the use of an implantable hydrogel-based MEMS device towards drug delivery applications. Our proposed solution will not only be fully biocompatible but also does not require an on-board power source and can be actuated wirelessly. This device will be able to precisely deliver a single fixed volume (ie: dose) of its payload per actuation and the dosing regimen can be easily changed depending on whether the device is actuated or not.

5.1 *In vitro* delivery of payload from PEGDA-based MEMS devices

In order to ensure our devices are able to function as drug delivery devices in an *in vivo* environment, we have to first determine if they are capable of delivering payloads in *in vitro* environments. Two different devices were tested in these *in vitro* release experiments; a single gear device and a Geneva drive device.

5.1.1 In vitro release of doxorubicin from a single gear device

Single gear devices with 5 reservoirs (and hence "doses") were designed to deliver payloads of doxorubicin. Doxorubicin was used as a payload to explore the potential use of this device as a means for local delivery of low doses of chemotherapeutics to tumors (Chapter 6).

5.1.1.1 Materials

All materials used for the fabrication of hydrogel MEMS devices were purchased as described. Doxorubicin hydrochloride (Tocris) was purchased from Fisher Scientific (Pittsburgh, PA).

5.1.1.2 Methods

A single gear device was fabricated using the technique described in Chapters 3 and 4. Figure 5.1 shows the dimensions of each component in the device and a schematic of the assembled device. The gear contains 6 reservoirs; one filled with iron nanoparticles and the other 5 for doxorubicin. The device was constructed entirely of PEG400 gels except for 6 posts located at the edge of the gear which were constructed out of PEG10k gels. These posts serve to hold the gear in place in the absence of magnetic actuation. During actuation, the gear rotates to deform the PEG10k posts, allowing it to move to the next position for the release of doxorubicin.

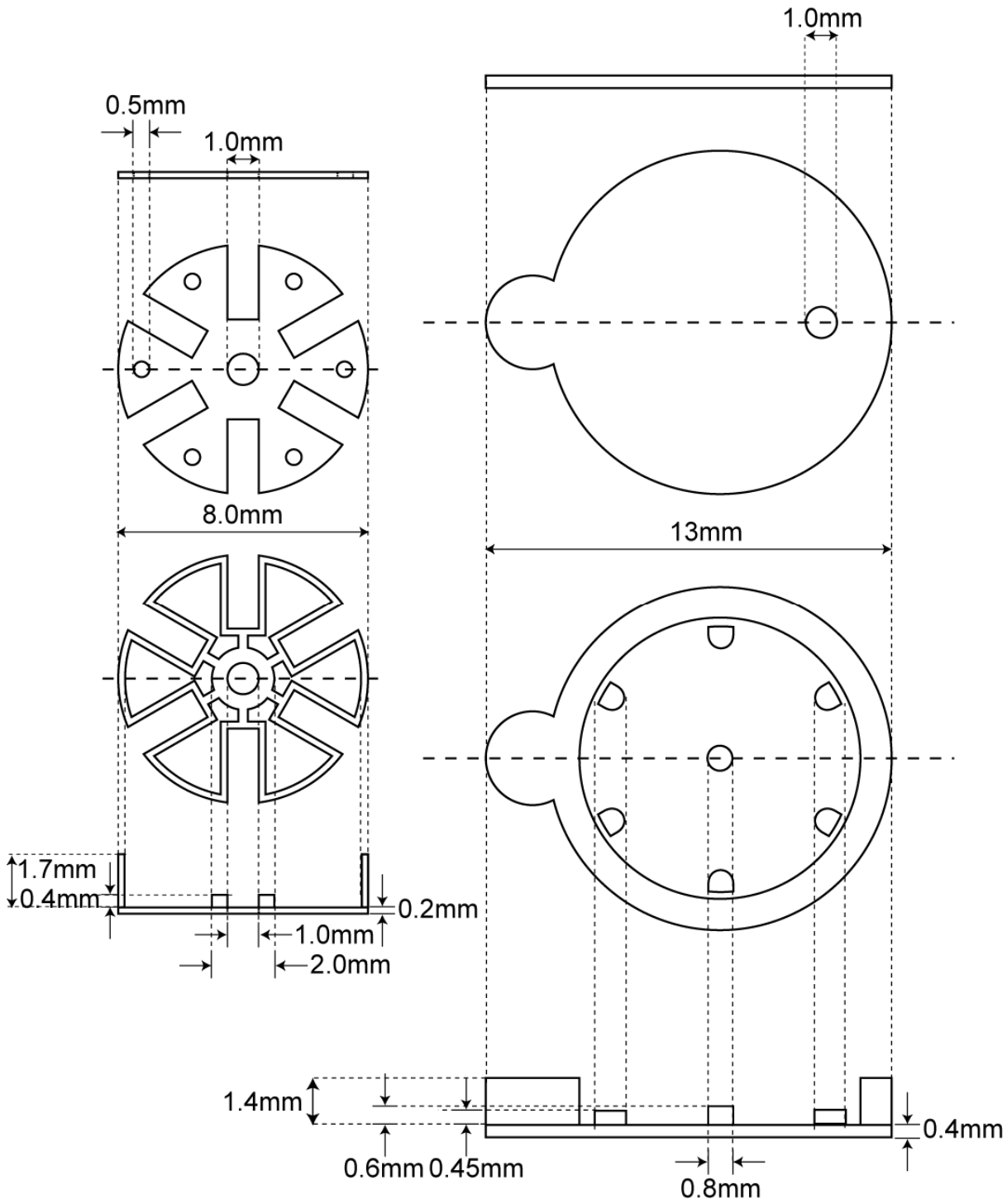

Figure 5.1: Schematic of single-gear hydrogel MEMS device for delivery of doxorubicin showing the dimensions of the various components within the device. The drawings show the cross-section of each component; the drug-containing gear (left) and the supporting structure of the device (right). Each reservoir in the gear has apertures measuring 0.5mm. When the device is in operation, these apertures align with the 1mm window that is located on the top-most layer of the device. The various dimensions of

the device are as described in the figure.

Following device fabrication, any uncrosslinked prepolymer was removed from the devices. The devices were then allowed to equilibrate in PBS for about 24 hours. Each device is then filled with 5 doses of doxorubicin. Each dose is calculated to be ~10% of a standard chemotherapy dose (scaled to the body mass of a mouse). As a standard dose for a 20g mouse is 50μg of doxorubicin (based on a 2.5mg/kg dose)[88], we injected 5μg of doxorubicin into each reservoir via the apertures in the device using a NanoFil syringe (World Precision Instruments, Sarasota, FL). The device was actuated with a magnet so that each reservoir can be accessed via the apertures. Each device was then incubated in 3mL of PBS at 37ºC in 24-well plates. The devices were actuated once every 2 days (q2d) or 4 days (q4d) using a magnet. The incubating solution was sampled daily; 200μL of solution was sampled and the fluorescent signal of doxorubicin present in the incubating solution was measured using a microplate reader (BioTek Synergy 5 Hybrid Multi-mode Microplate Reader). Doxorubicin has an inherent fluorescence signal and the presence of doxorubicin in the incubating solutions was detected by using an excitation wavelength of 479nm and reading the emission wavelength at 593nm. 200μL of fresh PBS was replaced each time a sample was drawn from the incubating solution. We then compared the release of doxorubicin for devices that were not actuated, actuated once every two days (q2d) and actuated once every 4 days (q4d).

5.1.1.3 Results and discussions

The release of doxorubicin from the devices is shown in the Figure 5.2. It was found that we were able to increase the rate of release of doxorubicin from the device by increasing the frequency of actuation (Figure 5.2C). However, for devices that were actuated once every four days (q4d), only about 62% of the total payload was deliver after 20 days. This is only a slight increase from the non-actuated control devices after 20 days (~45%). This is possibly due to the diffusion of doxorubicin within the device; the small apertures for each reservoir and clearances

between the gear and the top layer of the device allows for a small amount of doxorubicin to diffuse into the inner space of the device and eventually into the surrounding solution. For the devices that were actuated every 2 days (q2d), we found that ~87% of the total payload was released after 10 days. This is a great increase compared to control devices (~20% background leakage of doxorubicin) and devices that were actuated once every 4 days (q4d, ~45% release). Since we are considering the efficacy of using a local delivery device that can deliver low doses of chemotherapy at a higher frequency of dosing without accompanying side effects, this is an encouraging result. Also, there has been evidence of therapeutic advantage in administering chemotherapy on a high-frequency/low-dose schedule even when administered systemically[89]. Thus this design and dosing schedule was then used for *in vivo* studies with a mouse osteosarcoma model (Chapter 6).

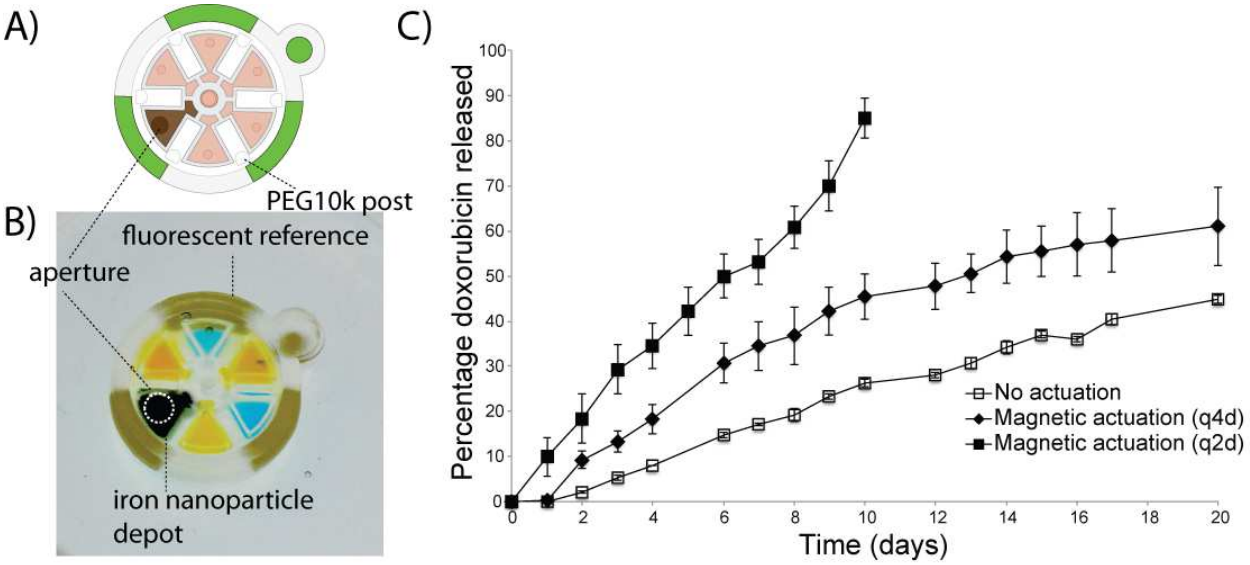

Figure 5.2: In vitro release of doxorubicin from a single-gear hydrogel MEMS device. A) Schematic and B) image of the single gear device used for delivering payloads of doxorubicin. A) and B) show a single-gear device with 5 reservoirs available for drug-loading. In B), the reservoirs were filled with different colored dyes in order to better elucidate the shape and location of the reservoirs. Fluorescent references in the capsule of the device and its asymmetric design were to aid future *in vivo* imaging of the device. C) Shows the release of doxorubicin over time. The release of doxorubicin from devices with different actuation schedules were expressed in terms of percentage of the totally doxorubicin loaded into each device.

5.1.2 *In vitro* release of multiple types of payload from a Geneva drive device

In order to demonstrate a further functionality of the hydrogel MEMS devices, we were interested in potentially delivering two different types of payloads/drugs with the added capability of being able to select which payload would be delivered. For these experiments, Geneva drive devices were fabricated (schematic in Figure 5.3) and filled with two different fluorescent-labeled dextrans.

5.1.2.1 Methods

Geneva drive devices were fabricated as described in Chapters 3 and 4. Figure 5.3 shows the dimensions of the various components in the device. After device fabrication, uncrosslinked prepolymer was removed from the devices and they were then allowed to equilibrate in PBS for ~24 hours. A NanoFil syringe was then used to inject AlexaFluor680 (AF680)-dextran (10kDa, Life Technologies, Carlsbad, CA) and FITC-dextran (20kDa, Sigma-Aldrich, St Louise, MO) through the apertures. The device was actuated with a magnet in order to gain access to the different reservoirs. The different dextrans were injected in an alternating manner into the devices. The molar concentration of dextran injected into each reservoir was the same (1mM). The location of the different types of dextran in the driven gear is shown in the schematic in Figure 5.4). Following injection of dextran, each device was then incubated in 3mL of PBS in 24-well plates at 37ºC. The devices were then actuated daily and the incubating solution was sampled 24 hours after each actuation. After each sampling, the devices were placed in 3mL of fresh PBS and actuated again. The amount of AF680-dextran (Ex:550nm, Em:702nm) and FITC-dextran (Ex:493nm, Em:519nm) in the incubating solution was measured using a microplate reader.

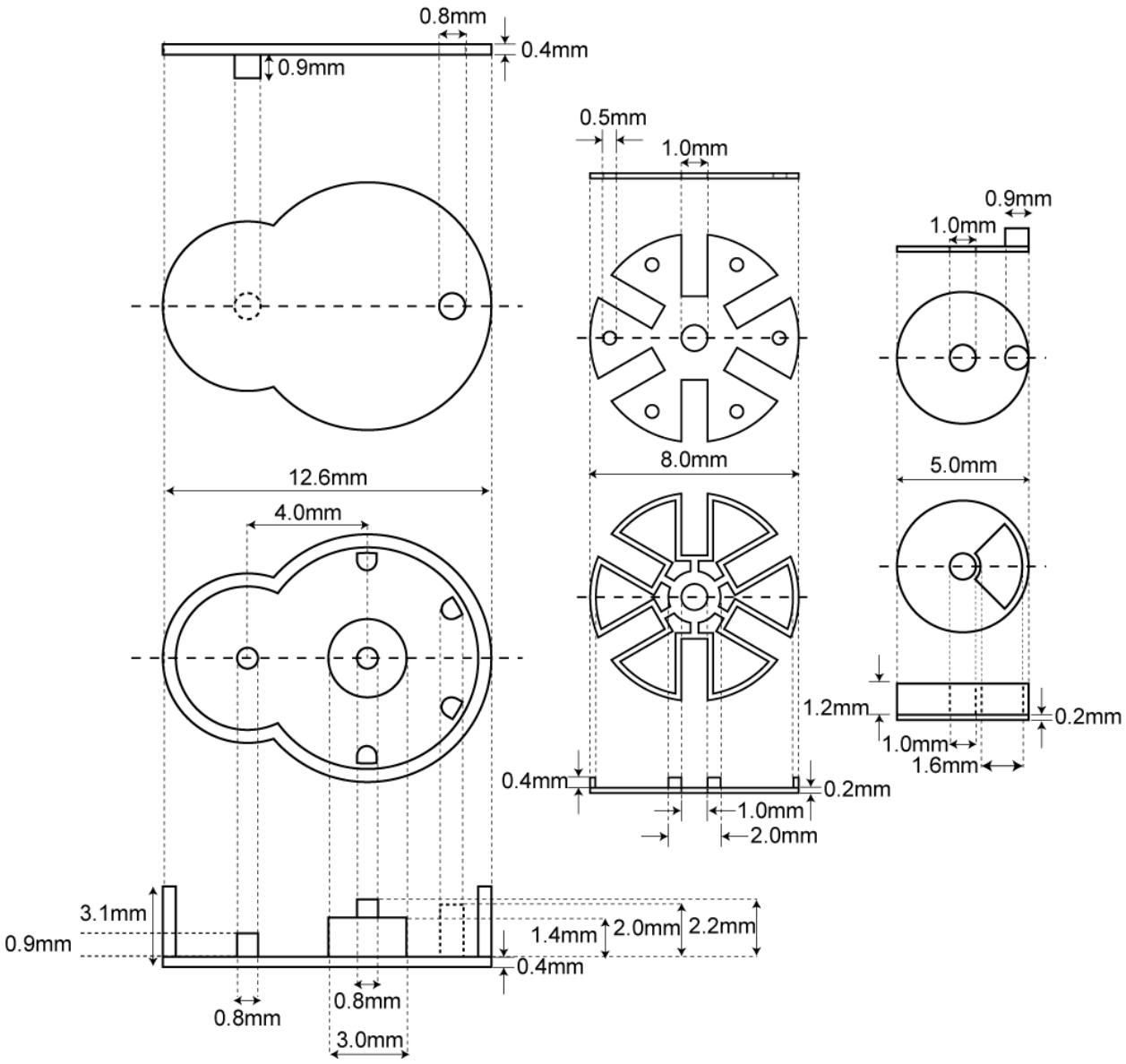

Figure 5.3: Schematic of Geneva drive hydrogel MEMS device showing the dimensions of the various components in the device. The bulk of this device was constructed in PEG400. The left panel shows the top and cross-section view of the supporting structures, including 2.0mm tall PEG10k posts. The middle panel shows the top and cross-section view of the driven gear. The top of each drug reservoir is designed to have a 0.5mm aperture that aligns with a 0.8mm aperture on the top layer of device during device operation. The driving gear (right panel) has a pin that measures 0.9mm in diameter. This pin engages with 1mm wide slots on the driven gear during device operation.

5.1.2.2 Results and discussions

The release of dextran from the Geneva drive device can be seen in Figure 5.4

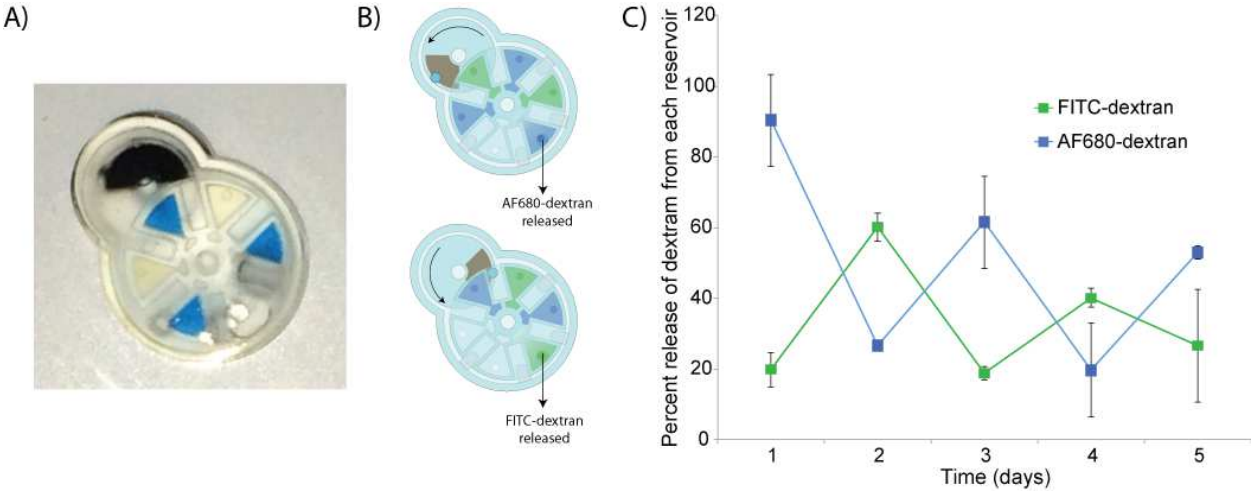

Figure 5.4: *In vitro* release of AF680-dextran and FITC-dextran from Geneva drive hydrogel MEMS device. A) Image of a Geneva drive device loaded with AF680-dextran and FITC-dextran. The first reservoir that is aligned to the top aperture is left empty for the "off" position. B) Schematic of the Geneva drive in operation. The first actuation will results in AF680-dextran to be released, followed by FITC-dextran. C) Release of dextran in vitro as measured by the fluorescent signal of the incubating solutions. The released is expressed in terms of percent of the amount of dextran loaded per reservoir. Since the reservoirs were filled in an alternating manner, after each actuation, we can see that the type of dextran being released alternates between AF680-dextran and FITC-dextran.

As can be seen from Figure 5.4 C, we were able to have a certain amount of control over the type of dextran that was to be released from the device. After the first actuation, ~90% of the first dose (AF680-dextran) was released while we only observed a ~20% background leakage of FITC-dextran. After the second actuation, we see a sharp rise in the amount of FITC-dextran in the incubating solution (~60%) while observing a decrease in the amount of AF680-dextran released (<30% due to background leakage). However, it is noticed that this effect of alternating increases in concentrations decreases over time and this is probably due to the background leakage of the device; as more of the payload passively diffuses out, there is less dextran that is

released with each active actuation. However, this could potentially be improved by changing the design of the device to ensure there are smaller clearances/gaps between the gears and the surrounding structures to decrease pathways for leakages to occur. Nevertheless, this is still an encouraging result and demonstrates the added capabilities of our device compared to other hydrogel-based drug delivery devices. This added capability would be immensely useful in situations where multiple drugs have to be delivered at specific times according to a progression of a disease or based on the response of a patient to treatment.

5.2 *In vivo* implantation of devices: mechanical robustness and *in vivo* delivery of payload.

We tested the robustness of hydroge MEMS devices upon subcutaneous implantation into a mouse model. This is to ensure the mechanical integrity of the device upon implantation as well as the robustness of our actuation method. We also assess the capability of the device in specifically delivering different types of payloads into an *in vivo* model. Prior to device implantation, we also conducted an *in vitro* cytotoxicity assay to confirm the biocompatibility of our PEGDA gels

5.2.1 Methods

5.2.1.1 In vitro biocompatibility of PEGDA hydrogels.

A simple *in vitro* biocompatibility test was conducted on different PEGDA gel compositions using a direct contact method. PEGDA gels of various compositions were polymerized and cut into disks (diameter: 2mm, height: 1mm). The gels were then rinsed 3 times with PBS and then incubated in PBS overnight at 37^{o}C to allow any uncrosslinked polymers to be rinsed off. The gels were then transferred into PBS supplemented with 1% penicillin-streptomycin. Dermal foreskin fibroblast cells were cultured in Dulbecco's Modification of Eagle's Media (DMEM, L-

glucose, L-glutamine and sodium pyruvate supplemented) supplemented with 10% Fetal Bovine Serum (FBS). Both items were purchased from Corning Cellgro (Mediatech, Inc., Manassas, VA). Confluent flasks of fibroblast cells were trypsinized, neutralized with fresh DMEM supplemented with 10%FBS and centrifuged at 300g for 5 minutes. Cells were then resuspended and counted using a hemocytometer. Fibroblasts were then seeded into a 96 well plate at a density of 5000cells/well. The cells were left to incubate at 37^{o}C overnight to allow for cell attachment. After incubation, PEGDA disks were then placed at the bottom of each well and let to incubate for 48 hours. After 48 hours, disks were removed with a tweezer, followed by removal of media. 200µL of fresh media was added to each well, followed by 20µL of alamarBlue^{TM} (10x concentration, Thermo Fisher Scientific, Pittsburgh, PA). The cells were then left to incubate for another 3 hours in the presence of alamarBlue^{TM}. Fluorescence readings (Excitation: 550nm, Emission: 590nm) were then taken using a microplate reader (BioTek Synergy 5 Hybrid Multi-mode Microplate Reader). Cell proliferation in each well was compared to a positive control of dermal fibroblasts cultured without PEGDA gels.

5.2.1.2 *In vivo* implantation of hydrogel MEMS devices.

Device fabrication.

Geneva drive devices were fabricated as previously described. After equilibrating in PBS for 24 hours, the devices were rinsed with sterile PBS and UV sterilized in a biosafety cabinet for 40 minutes. They were then injected with sterile AF680-dextran and FITC-dextran solutions in an alternating manner (See section 5.1.2). The devices were then left in PBS supplemented with 1% Penicillin-streptomycin prior to implantation.

Surgical techniques.

Two 9-week-old, athymic male nude mice (NCRNU-M, Taconic Farm, Albany, NY) were anesthetized with a ketamine/xylazine cocktail. Immediately after induction, each mouse was

given injections of buprenorphine (subcutaneously at the scruff of the neck) and lidocaine (subcutaneously at the site of incision). Following 3 cycles of povidone/iodine and ethanol scrubs, a ~ 1cm incision was made on the flank of the mouse and a subcutaneous pocket was made. The pockets were filled with PBS and the hydrogel device was placed deep within the pocket. Incisions were closed with mattress sutures using synthetic, non-absorbable monofilament 4-0 sutures (Henry Schein). All animal work was conducted in accordance with an animal protocol approved by IACUC.

5.2.1.3 *In vivo* actuation and imaging.

After surgery, the mice were imaged using a Maestro Cri In vivo Imager in order to visualize the device. The device has fluorescent markers present on its exterior as well as on the driven gear. A Neodymium magnet was used to actuate the device to release either a dose of AF680-dextran or FITC-dextran. The mice were then returned to the animal facility. After 24 hours, they were anesthetized and imaged again. The implanted devices were actuated again. The devices were actuated in a way that the same type of dextran was released as for the previous day; each mouse received either AF680-dextran OR FITC-dextran only. The mice were then returned to the animal facility again. 24 hours later, the mice were euthanized and the devices were explanted from them. After device explantation, the mice were imaged for AF680 and FITC. The devices were explanted before the final imaging so as to avoid interferences from the highly fluorescent materials inside the device. Once the device is removed, we were able to see the levels of fluorescence that remained on the tissue of the mice that were in immediate contact with the device.

5.2.2 Results and discussions

5.2.2.1 *In vitro* biocompatibility of PEGDA hydrogels.

Cell viability of dermal fibroblasts cultured in the presence of PEGDA hydrogels was compared to that of a positive control (cells cultured in media alone) using an alamarBlue cell proliferation assay. Figure 5.5 shows that there was little ill-effect of culturing cells in the presence of PEGDA hydrogels.

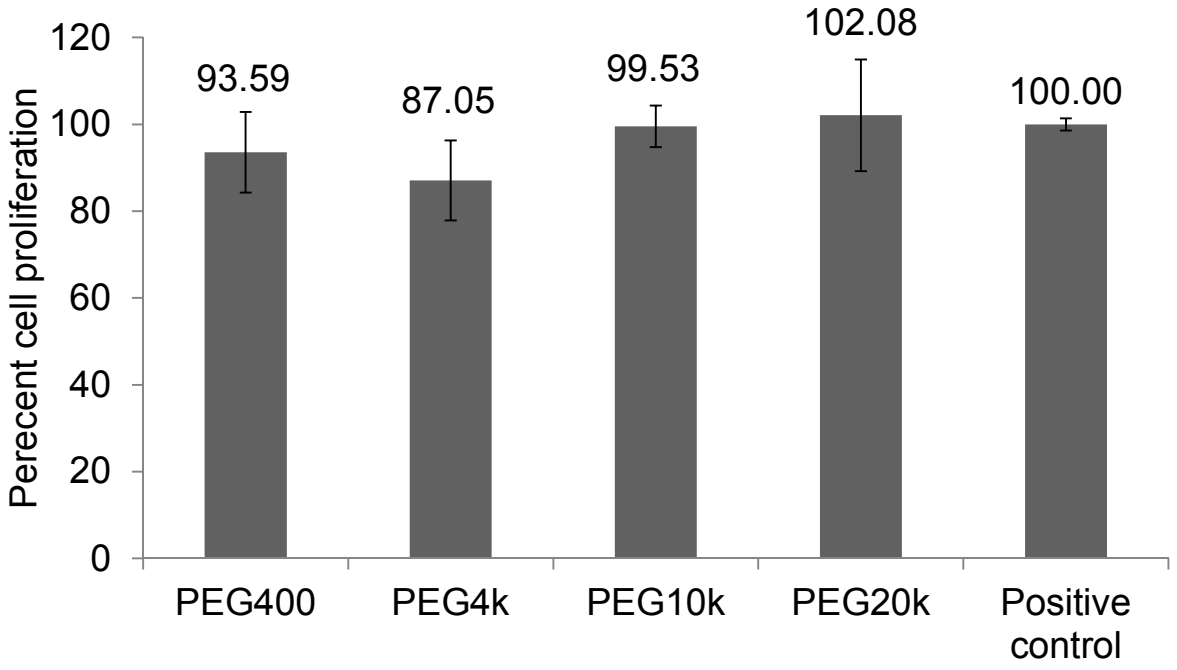

Figure 5.5: Percent cell proliferation of dermal fibroblasts cultured with PEGDA hydrogels. The graph shows the percentage cell proliferation of dermal fibroblast cells after 48 hours of culture in direct contact with PEG400, PEG4k, PEG10k and PEG20k hydrogels (n=8 for each gel type) as compared to cells that were cultured in media alone (positive control). Corresponding p-values: PEG400=0.986, PEG4k=0.924, PEG10k=0.962, PEG20k=0.990

As can be seen from the graph in Figure 5.5, percent cell proliferation for all gel compositions were well over 80% of that compared to the positive control with all but one gel type (PEG4k) having more than 90% cell proliferation. A Student's t-Test was also performed and the

corresponding p-values (Figure 5.5) were >0.900 for all compositions, indicating there is no statistical difference between the cells that were cultured with PEGDA gels and the control group. Also, from images taken of the cells growing in the presence of PEGDA gels (Figure 5.6), we can see that the morphology of the cells are comparable to that of the positive control. Hence from these results we can conclude that these compositions of PEGDA gels were biocompatible as they did not demonstrate any cytotoxicity in vitro.

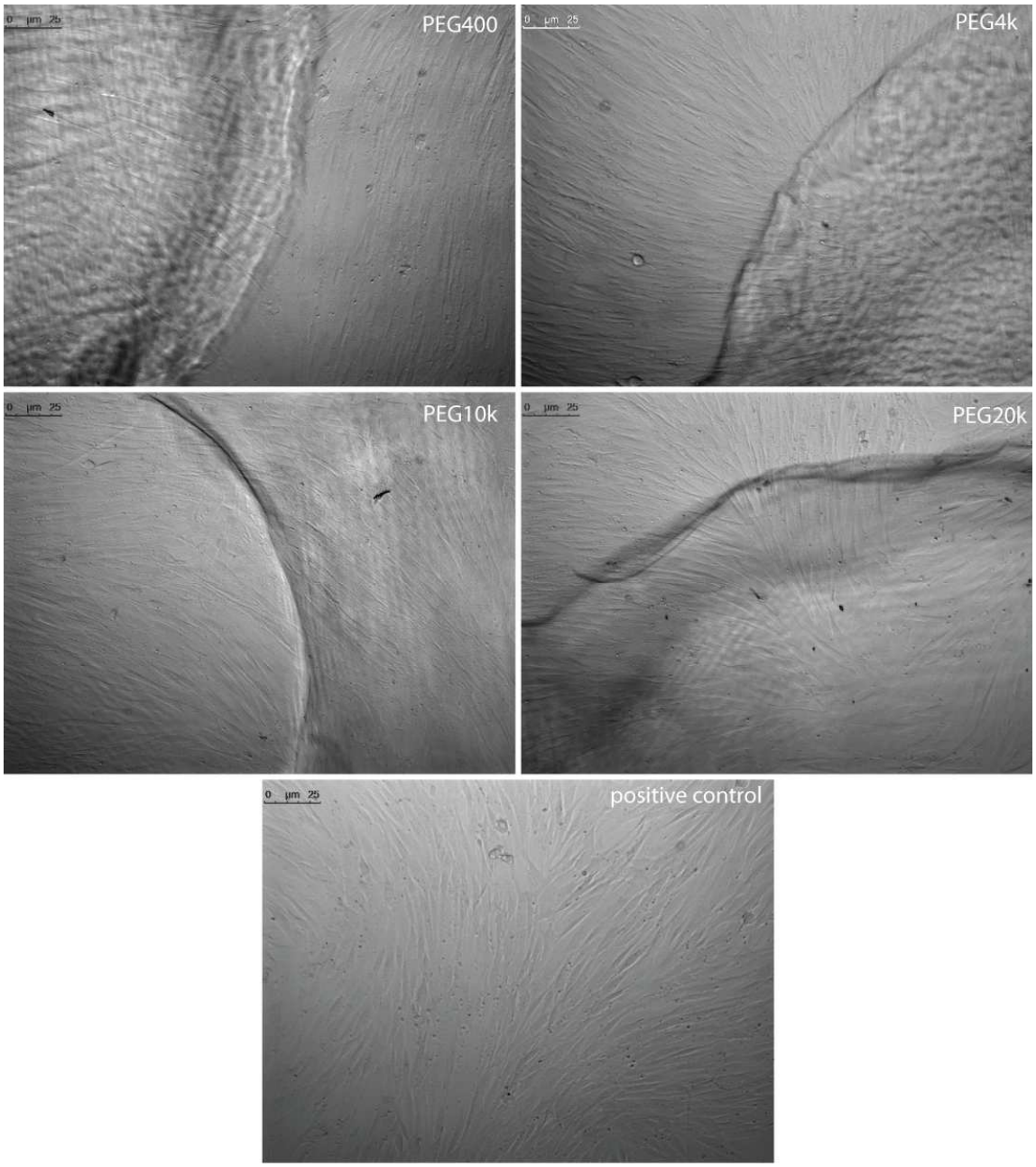

Figure 5.6: Images of cultured dermal fibroblast cells in the presence of PEGDA hydrogels. PEG400, PEG4k, PEG10k, PEG20k were placed in direct contact with dermal fibroblast cells. Images show that they are morphologically similar to that of positive controls. Cells can also be seen growing beneath gel compositions that are transparent.

5.2.2.2 *In vivo* implantation of hydrogel MEMS devices.

The mechanical robustness of this device after subcutaneous implantation is demonstrated via in vivo imaging (Figure 5.7).

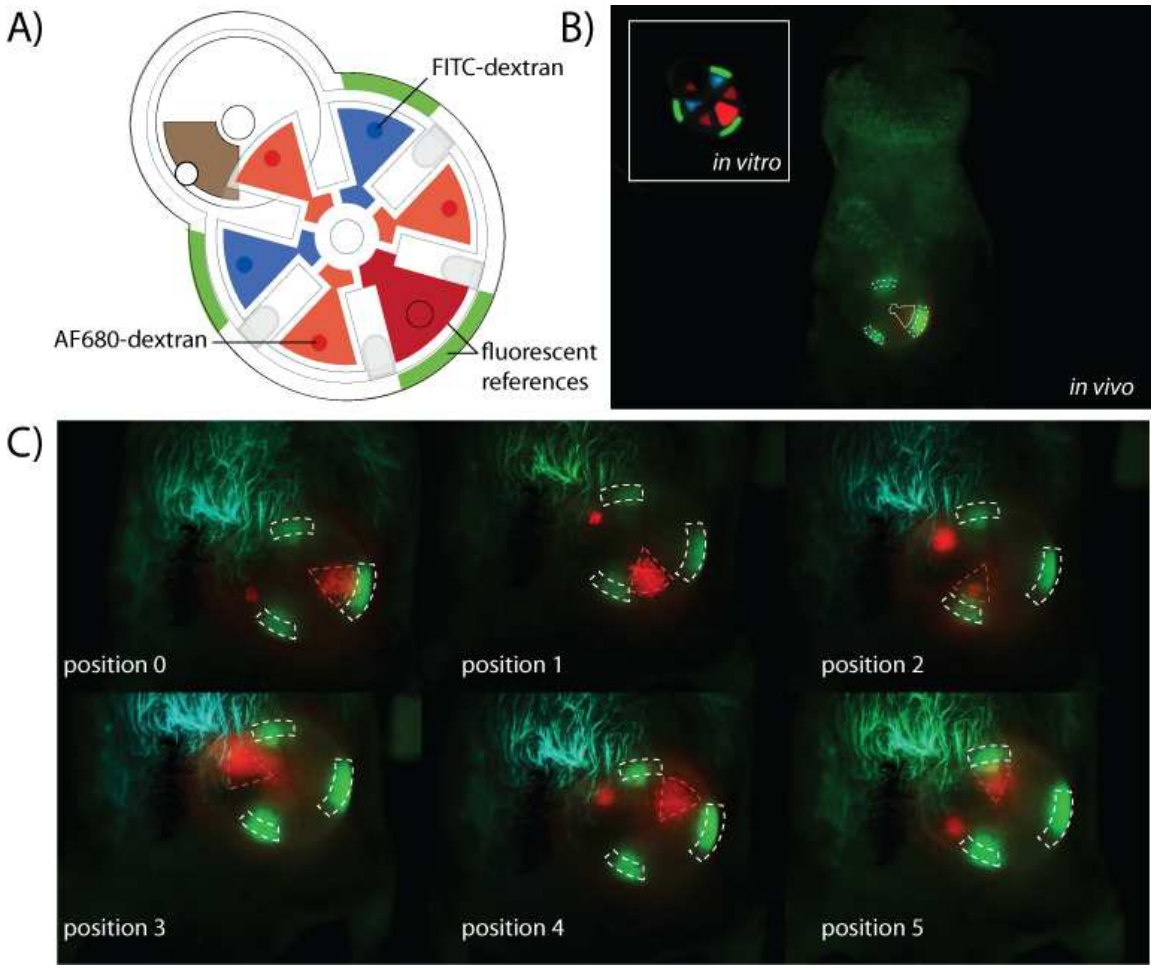

Figure 5.7: Schematic of implanted Geneva drive hydrogel MEMS device and its operation *in vivo*. A) This schematic shows the various fluorescent components in the Geneva drive. Two types of fluorescent references (fluorescent beads immobilized in PEG400 gel) were used to visualize the movement of the device. The red fluorescent reference on the gear is placed under the aperture at the start of the experiment (position 0/"off"). The reservoirs adjacent to the fluorescent reference were filled with AF680-dextran solutions and the other reservoirs were filled with either FITC-dextran or AF680-dextran in an alternating manner. B) Images taken by the Maestro Cri In Vivo imager. The inset shows an image of the device before implantation. Each fluorescent species can be differentiated by their unique wavelengths. Following implantation, the Geneva drive device can be imaged through the skin of the mouse. The fluorescent references can be clearly seen. C) Operation of device during magnetic actuation. In vivo imaging allows us to see the "state" of the device; the location of the fluorescent reference on the driven gear. With each full rotation of the driving gear, the driven gear moves through position 0-6.

As can be seen in Figure 5.7, fluorescent references are incorporated into the device to aid with the imaging of the device. These references were constructed by incorporating fluorescent

microbeads into the different structures of the device. By imaging for these references, we are able to see the movement of the gears within the device. These imaging experiments showed that the device maintains its mechanical integrity after subcutaneous implantation and we are able to precisely actuate the device using external magnets. The schematic in Figure 5.4B also lays out the location of the AF680-dextran and FITC-dextran reservoirs within the Geneva drive. The colors in the schematic correspond to the different filters used with the Maestro Cri In Vivo imager to differentiate between the different fluorescent emissions. It is noted that the resolution of the dextran-filled reservoirs greatly deteriorates after the device has been implanted into the mouse. We were not able to see the individual chambers. These chambers have a much lower fluorescent signal compared to the fluorescent beads used as fluorescent references on the device. It is possible that this loss of resolution is due to the very thin reservoirs within the device in addition to having to image through layers of PEGDA and skin. Nevertheless, we were able to very clearly see the fluorescent references and show that the driven gear is able to move through positions 0 (starting position) to 5 (corresponding to the last “dose” being delivered)

In order to demonstrate that we are capable of specifically delivering different types of payload, the implanted devices were actuated such that only one of two fluorescent dextrans is released for each mouse. One mouse was only “dosed” with AF680-dextran while the other was only “dosed” with FITC-dextran (Figure 5.6). As described in Figure 5.7, the mouse on the left column was only given two doses of AF680-dextran, once at t=0 and another at t=24hours. Thus at the start of the experiment, the driving gear is rotated once to bring the driven gear to “position 1” (Figure 5.7). At t=24hours, the driving gear is rotated twice to release another dose of AF680-dextran (corresponding to “position 3” in Figure 5.7). Conversely, the mouse on the right column is only given doses of FITC-dextran, once at t=0 and another at t=25hours. The driving gear is rotated twice at t=0 (“position 2” in Figure 5.7) and twice again at t=24 hours (“position 4” in Figure 5.7).

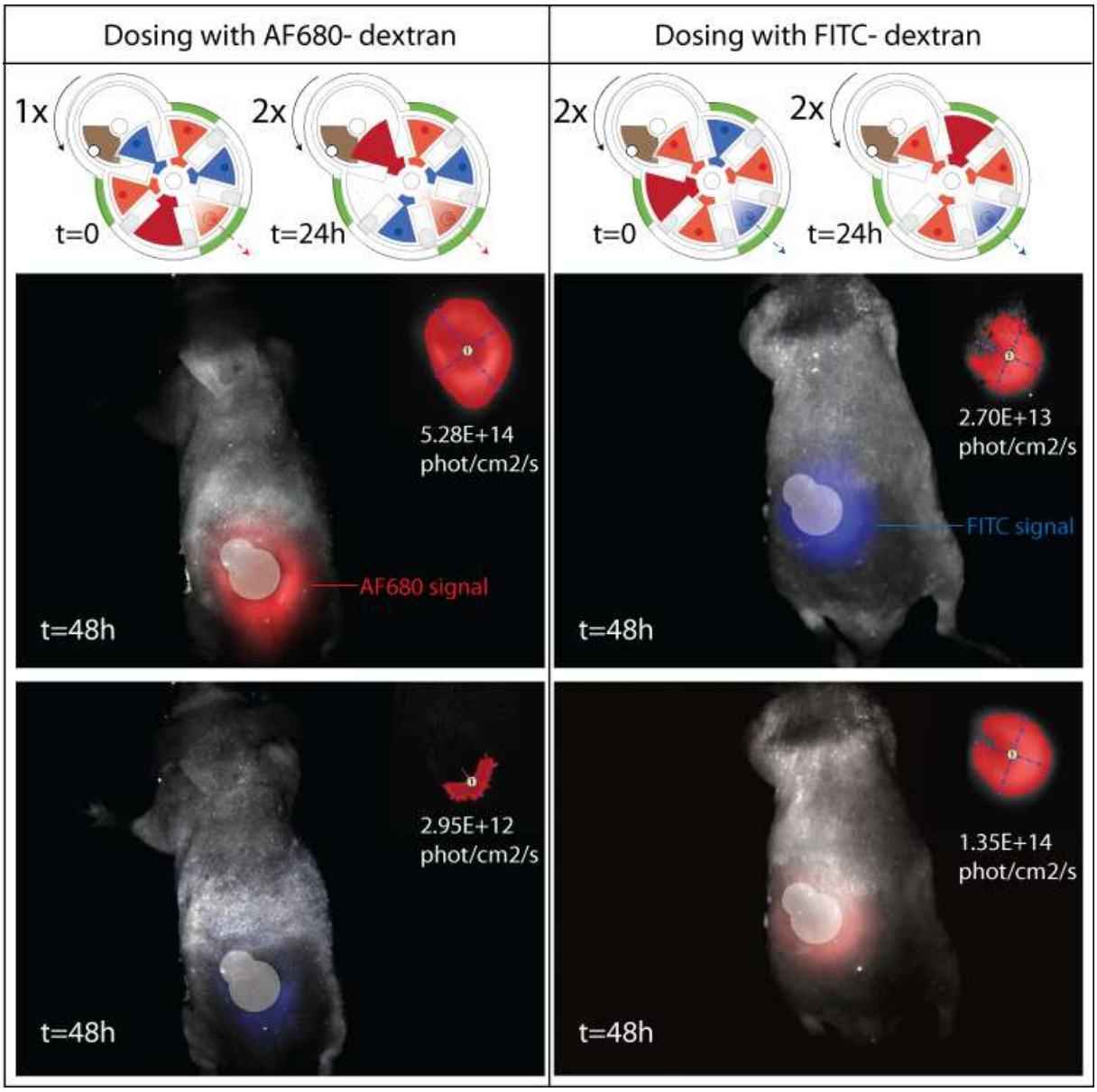

Figure 5.8: Dosing schedule for each mouse and the fluorescent signals detected at the end of each experiment. The left column shows the dosing schedule of the mouse that was only "dosed" with AF680-dextran. The mouse was given two doses of AF680-dextran at t=0 and t=24h. The right column shows the dosing schedule of the mouse that was only "dosed" with FITC-dextran. The mouse was given two doses of FITC-dextran at t=0 and t=24h. The 2x2 matrix of in vivo images show the fluorescent signals present in the mouse immediately after the device was explanted. The top row of the 2x2 matrix shows the fluorescent signal corresponding to the dextran that the mice were specifically dosed with. The bottom row of the 2x2 matrix shows the fluorescent signal corresponding to the other type of dextran (background leakage). The outline of the device is drawn to show the location of the device prior to explantation.

Indeed, we see that the fluorescent signal detected in the mice show that the chosen fluorescent-labeled dextran was delivered to the tissue surrounding the device (top row of 2x2 matrix of in vivo images in Figure 5.8). Additionally, if we compare diagonally across the 2x2 matrix of in vivo images in Figure 5.8, we see that the background leakage of the non-delivered dextran is much weaker than if it were actively delivered via magnetic actuation. By measuring the average intensity of the fluorescent signals (photons/cm^2/s), we see that background leakage of FITC-dextran for the mouse that dosed with AF680-dextran only was roughly 11% of the FITC signal measured in the mouse that was given doses of FITC-dextran. Similarly, the fluorescent signal due to background leakage of AF680-dextran in the mouse that was dosed with FITC-dextran was about 20% of the signal measured in the mouse that was given doses of AF680-dextran only.

5.3 Conclusion.

We have demonstrated that we can deliver payloads/drug using hydrogel MEMS devices. In *in vitro* demonstrations, we were able to control the release profile by changing the frequency of actuation. Additionally, in devices that were loaded with more than one type of payload, we showed that we could specifically select which payload that was to be delivered. We showed this second capability in an in vivo mouse model as well as demonstrate the mechanical robustness of the device post-implantation. This has never been demonstrated for a hydrogel-type device and we believe it holds a promising future for a new class of medical and drug delivery devices.

Chapter 6

An implantable PEGDA-based MEMS device for local, low-dose chemotherapy treatments

Current implantable drug delivery devices can be classified into two groups; devices that can be actively controlled by the patient/doctor after implantation and devices that lack active control where only a sustained release of therapeutics is maintained. Devices with active control typically resemble more traditional electronics/MEMS devices; their construction is based off of silicon technologies[5, 86], they contain electronic components[90] and often require an on-board battery[91]. Thus, these devices are often not biocompatible, require special coatings for improved biocompatibility[18] and even then still require removal after they have performed their function. Biocompatible systems, on the other hand, belong to the group of devices that do not allow for active control. Often these biocompatible drug delivery systems consist of swollen polymer networks that gradually release their payload over time after implantation[46, 92, 93]. Thus, we believe that there is a need for a fully biocompatible implantable drug delivery device that allows for active control post-implantation. In this way, dosing schedules and/or the type of drug to be delivered can be changed according to the disease progression.

Another factor to consider is, depending on the location of implantation, drug delivery via an implantable device could result in a localized increase of therapeutics at the site of implantation. This could be beneficial for treatments such as chemotherapy, where clinicians would be interested in introducing a high concentration of chemotherapy drugs to a local site but not systemically due to the side-effects of chemotherapy. Thus we believe there is a benefit in developing implantable devices for local delivery of current chemotherapeutics at the site of tumors. A specific example will be that of post-surgery chemotherapy treatments for patients

with osteosarcoma. Often times, after a tumor has been resectioned, the patient has to undergo a course of chemotherapy. This is due to stray cancer cells that may remain after surgery especially in cases where it is difficult to resection the tumor with a negative margin. Therefore, to avoid local recurrence, chemotherapy is normally performed post-surgical removal of the tumor[94]. This course of chemotherapy is administered via IV and the patient will experience the full side effects of the drugs as chemotherapy has to be administered at a high enough dosage for it to travel through the circulatory system and arrive at the site where the tumor was removed.

Therefore, we believe this is a clinical application that would be well suited for our device. Potentially, after a surgeon has excised a tumor from a patient, a hydrogel MEMS device containing small doses of chemotherapy can be implanted at the site of the surgery. After the surgical wounds have healed, the device can then be actuated to release doses of doxorubicin locally to kill any cancer cells that may remain at the site of surgery.

6.1 Mouse osteosarcoma model

In order to assess the feasibility of this strategy, we first established a mouse osteosarcoma model. Luciferase-tagged human osteosarcoma cells (143B) were injected orthotopically into mice and tumors were allowed to form. Tumor growth can then be monitored using bioluminescence imaging. 143B cells were used for xenografting because of their known aggressive growth in mouse models[95].

6.1.1 Materials

143B osteosarcoma cells, which were transfected with the luc2 gene, were very generously provided by Prof. Francis Y. Lee. These cells allow for easy monitoring of tumor growth in an in vivo model. Dulbecco's Modification of Eagle's Media (DMEM, L-glucose, L-glutamine and

sodium pyruvate supplemented) and Fetal Bovine Serum (FBS) were purchased from Corning Cellgro (Mediatech, Inc., Manassas, VA). D-Luciferin, monopotassium salt was purchased from Thermo Fisher Scientific (Pittsburgh, PA). NCNRU-M mice (male, nude athymic) were purchased from Taconic Farms (Albany, NY).

6.1.2 Methods

The 143B cells were cultured with FBS supplemented DMEM. Confluent cells were trypsinized, centrifuged and resuspended in PBS. The suspension of cells was diluted to form $20x10^6$cells/mL suspensions. Syringed with 30G needles were each filled with 50μL of this 143B cell suspension (ie: $1x10^6$cells per syringe). The nude mice were first anesthetized with a ketamine/xylazine cocktail. Following induction, they were given buprenorphine (subcutaneous). A 27G needle was used to core the femur of the mouse. After coring, the prepared syringes of 143B cells were used to inject the cells into the instraosseous space of the femur. The mice were then monitored everyday until the tumors were formed and were palpable (~3 weeks).

The growth of the tumor was monitored using in vivo bioluminescent imaging. Mice were anesthetized then injected with 100μL D-luciferin solutions (30mg/mL) intraperitoneally. 5 minutes after injection, bioluminescent imaging was conducted using the Maestro Cri In Vivo imager. The mice were placed in the imager with the bulk of the tumor facing the camera in the imaging chamber. The mice were typically in a prone position or lying on their side such that the entire thigh is visible. A 540s exposure time was used for each mouse (the luminescent signal stays stable for 20 minutes) and the integrated software was used to measure the bioluminescence intensity of the tumor (photons/cm^2/s).

6.1.3 Results and discussions

After 3 weeks, a palpable tumor was developed in all the mice. Figure 6.1 shows the typical images and bioluminescent intensity signals obtained from the Maestro Cri In Vivo imager

during tumor growth monitoring. As can be seen from the in vivo images (Figure 6.1A), the mice were placed in the imaging chamber such that the bulk of the tumor was visible during imaging. Throughout monitoring, the images were taken at the same position every 4 days. The bioluminescent intensity, as well as surface area of the tumor increased over time. The intensity of the bioluminescent signal was also quantified using the integrated Maestro Cri software. As can be seen from the plot of the total signal (photons/cm^2/s) over time (Figure 6.1B), there was approximately a 12-fold increase in bioluminescent intensity over the course of 20 days (41 days after 143B cell injections).

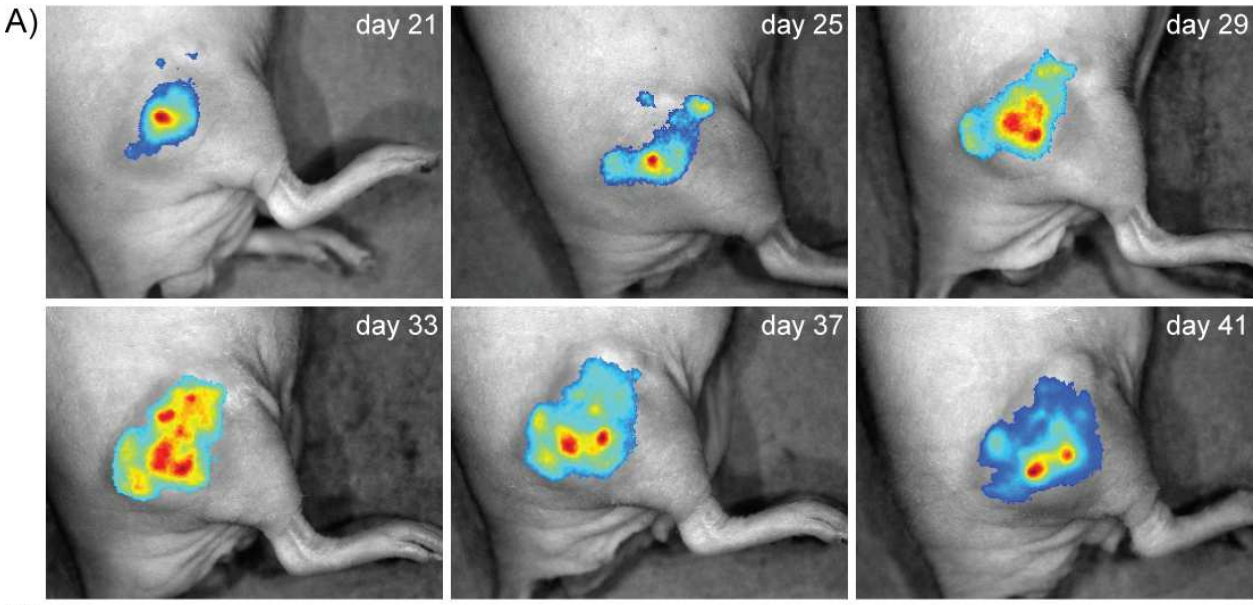

B)

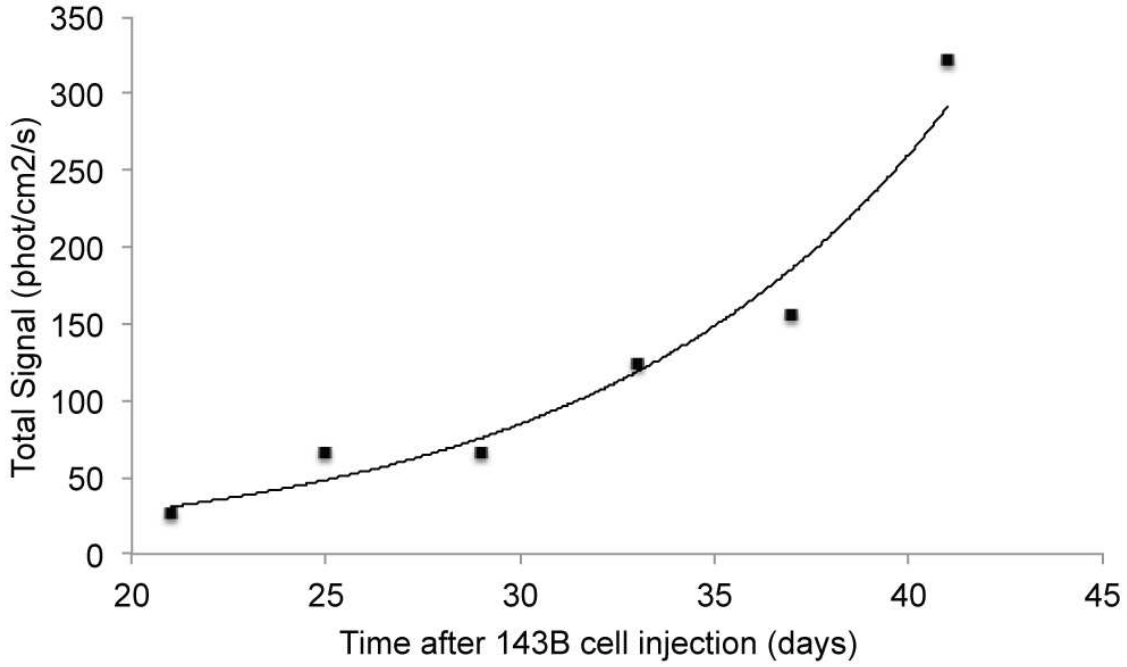

Figure 6.1: Monitoring of tumor growth via bioluminescence imaging. A) In vivo bioluminescent images showing growth of tumor over time. Images were taken every four days and the intensity of the bioluminescent signal was quantified. B) Plot of total bioluminescent signal from the tumor over time (n=1).

Due to variations in starting tumor sizes across all the mice, we typically normalized the intensity signal with starting signal measured at 21 days after 143B cell injections (I_0). Thus we monitor tumor growth in terms of increase the increase in bioluminescent signal over time (I/I_0). Figure 6.2 shows the plot of the increase in bioluminescent intensity over time for a control group of mice (no treatment, n=3)

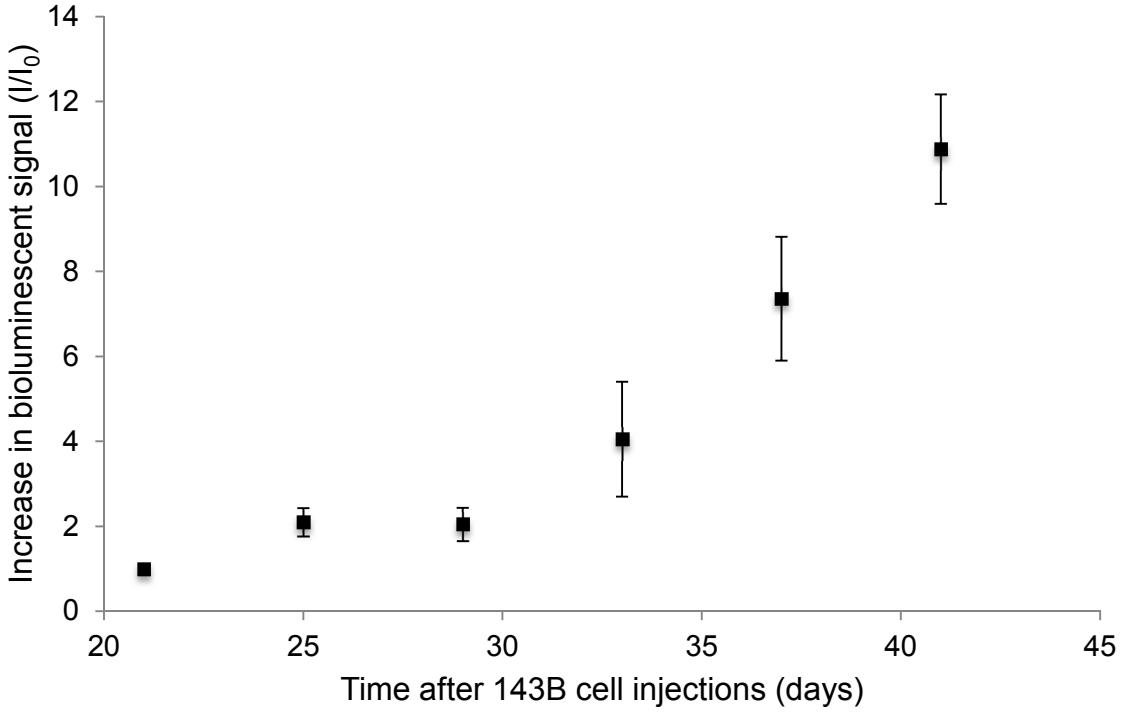

Figure 6.2: Increase in bioluminescent signal of tumor over time. This plot shows the increase in bioluminescent signal expressed as the ratio of the detected signal to the starting bioluminescent intensity at day 21 (I_0) over time.

6.2 Local *in vivo* delivery of doxorubicin in an osteosarcoma model

We studied the efficacy of using hydrogel MEMS devices to deliver a standard chemotherapy drug to the site of a tumor. Each device carried a payload of 5 doses of doxorubicin with each dose amounting to ~10% of a standard dose of chemotherapy that would be administered systemically (rough estimate of percent weight of tumor to body mass). Due to the lower levels

of doxorubicin in each dose, we postulated that we would be able to deliver the doses at a higher frequency compared to the standard treatment without the harmful side effects of doxorubicin (eg: cardiotoxicity). In this manner, we would be able to safely deliver higher doses to the tumor while avoiding the effects of cardiotoxicity.

6.2.1 Methods

Single gear devices were prepared as described in Section 5.1.1. Following fabrication and equilibration in PBS, the devices were rinsed with sterile PBS and UV sterilized in a biosafety cabinet for 40 mins. Sterile doxorubicin solutions were then injected into each reservoir using a NanoFil syringe. Each reservoir was injected with ~0.5μL of a 10mg/mL solution of doxorubicin. Hence each reservoir contains 5μg of doxorubicin. The doxorubicin-loaded devices were stored in 1% penicillin-streptomycin solutions in PBS until they were ready to be implanted. Mice were orthotopically injected with luciferase-tagged 143B osteosarcoma cells as described in section 6.1. The tumors were allowed to grow for 3 weeks before implantation.

The mice were randomly assigned to 4 groups (*n*=3 for each group):

(i) **Local device dosing, q2d (n=3).** Local low-dose delivery of doxorubicin using single-gear device. Doxorubicin-loaded hydrogel MEMS devices were subcutaneously implanted close to the site of the tumor. The device was actuated once every 2 days (q2d) to release doses of doxorubicin. Each actuation would release 5μg of doxorubicin (10% of standard dose). A total of 5 doses was administered (25μg)

(ii) **Low dose, q2d, intraperitoneal (n=3).** Systemic treatment with low doses of doxorubicin every 2 days (q2d). Each mouse in this group was treated with intraperitoneal injections of 5μg of doxorubicin (10% of standard dose). This level of

dosing and frequency was selected so as to compare systemic vs local delivery with the device (see group (iii)). A total of 5 doses was administered (25μg)

(iii) **High dose, q4d, intraperitoneal (n=3).** Systemic treatment with high standard dose of doxorubicin every 4 days (q4d, ~2.5mg/kg)[88]. Each mouse in this group was treated with intraperitoneal injections of 50μg of doxorubicin (assuming 20g mouse). A total of 5 doses was administered (250μg)

(iv) **No treatment (n=3).** No doxorubicin was administered to this group of mice.

Group	Doxorubicin treatment details			
	M_{dox}/dose (μg)	Frequency	Route	Cumulative dose (μg)
i	5	Once every 2 days, q2d	Local	25
ii	5	Once every 2 days, q2d	Intraperitoneal	25
iii	50	Once every 4 days, q4d	Intraperitoneal	250
iv	No treatment			

Table 6.1: Doxorubicin dosing schedule for different treatment groups. The table describes the dose amount (M_{dox}/dose : mass of doxorubicin per dose administered), dosing frequency, route of administration, and the cumulative dose of doxorubicin administered at the end of the experiment.

Table 6.1 summarizes the treatment schedule for the various groups. For the group receiving treatment via our implantable hydrogel MEMS device, placement of the device was very important. The device was placed close enough such that it came in contact with the tumor but not in a position such that it affected the bioluminescent imaging. Thus, we placed the device on the back of the mouse, with the aperture of the device located at the proximal end of the femur (in contact with the tumor). In vivo imaging was then performed with the mouse lying on its side but with the bulk of the tumor still facing the camera. In this manner, the device did not obstruct the bioluminescent signal from the tumor (Figure 6.3). Mice in group (i) also received implants 24 hours before the first dose was administered to allow for the recuperation of the mice.

Bioluminescent imaging was performed on the mice as described in Section 6.1. All groups were imaged before the start of treatment to obtain the starting bioluminescent intensity (I_0). Bioluminescent imaging was then performed every time a dose was administered (2 or 4 days). The increase in bioluminescent signal over time (I/I_0) for the various treatment groups were quantified and compared. At the end of the treatment courses (10 days total, 24 hours after the final fifth dose was administered), the mice from groups (i) and (ii) were euthanized using CO_2 followed by cervical dislocation to confirm death. Mice from group (iii) were euthanized after 20 days so that a total of 5 doses of doxorubicin could be administered. The tumors and hearts of each mouse was then harvested and sent for histological staining and analysis. Hematoxylin & eosin (H&E) staining and TUNEL (terminal deoxynucleotidyl transferase dUTP nick end labeling) staining was performed on each tissue to check for cell apoptosis. The implanted devices, along with the skin and fibrous capsule surrounding the devices, were also sent for histological staining and analysis (H&E and Trichome staining).

6.2.2 Results and discussions

6.2.2.1 *In vivo* performance of Geneva drive device

We were able to implant doxorobucin-loaded devices into an osteosarcoma mouse model. In these experiments, the single-gear device was chosen over the Geneva drive device due to its smaller size. Since the tumor grows rather aggressively and has a large volume relative to the size of the mouse, a smaller device was preferred so as to have better wound healing after implantation. Implanting a large device would require larger subcutaneous pockets and result in excessive stress on the sutured wounds. Additionally, there was also a concern about the prolonged functioning of the Geneva drive in an *in vivo* environment. This is due to the complicated design of the Geneva drive compared to the single-gear device. Any cell infiltration into the device via the aperture could result in the device clogging up. Presence of cells or

proteins within the device could result in failure of pin-slot engagement in the operation of the device. Figure 6.3 shows images of an explanted Geneva drive (no doxorubicin) that was implanted for over a week into a nude mouse. As can be seen from the image, some cell infiltration had occurred within the device.

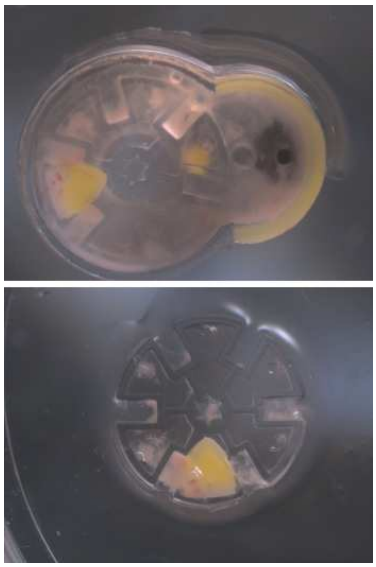

Figure 6.3: Images of an explanted Geneva drive hydrogel MEMS device. A Geneva drive device (with no payload) was used as a test implant into a nude mouse. After a week, the device was explanted. Presence of cell infiltration is shown in the interior of the device, including within the slots of the driven gear. This resulted in the device clogging presence of the cells in the space surrounding the driven gear prevented pin-slot engagement. This resulted in failure of actuation of the device.

The single-gear device remained functional in the tumor-bearing mice throughout the experiment and robust actuation was observed (Figure 6.4). Initial experiments with the single-gear device implanted in non-tumor bearing mice remained functional for up to two weeks (data not shown). Figure 6.4 shows the state of the device throughout the course of treatment. In the left-panel of Figure 6.4, the sketch in the inset shows the orientation for implantation and the different features in the device. On the skin-side of the device, a layer of red fluorescent beds suspended in PEG400 gels was polymerized in one of the chambers. That same chamber also contains the iron oxide superparamagnetic nanoparticles on the tumor-side of the device. In this way, we are able to incorporate fluorescent references to aid imaging while maintaining 5 chambers to be loaded with a dose of doxorubicin each. The right panel of Figure 6.4 shows the various positions of the red fluorescent reference chamber that corresponds to the “dose number” of the device. Thus by magnetically moving the red fluorescent reference, we were

able to accurately actuate the device to release each dose throughout the course of the experiment.

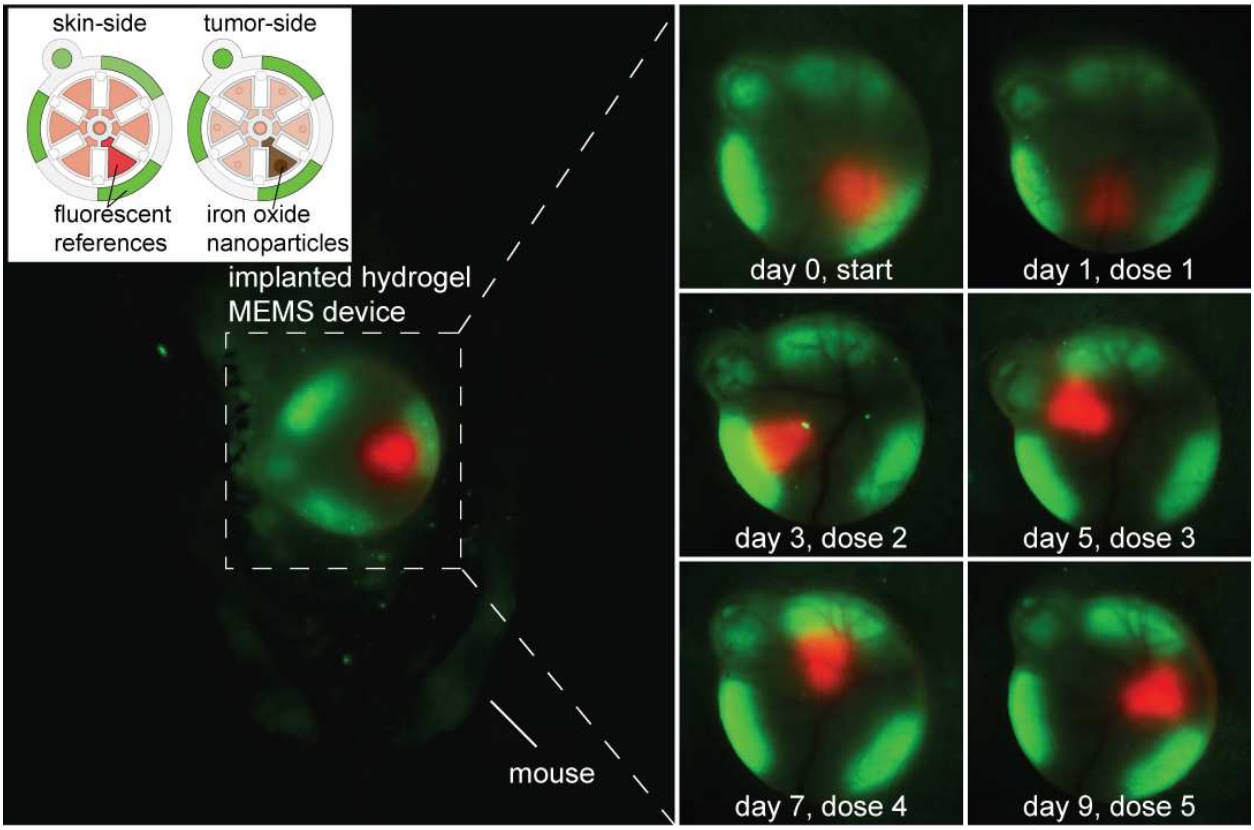

Figure 6.4: *In vivo* imaging of a mouse implanted with hydrogel MEMS device for local low dosing of doxorubicin. Left panel shows the location of the device as implanted into the mouse as well as sketches of the orientation in which the device was implanted (inset). The right panel shows the state of the device as each dose of doxorubicin was released over the course of the experiment.

6.2.2.2 Assessment of treatment via bioluminescent imaging

We tried as much as possible to implant our doxorubicin-loaded devices close to the tumor while ensuring that the bioluminescent signal was not obstructed during imaging. As can be seen in Figure 6.5, the device is located at the very edge of the tumor and does not lie on top of the tumor relative to the direction of imaging. In addition, the bioluminescent intensities measured over time were normalized with that of the starting intensity (I_0) before the start of

treatment. Therefore, we are confident that the presence of the device does not affect the bioluminescent signal that is generated by the luciferase-tagged cells.

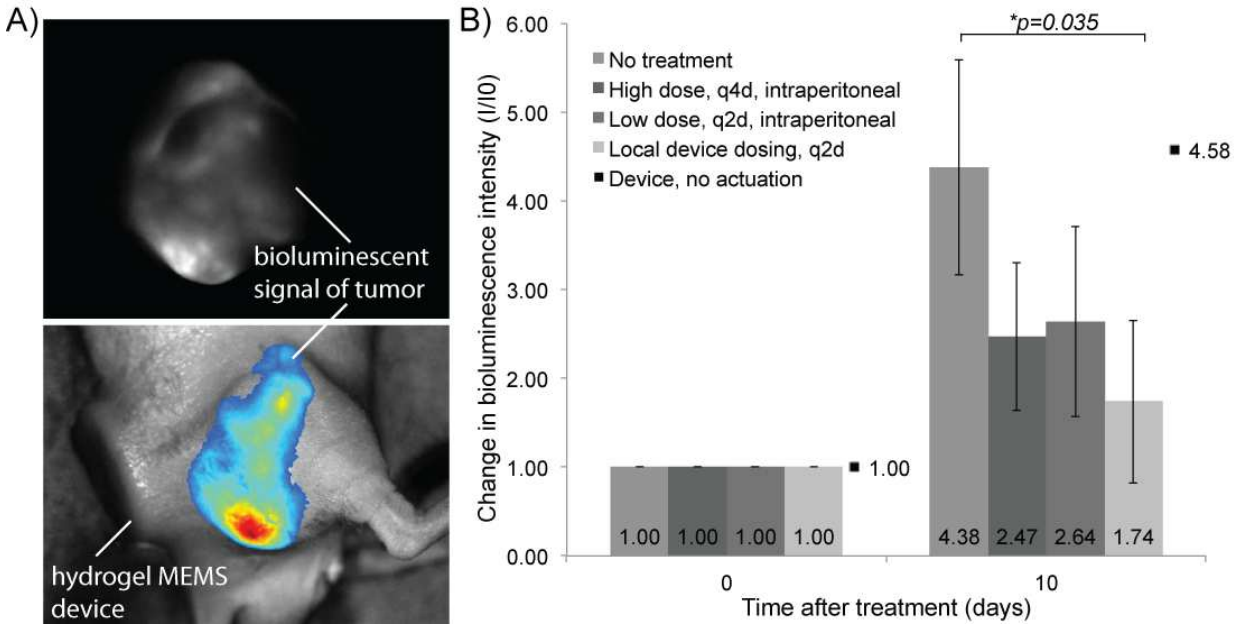

Figure 6.5: Local delivery of doxorubicin via hydrogel MEMS to the site of a tumor. A) The top image shows the raw bioluminescent image taken after an injection of d-luciferin. A color map image superimposed on a bright-field image of the mouse (bottom) shows the location of the implanted device. The position of the device does not interfere with bioluminescent intensity that is measured. B) The bar graph shows the change in mean bioluminescence of the various treatment groups (n=3 for each group). The mice that received local delivery of doxorubicin from the hydrogel MEMS device (local device dosing) showed the smallest increase of bioluminescent signal over the course of 10 days (p=0.035). There was no statistical significance between the other control groups.

As can be seen from Figure 6.5B, all treatment groups have smaller increases in bioluminescence intensity compared to the group that was not given doxorubicin at all. However, the group that received local dosing from the implantable hydrogel MEMS device showed the least increase in bioluminescence intensity of the tumor (I/I_0=1.74± 0.92). The statistical significance of these results was calculated using a two-tailed Student's t-Test. It was found that the only group that was statistically significant compared to the control group ($p<0.05$) was the group that received local dosing with the implantable hydrogel MEMS device

with a p-value of 0.035. Additionally, a control experiment where a doxorubicin-loaded hydrogel MEMS device was implanted into a single mouse but not actuated had an I/I_0 value of 4.58 after 10 days. This shows that the treatment of the tumor was not due to the passive release of doxorubicin out of the device through background leakage but via the active release of doxorubicin via magnetic actuation.

6.2.2.3 Assessment of treatment via histological staining

The device was explanted at the end of the experiments and the tissue surrounding the device (fibrous capsule and skin) were sent for H&E and Trichome staining. As can be seen from Figure 6.6, the device remained intact at the end of the experiment and a very thin fibrious capsule layer had formed around the device. Histological staining showed that there was a very thin layer of fibrous tissue (<100μm) that had formed after 10 days. There was also an absence of inflammatory cells such as giant cells. All this indicates that there was normal wound healing and there was not a severe inflammatory reaction to the PEG gels.

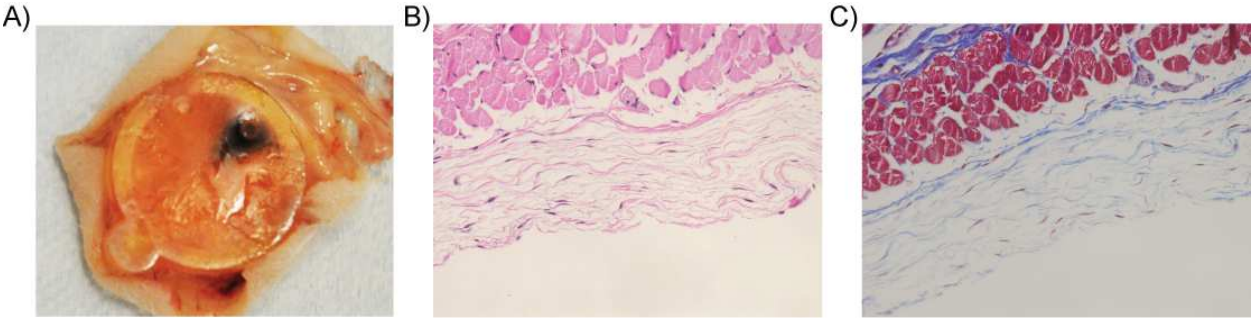

Figure 6.6: Explanted hydrogel MEMS device and histology of the surrounding tissue. A) Image of the device that was explanted from the mouse at the end of the experiment. B) H&E and C) Trichome staining of the skin and fibrous capsule surrounding the implanted device. Histology images were taken at a 20x magnification.

TUNEL staining was performed on the tumors and hearts of all the mice at the end of the experiment. TUNEL staining is a method for detecting DNA fragmentation by labeling the

terminal end of nucleic acids and it is a common method for detecting cell apoptosis[96]. Figure 6.7 shows example images of the histological staining performed on the tumors of mice from different treatment groups. Apoptotic cells will have their nuclei stained brown, while healthy cell nuclei are counterstained blue (hematoxylin). A qualitative assessment of the stained tissue samples was performed. The example images shown in Figure 6.7 are representative of the tissue samples that were stained. The arrows in Figure 6.7 indicate the presence of apoptotic cells but do not label all the apoptotic cells that are present in the image. As can be seen from Figure 6.7, tumors of mice in the non-treatment group (Figure 6.7 A-C) and those that were given frequent (q2d) low doses of doxorubicin intraperitoneally (Figure 6.7 D-F) had little to no apoptotic cells present. Tumors of mice that were administered high doses of doxorubicin (q4d) intraperitoneally showed signs of apoptosis (Figure 6.7 G-I). Tumors of mice that were treated with local device dosing via our implantable device also showed evidence of apoptosis (Figure 6.7 J-L). Signs of apoptosis were more evident for the groups that were treated using our implantable device as well as that for the mice that were given the high systemic dose of doxorubicin, this is in comparison to much lower levels of apoptosis that were present for the other two groups. Additionally, we saw evidence of necrosis for mice that were given doxorubicin via local device dosing as well as the high systemic dose. This is characterized by the large regions where ghost cells are present; distinguishable cell outlines but with an absence of healthy nuclei. This level of necrosis was not apparent for the other two treatment groups. As levels or apoptosis and necrosis in tumors are key indicators in assessing treatment of tumors[97-99] the evidence of these in the tumor tissues indicate that there was a positive treatment effect. This effect is also in stark contrast with no treatment, or low systemic dosing groups where little to no apoptosis and necrosis was detected. Further quantitative analysis will have to be performed to evaluate the percent apoptosis and necrosis between the groups but this initial result is very encouraging and supports the data obtained via bioluminescent imaging which also shows better response to treatment for groups that are treated with local device

dosing compared to control groups. Thus we can conclude that local delivery of doxorubicin via implantable hydrogel MEMS devices does show some level of efficacious treatment.

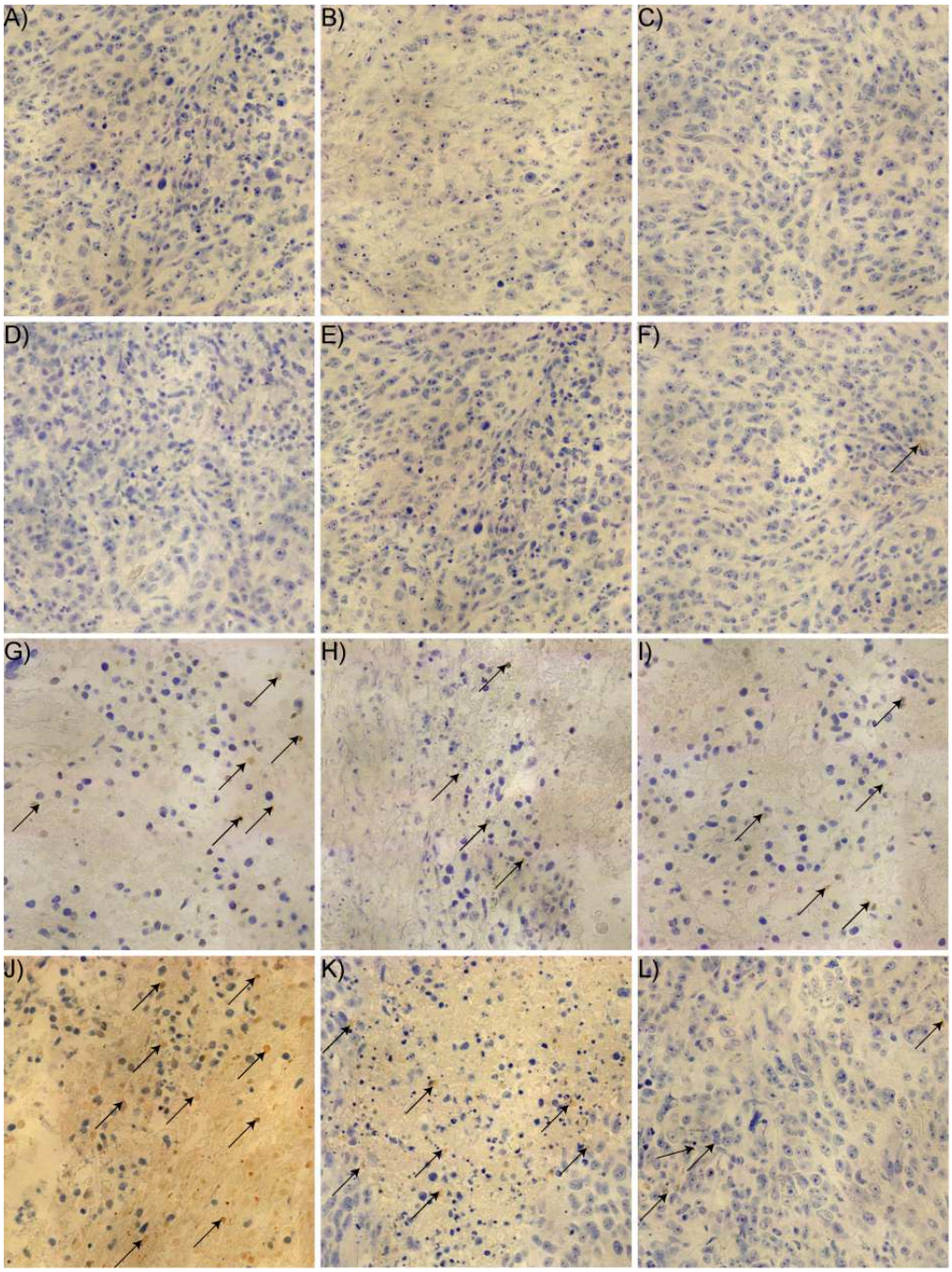

Figure 6.7: TUNEL staining of bone tumor from the various treatment groups. Example images of the histological staining are presented: (A-C) Non-treatment group, (D-F) Low dose, q2d, (G-I) high dose, q4d, (J-L) local device dosing. Arrows indicate the presence of some of the apoptotic cells. Images were taken at 40x magnification.

We also assessed the degree of apoptosis in the heart tissue has doxorubicin is known to cause cardiotoxicity and cardiomyopathy[100, 101]. Figure 6.8 shows TUNEL staining of heart tissue from mice of the various treatment groups.

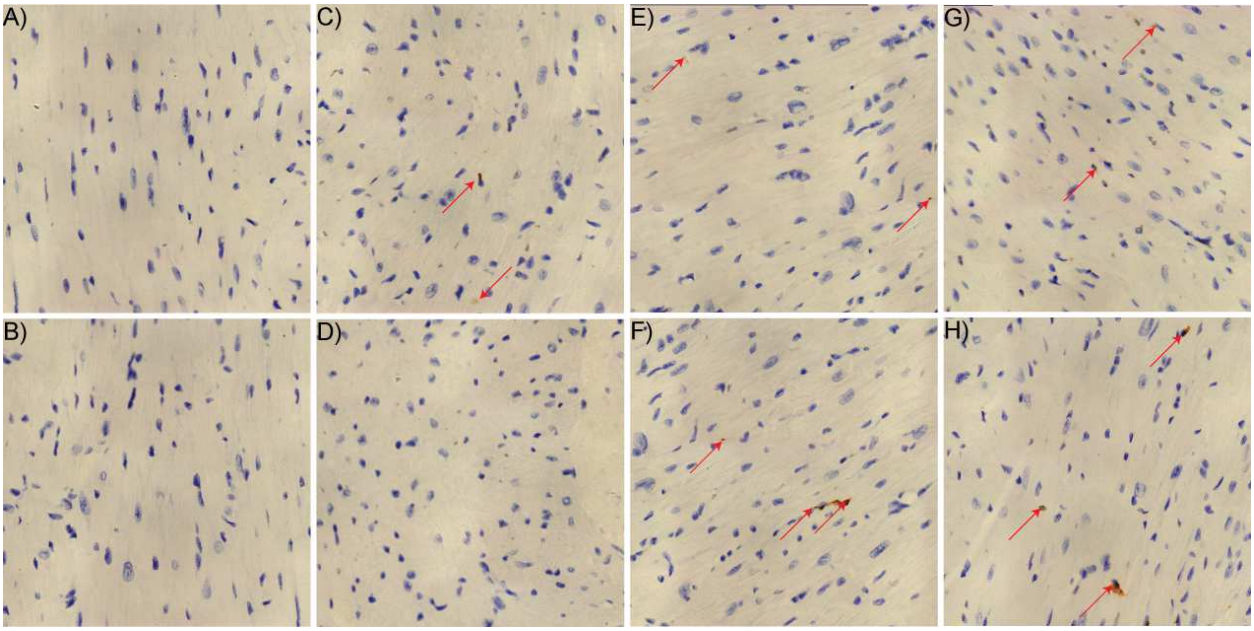

Figure 6.8: TUNEL staining of cardiomyocytes of mice from various treatment groups. (A-B) Local device dosing group, (C-D) low dose, q2d group, (E-F) high dose, q4d group and (G-H) mice that were give only 2 doses of 50µg of doxuribicin. Red arrows indicate evidence of apoptosis. Images were taken at 40x magnification.

As can be seen from Figure 6.8, there was little to no evidence of apoptosis for the mice that were treated with the hydrogel MEMS device. For the mice that were given low doses of doxorubicin systemically, some apoptosis detected. As expected, there was also evidence of cardiotoxicity for mice that were give a total of 5 high standard doses of doxorubicin (250µg cumulative dose of doxorubicin). Even when mice were only given 2 standard systemic doses of doxorubicin (Figure 6.8 G-H), cell apoptosis was detected in the cardiac tissue. Therefore, it can be concluded that we were able to avoid the side effects of cardiotoxicity using our method of drug delivery. Once again, this is just a qualitative assessment and a quantitative assessment is required so that we can compare the percentage apoptosis in the cardiac tissue of different

treatment groups. This analysis as well as the analysis of the TUNEL staining of tumor tissues will be conducted in preparation for the submission of this body of work for publication in a scientific journal.

6.3 Conclusion

In culmination of the work done in Chapters 3-5, we have demonstrated a very convincing use of an implantable hydrogel MEMS device for the local delivery of therapeutics. Based on both the live monitoring of tumor growth and end-point histological analysis, our proposed drug delivery device has shown to be more efficacious than standard administration of chemotherapy; achieving treatment of tumors at just a fraction of the standard dose. We not only improved upon a therapy that has arguably not been very effective at treating osteosarcoma[102-104] without having to change the composition of the drug or having to add adjuvant therapies[105], we were also able to demonstrate that locally delivering low doses of chemotherapy results in reduced side-effects that have been associated with standard treatments.

The work described in Chapters 3-6 are currently being written up as a manuscript in preparation to be submitted to a peer-reviewed journal.

Chapter 7
Summary

This dissertation has demonstrated the use of microfabrication and microfluidic techniques in developing novel medical devices for use in diagnosis and treatment. First, we successfully demonstrated the implementation of a microfluidic device in the capture and enumeration of CD4+ T-cells. The microfluidic device consisted of microstructures which increased the surface area so as to increase capture of the cells, as well as provided the optimal shear stresses for rinsing away CD4- cells whilst retaining cells of interest. These cells were then specifically detected in the same chamber via the introduction of a chemiluminescent substrate. Prior labeling of the cells with anti-human CD3 antibodies and HRP conjugated IgG ensures that only T-cells that are both CD3+ and CD4+ contributed to the chemiluminescent signal detected. Our method showed high sensitivities and specificities that can be further improved by increasing the amount of HRP conjugated IgG used to label the cells. Increasing the amount of HRP conjugated IgG also had the effect of increasing the dynamic range and linearity of the plot of chemiluminescent signal vs. count for samples with low CD4 counts. This is particularly relevant in the case of monitoring patients with HIV/AIDS as we would be interested in looking at CD4 counts in the lower range. This technology is amenable for miniaturization as the detection method only requires the use of a photodetector and no other equipment, such as complex light sources for fluorescence imaging or image/data analysis tools are required. This work as been published[36].

Future work for the further development of this technique would include the miniaturization of the detection set-up (silicon photodetector and picoammeter) and performing on-chip labeling of the CD4+ T-cells. In the current format, where prior-labeling of the CD3+ cells is required, the off-chip incubation step prevents this test from being implemented in point-of-care settings

where it can be used by untrained personnel (eg: clinic workers or patients). Doing away with this one preprocessing step before the start of the assay would greatly increase the likelihood for such a test to be used at the point-of-care. Suggested ways for addressing this would be to include multiple chambers in the microfluidic platform. As chemiluminescent techniques are very sensitive to background noises, incubations with a HRP-labeled antibodies should be performed in a separate chamber that is upstream from the capture and detection chamber in order to increase the signal-to-noise ratio which might be affected by residual HRP-conjugated antibodies. This would also involve a more sophisticated design which allows for fluid handling, such as with microfluidic valves.

The second main topic, which is covered by the rest of the chapters of this dissertation, was the development of a novel microfabrication strategy for constructing MEMS-like devices entirely out of hydrogels – Hydrogel MEMS. The material of choice for the fabrication of these devices was PEGDA-based hydrogels. These polymers were attractive candidates due to their biocompatibility, easily tunable material properties and ease of polymerization as they can be UV-crosslinked and structures can be easily defined by using photomasks. PEG-based hydrogels have also be FDA-approved in humans. In the initial stages of this project, we first characterized several PEGDA compositions with a wide range of mechanical stiffness and permeability. This provided us with a wide variety of candidates when selecting compositions for constructing MEMS devices out of PEGDA.

We then designed and constructed various types of devices out of PEGDA hydrogels. The various devices were designed with drug delivery applications in mind and have common features in order to achieve payload delivery. These features include a moving component that is doped with superparamagnetic iron oxide nanoparticles that responds to magnetic actuation, reservoirs in which drugs or payloads can be contained, a diffusion window or aperture out of which payloads can exit from the device and into the surrounding environment, and structures

which serve as locking mechanisms to prevent accidental movement and hence release of payloads. This design and fabrication stage was an iterative process in which we fine-tuned the fabrication strategy in trying to construct hydrogel MEMS devices that can be robustly actuated. With each design, we learned certain strategies that were important towards developing the final implantable device. This included methods for incorporating iron-oxide nanoparticles into microcomponents of PEGDA hydrogels, introduction of payload into the fabricated device versus in situ polymerization of payload in PEGDA hydrogels, the type of translational movement during the operation of the device which plays a part in minimizing the foot print of the device and other strategies that including leveraging the different stiffnesses in hydrogels to aid in maintaining the alignment of moving components.

We then tested the capabilities of these devices in delivering payloads in *in vitro* and *in vivo* environments as well as assessed the mechanical robustness of such devices after subcutaneous implantation into an animal model. We were able to demonstrate that we were able to control and change the release profiles of payloads from the devices via magnetic actuation, while achieving a high percentage of release of payload from the devices with each actuation. Additionally, we were able to introduce more than one type of payload into each hydrogel MEMS device and specifically select which payload would be delivered. This added function was also demonstrated in an in vivo mouse model. Using *in vivo* imaging techniques we were also able to show that the mechanical robustness of these devices were maintained throughout the experiment.

These results culminated in the implementation of hydrogel MEMS as drug delivery devices for disease treatment. Specifically, we explored the application of hydrogel MEMS devices for localized, low dose chemotherapy treatment in an osteosarcoma model. These devices were designed to deliver low doses (~10% of a standard dose of chemotherapy) at high frequencies locally at site of a tumor. The progression of tumor growth was then assessed via *in vivo*

imaging techniques. In this demonstration, we were able to show an increased efficacy of treatment as well as a reduction in the side effects of the drug compared to standard administrations of doxorubicin. Specifically, signs of cardiotoxicity were less evident in mice treated with doxorubicin delivered via hydrogel MEMS devices. In future, further quantitative analysis of histological results will be performed in order to assess the efficacy of treatment, especially between the group that was administered with local low dosing of doxorubicin via the implantable hydrogel MEMS device and the group that was administered high systemic doses of doxorubicin. The results of this analysis will then be presented in a future publication of the work presented in this thesis.

Therefore, we have devised strategies for fabricating a next-generation of implantable devices. These devices not only have the potential to rival the capabilities of other active-control MEMS based drug delivery systems but also has the added advantage of being entirely biocompatible, doing away with the need of removal after it has served its function. Although the specific hydrogels used in this demonstration was only biocompatible but not biodegradable, we believe this strategy can be used for the construction of similar devices using any photopolymerizable hydrogel, such as methacrylated hyaluronic acid[106] and poly(lactic acid)-PEG-Poly(lactic acid) copolymer [107]. This would be an interesting investigation for future development of implantable hydrogel MEMS devices. Other future developments would also include strategies to incorporate different payloads (such as cells in stem cell therapies) and payloads of different forms (solid vs. liquid) for improved drug stability during long term storage within the device after implantation as well as to decrease the background leakages of drug from the device. To this end, future work could also be done to introduce methods to disrupt gels during the release of payload in order to reduce background leakages due to open apertures in the device. This could be achieved either by the introduction enzyme-cleavable or pH sensitive hydrogels and reservoirs containing the corresponding enzyme/pH environment that can be aligned to allow for

a change in state of the hydrogel, resulting in the release of payload. Alternatively, temperature-sensitive gels can be used as barriers between the payload and surrounding environment. These gels can be actuated using a combination of magnetic actuation and localized thermal actuation (such as with focused ultrasounds) to trigger the release of payloads.

Bibliography

1. Manz, A., N. Graber, and H.M. Widmer, *Miniaturized total chemical analysis systems: A novel concept for chemical sensing.* Sensors and Actuators B: Chemical, 1990. **1**(1–6): p. 244-248.

2. Freaney, R., et al., *Novel instrumentation for real-time monitoring using miniaturized flow systems with integrated biosensors.* Ann Clin Biochem, 1997. **34 (Pt 3)**: p. 291-302.

3. Kopp, M.U., A.J. Mello, and A. Manz, *Chemical amplification: continuous-flow PCR on a chip.* Science, 1998. **280**(5366): p. 1046-8.

4. Whitesides, G.M., *The origins and the future of microfluidics.* Nature, 2006. **442**(7101): p. 368-73.

5. Elman, N.M., et al., *Electro-thermally induced structural failure actuator (ETISFA) for implantable controlled drug delivery devices based on micro-electro-mechanical-systems.* Lab Chip, 2010. **10**(20): p. 2796-804.

6. Kim, D.H., et al., *Epidermal electronics.* Science, 2011. **333**(6044): p. 838-43.

7. Mabey, D., et al., *Diagnostics for the developing world.* Nat Rev Microbiol, 2004. **2**(3): p. 231-40.

8. Chin, C.D., V. Linder, and S.K. Sia, *Lab-on-a-chip devices for global health: past studies and future opportunities.* Lab Chip, 2007. **7**(1): p. 41-57.

9. Chin, C.D., et al., *Microfluidics-based diagnostics of infectious diseases in the developing world.* Nat Med, 2011. **17**(8): p. 1015-9.

10. Cheng, X., et al., *Enhancing the performance of a point-of-care CD4+ T-cell counting microchip through monocyte depletion for HIV/AIDS diagnostics.* Lab Chip, 2009. **9**(10): p. 1357-64.

11. Cheng, X., et al., *A microchip approach for practical label-free CD4+ T-cell counting of HIV-infected subjects in resource-poor settings.* J Acquir Immune Defic Syndr, 2007. **45**(3): p. 257-61.

12. Jokerst, J.V., et al., *Integration of semiconductor quantum dots into nano-bio-chip systems for enumeration of CD4+ T cell counts at the point-of-need.* Lab Chip, 2008. **8**(12): p. 2079-90.

13. Rodriguez, W.R., et al., *A microchip CD4 counting method for HIV monitoring in resource-poor settings.* PLoS Med, 2005. **2**(7): p. e182.

14. Martinez, A.W. and E.L. Chaikof, *Microfabrication and nanotechnology in stent design.* Wiley Interdiscip Rev Nanomed Nanobiotechnol, 2011. **3**(3): p. 256-68.

15. Hoekstra, A., *Pain relief mediated by implantable drug delivery devices.* Int J Artif Organs, 1994. **17**(3): p. 151-4.

16. Xu, S., et al., *Soft microfluidic assemblies of sensors, circuits, and radios for the skin.* Science, 2014. **344**(6179): p. 70-4.

17. Bridges, A.W. and A.J. Garcia, *Anti-inflammatory polymeric coatings for implantable biomaterials and devices.* J Diabetes Sci Technol, 2008. **2**(6): p. 984-94.

18. Rizzi, G., et al., *Biomedical coatings to improve the tissue-biomaterial interface.* Int J Artif Organs, 2004. **27**(8): p. 649-57.

19. Koyama, N., et al., *Acrylamide genotoxicity in young versus adult gpt delta male rats.* Mutagenesis, 2011. **26**(4): p. 545-9.

20. Chang, H.J., et al., *Discordant human epidermal growth factor receptor 2 and hormone receptor status in primary and metastatic breast cancer and response to trastuzumab.* Jpn J Clin Oncol, 2011. **41**(5): p. 593-9.

21. Ford, N., et al., *The future role of CD4 cell count for monitoring antiretroviral therapy.* Lancet Infect Dis, 2015. **15**(2): p. 241-7.

22. Aledort, J.E., et al., *Reducing the burden of HIV/AIDS in infants: the contribution of improved diagnostics.* Nature, 2006. **444 Suppl 1**: p. 19-28.

23. Aledort, J.E., et al., *Reducing the burden of sexually transmitted infections in resource-limited settings: the role of improved diagnostics.* Nature, 2006. **444 Suppl 1**: p. 59-72.

24. Yager, P., et al., *Microfluidic diagnostic technologies for global public health.* Nature, 2006. **442**(7101): p. 412-8.

25. *Adult HIV prevalence (15-49 years), 2011*, World Health Organization.

26. *Health Financing: Per capita total expenditure on health at average exchange rate (US$): 2011*. Available from: http://gamapserver.who.int/gho/interactive_charts/health_financing/atlas.html.

27. *Revised Surveillance Case Definitions for HIV Infection Among Adults, Adolescents, and Children Aged <18 Months and for HIV Infection and AIDS Among Children Aged 18 Months to <13 Years—United States, 2008*, Center for Disease Control and Prevention.

28. *Patient Monitoring Guidelines For HIV Care and ART;*, 2006, World Health Organization.

29. *Consolidated guidelines on the use of antiretroviral drugs for treating and preventing HIV inection*, 2013, World Health Organization. p. 272.

30. Jarvis, J.N., et al., *Screening for cryptococcal antigenemia in patients accessing an antiretroviral treatment program in South Africa.* Clin Infect Dis, 2009. **48**(7): p. 856-62.

31. *"3 By 5" Progress Report*, 2004, World Health Orgnanization.

32. *Antiretroviral Therapy for HIV Infection in Adults and Adolescents: Recommendations for a Public Health Approach*, 2006, World Health Organization.

33. Miguel, S.M., et al., *ERK1/2-activated de novo Mapkapk2 synthesis is essential for osteogenic growth peptide mitogenic signaling in osteoblastic cells.* J Biol Chem, 2005. **280**(45): p. 37495-502.

34. Xia, Y.N. and G.M. Whitesides, *Soft lithography.* Annual Review of Materials Science, 1998. **28**: p. 153-184.

35. Moon, S., et al., *Integrating microfluidics and lensless imaging for point-of-care testing.* Biosens Bioelectron, 2009. **24**(11): p. 3208-14.

36. Wang, Z., et al., *Microfluidic CD4+ T-cell counting device using chemiluminescence-based detection.* Anal Chem, 2010. **82**(1): p. 36-40.

37. Zhu, J. and R.E. Marchant, *Design properties of hydrogel tissue-engineering scaffolds.* Expert Rev Med Devices, 2011. **8**(5): p. 607-26.

38. Beamish, J.A., et al., *The effects of monoacrylated poly(ethylene glycol) on the properties of poly(ethylene glycol) diacrylate hydrogels used for tissue engineering.* J Biomed Mater Res A, 2010. **92**(2): p. 441-50.

39. El-Sherbiny, I.M. and M.H. Yacoub, *Hydrogel scaffolds for tissue engineering: Progress and challenges.* Glob Cardiol Sci Pract, 2013. **2013**(3): p. 316-42.

40. Cruise, G.M., et al., *In vitro and in vivo performance of porcine islets encapsulated in interfacially photopolymerized poly(ethylene glycol) diacrylate membranes.* Cell Transplant, 1999. **8**(3): p. 293-306.

41. Khetan, S. and J. Burdick, *Cellular encapsulation in 3D hydrogels for tissue engineering.* J Vis Exp, 2009(32).

42. Khademhosseini, A., et al., *Micromolding of photocrosslinkable hyaluronic acid for cell encapsulation and entrapment.* J Biomed Mater Res A, 2006. **79**(3): p. 522-32.

43. Arti Vashist, A.V., Y.K. Gupta, Sharif Ahmad, *Recent advances in hydrogel based drug delivery systems for the human body.* Journal of Materials Chemistry B. **2**.

44. Tsurkan, M.V., et al., *Growth factor delivery from hydrogel particle aggregates to promote tubular regeneration after acute kidney injury.* J Control Release, 2013. **167**(3): p. 248-55.

45. Weng, L., et al., *An in situ forming biodegradable hydrogel-based embolic agent for interventional therapies.* Acta Biomater, 2013. **9**(9): p. 8182-91.

46. Qiu, Y. and K. Park, *Environment-sensitive hydrogels for drug delivery.* Adv Drug Deliv Rev, 2001. **53**(3): p. 321-39.

47. Gupta, P., K. Vermani, and S. Garg, *Hydrogels: from controlled release to pH-responsive drug delivery.* Drug Discov Today, 2002. **7**(10): p. 569-79.

48. Ruan, G. and S.S. Feng, *Preparation and characterization of poly(lactic acid)-poly(ethylene glycol)-poly(lactic acid) (PLA-PEG-PLA) microspheres for controlled release of paclitaxel.* Biomaterials, 2003. **24**(27): p. 5037-44.

49. Alconcel, S.N.S., A.S. Baas, and H.D. Maynard, *FDA-approved poly(ethylene glycol)-protein conjugate drugs.* Polymer Chemistry, 2011. **2**(7): p. 1442-1448.

50. West, J.L. and J.A. Hubbell, *Photopolymerized Hydrogel Materials for Drug-Delivery Applications.* Reactive Polymers, 1995. **25**(2-3): p. 139-147.

51. Hillwest, J.L., et al., *Inhibition of Thrombosis and Intimal Thickening by in-Situ Photopolymerization of Thin Hydrogel Barriers.* Proceedings of the National Academy of Sciences of the United States of America, 1994. **91**(13): p. 5967-5971.

52. Mazzoccoli, J.P., et al., *Mechanical and cell viability properties of crosslinked low- and high-molecular weight poly(ethylene glycol) diacrylate blends.* Journal of Biomedical Materials Research Part A, 2010. **93A**(2): p. 558-566.

53. Cruise, G.M., D.S. Scharp, and J.A. Hubbell, *Characterization of permeability and network structure of interfacially photopolymerized poly(ethylene glycol) diacrylate hydrogels.* Biomaterials, 1998. **19**(14): p. 1287-1294.

54. Ross, A.E., M.Y. Tang, and R.A. Gemeinhart, *Effects of Molecular Weight and Loading on Matrix Metalloproteinase-2 Mediated Release from Poly(Ethylene Glycol) Diacrylate Hydrogels.* Aaps Journal, 2012. **14**(3): p. 482-490.

55. Ali, S., et al., *Immobilization of Cell-Adhesive Laminin Peptides in Degradable PEGDA Hydrogels Influences Endothelial Cell Tubulogenesis.* Biores Open Access, 2013. **2**(4): p. 241-9.

56. He, L., et al., *Electroactive SWNT/PEGDA hybrid hydrogel coating for bio-electrode interface.* Colloids and Surfaces B-Biointerfaces, 2011. **87**(2): p. 273-279.

57. Rao, L., et al., *Polyethylene glycol-containing polyurethane hydrogel coatings for improving the biocompatibility of neural electrodes.* Acta Biomaterialia, 2012. **8**(6): p. 2233-2242.

58. Ding, X., et al., *Antibacterial and antifouling catheter coatings using surface grafted PEG-b-cationic polycarbonate diblock copolymers.* Biomaterials, 2012. **33**(28): p. 6593-6603.

59. Bostman, O. and H. Pihlajamaki, *Clinical biocompatibility of biodegradable orthopaedic implants for internal fixation: a review.* Biomaterials, 2000. **21**(24): p. 2615-21.

60. Hofmann, G.O., *Biodegradable implants in traumatology: a review on the state-of-the-art.* Arch Orthop Trauma Surg, 1995. **114**(3): p. 123-32.

61. Ziegler, J., et al., *Adsorption and release properties of growth factors from biodegradable implants.* J Biomed Mater Res, 2002. **59**(3): p. 422-8.

62. Mazzoccoli, J.P., et al., *Mechanical and cell viability properties of crosslinked low- and high-molecular weight poly(ethylene glycol) diacrylate blends.* J Biomed Mater Res A, 2010. **93**(2): p. 558-66.

63. Seiffert, S. and W. Oppermann, *Systematic evaluation of FRAP experiments performed in a confocal laser scanning microscope.* J Microsc, 2005. **220**(Pt 1): p. 20-30.

64. Gillette, B.M., et al., *Dynamic hydrogels: switching of 3D microenvironments using two-component naturally derived extracellular matrices.* Adv Mater, 2010. **22**(6): p. 686-91.

65. Huang, X. and T.L. Lowe, *Biodegradable thermoresponsive hydrogels for aqueous encapsulation and controlled release of hydrophilic model drugs.* Biomacromolecules, 2005. **6**(4): p. 2131-9.

66. Ta, H.T., et al., *A chitosan hydrogel delivery system for osteosarcoma gene therapy with pigment epithelium-derived factor combined with chemotherapy.* Biomaterials, 2009. **30**(27): p. 4815-23.

67. Ta, H.T., et al., *A chitosan-dipotassium orthophosphate hydrogel for the delivery of Doxorubicin in the treatment of osteosarcoma.* Biomaterials, 2009. **30**(21): p. 3605-13.

68. Ritger, P.L. and N.A. Peppas, *A simple equation for description of solute release I. Fickian and non-fickian release from non-swellable devices in the form of slabs, spheres, cylinders or discs.* Journal of Controlled Release, 1987. **5**(1): p. 23-36.

69. Serra, L., J. Domenech, and N.A. Peppas, *Drug transport mechanisms and release kinetics from molecularly designed poly(acrylic acid-g-ethylene glycol) hydrogels.* Biomaterials, 2006. **27**(31): p. 5440-51.

70. Grogan, S.P., et al., *Digital micromirror device projection printing system for meniscus tissue engineering.* Acta Biomater, 2013. **9**(7): p. 7218-26.

71. Cui, X. and T. Boland, *Human microvasculature fabrication using thermal inkjet printing technology.* Biomaterials, 2009. **30**(31): p. 6221-7.

72. Poon, Y.F., et al., *Hydrogels based on dual curable chitosan-graft-polyethylene glycol-graft-methacrylate: application to layer-by-layer cell encapsulation.* ACS Appl Mater Interfaces, 2010. **2**(7): p. 2012-25.

73. Kim, J., et al., *Programming magnetic anisotropy in polymeric microactuators.* Nat Mater, 2011. **10**(10): p. 747-52.

74. Tumbleston, J.R., et al., *Additive manufacturing. Continuous liquid interface production of 3D objects.* Science, 2015. **347**(6228): p. 1349-52.

75. Hockaday, L.A., et al., *Rapid 3D printing of anatomically accurate and mechanically heterogeneous aortic valve hydrogel scaffolds.* Biofabrication, 2012. **4**(3): p. 035005.

76. Hanson Shepherd, J.N., et al., *3D Microperiodic Hydrogel Scaffolds for Robust Neuronal Cultures.* Adv Funct Mater, 2011. **21**(1): p. 47-54.

77. Cheung, Y.K., et al., *Microscale control of stiffness in a cell-adhesive substrate using microfluidics-based lithography.* Angew Chem Int Ed Engl, 2009. **48**(39): p. 7188-92.

78. Giray, S., et al., *Controlled drug delivery through a novel PEG hydrogel encapsulated silica aerogel system.* J Biomed Mater Res A, 2012. **100**(5): p. 1307-15.

79. Zustiak, S.P. and J.B. Leach, *Characterization of protein release from hydrolytically degradable poly(ethylene glycol) hydrogels.* Biotechnol Bioeng, 2011. **108**(1): p. 197-206.

80. Zhao, X., et al., *Active scaffolds for on-demand drug and cell delivery.* Proc Natl Acad Sci U S A, 2011. **108**(1): p. 67-72.

81. Wikipedia. *"Geneva drive"* [cited 2015; Available from: http://commons.wikimedia.org/wiki/File:Geneva_drive.svg -/media/File:Geneva_drive.svg

82. Clement, K.M. and D.J. Mansour, *Improving uptake of the copper intrauterine device for emergency contraception by educating pharmacists in the community.* J Fam Plann Reprod Health Care, 2014. **40**(1): p. 41-5.

83. Ziegler, R., et al., *ProAct study: new features of insulin pumps improve diabetes management and glycemic control in patients after transition of continuous*

subcutaneous insulin infusion systems. Diabetes Technol Ther, 2013. **15**(9): p. 738-43.

84. Chase, H.P., et al., *The use of insulin pumps with meal bolus alarms in children with type 1 diabetes to improve glycemic control.* Diabetes Care, 2006. **29**(5): p. 1012-5.

85. Farra, R., et al., *First-in-human testing of a wirelessly controlled drug delivery microchip.* Sci Transl Med, 2012. **4**(122): p. 122ra21.

86. Elman, N.M., H.L. Ho Duc, and M.J. Cima, *An implantable MEMS drug delivery device for rapid delivery in ambulatory emergency care.* Biomed Microdevices, 2009. **11**(3): p. 625-31.

87. Gensler, H., et al., *An implantable MEMS micropump system for drug delivery in small animals.* Biomed Microdevices, 2012. **14**(3): p. 483-96.

88. Yang, Y., et al., *The efficacy of abraxane on osteosarcoma xenografts in nude mice and expression of secreted protein, acidic and rich in cysteine.* Am J Med Sci, 2012. **344**(3): p. 199-205.

89. Berken, A., et al., *High-frequency low-dose multiple-drug chemotherapy in advanced metastatic breast cancer.* Cancer, 1982. **49**(11): p. 2231-3.

90. Prescott, J.H., et al., *Chronic, programmed polypeptide delivery from an implanted, multireservoir microchip device.* Nat Biotechnol, 2006. **24**(4): p. 437-8.

91. Razzacki, S.Z., et al., *Integrated microsystems for controlled drug delivery.* Adv Drug Deliv Rev, 2004. **56**(2): p. 185-98.

92. Makadia, H.K. and S.J. Siegel, *Poly Lactic-co-Glycolic Acid (PLGA) as Biodegradable Controlled Drug Delivery Carrier.* Polymers (Basel), 2011. **3**(3): p. 1377-1397.

93. Grayson, A.C., et al., *Differential degradation rates in vivo and in vitro of biocompatible poly(lactic acid) and poly(glycolic acid) homo- and co-polymers for a polymeric drug-delivery microchip.* J Biomater Sci Polym Ed, 2004. **15**(10): p. 1281-304.

94. Grimer, R.J., et al., *Surgical outcomes in osteosarcoma.* J Bone Joint Surg Br, 2002. **84**(3): p. 395-400.

95. Luu, H.H., et al., *An orthotopic model of human osteosarcoma growth and spontaneous pulmonary metastasis.* Clin Exp Metastasis, 2005. **22**(4): p. 319-29.

96. Kyrylkova, K., et al., *Detection of apoptosis by TUNEL assay.* Methods Mol Biol, 2012. **887**: p. 41-7.

97. Hauben, E.I., et al., *Does the histological subtype of high-grade central osteosarcoma influence the response to treatment with chemotherapy and does it affect overall survival? A study on 570 patients of two consecutive trials of the European Osteosarcoma Intergroup.* Eur J Cancer, 2002. **38**(9): p. 1218-25.

98. Rosen, G., et al., *Preoperative chemotherapy for osteogenic sarcoma: selection of postoperative adjuvant chemotherapy based on the response of the primary tumor to preoperative chemotherapy.* Cancer, 1982. **49**(6): p. 1221-30.

99. Li, H.Y., et al., *Celastrol induces apoptosis and autophagy via the ROS/JNK signaling pathway in human osteosarcoma cells: an in vitro and in vivo study.* Cell Death Dis, 2015. **6**: p. e1604.

100. Chatterjee, K., et al., *Doxorubicin cardiomyopathy.* Cardiology, 2010. **115**(2): p. 155-62.

101. Mettler, F.P., D.M. Young, and J.M. Ward, *Adriamycin-induced cardiotoxicity (cardiomyopathy and congestive heart failure) in rats.* Cancer Res, 1977. **37**(8 Pt 1): p. 2705-13.

102. Patel, S.J., et al., *Dose-intense ifosfamide/doxorubicin/cisplatin based chemotherapy for osteosarcoma in adults.* Am J Clin Oncol, 2002. **25**(5): p. 489-95.

103. Dieudonne, F.X., et al., *Targeted inhibition of T-cell factor activity promotes syndecan-2 expression and sensitization to doxorubicin in osteosarcoma cells and bone tumors in mice.* J Bone Miner Res, 2012. **27**(10): p. 2118-29.

104. Zhu, X.Z., H.M. Yin, and J. Mei, *Inhibition of tumors cell growth in osteosarcoma-bearing SD rats through a combination of conventional and metronomic scheduling of neoadjuvant chemotherapy.* Acta Pharmacol Sin, 2010. **31**(8): p. 970-6.

105. Noh, K., et al., *Targeting inflammatory kinase as an adjuvant treatment for osteosarcomas.* J Bone Joint Surg Am, 2011. **93**(8): p. 723-32.

106. Burdick, J.A., et al., *Controlled degradation and mechanical behavior of photopolymerized hyaluronic acid networks.* Biomacromolecules, 2005. **6**(1): p. 386-91.

107. Mason, M., et al., *Predicting controlled-release behavior of degradable PLA-b-PEG-b-PLA hydrogels.* Macromolecules, 2001. **34**(13): p. 4630-4635.